Parton Shower Corrections to Vector-Boson Fusion Processes at the Large Hadron Collider in Next-to-Leading Order QCD Precision

Zur Erlangung des akademischen Grades eines

DOKTORS DER NATURWISSENSCHAFTEN

von der Fakultät für Physik des

Karlsruher Instituts für Technologie (KIT)

genehmigte

DISSERTATION

von

Dipl.-Phys. Franziska Schissler
aus Heilbronn-Neckargartach

Tag der mündlichen Prüfung: 2. Mai 2014

Referent: Prof. Dr. Dieter Zeppenfeld
Korreferent: Prof. Dr. Günter Quast

Abstract

Scrutinizing the properties of the newly discovered boson at the Large Hadron Collider is a challenging endeavor. A rather clean environment for such measurements is provided by vector-boson fusion (VBF) processes. To give reliable predictions for distributions, we have matched several VBF processes to parton showers at next-to-leading order (NLO) accuracy.

The processes under consideration are electroweak gauge-boson production, Higgs boson production with anomalous couplings and Standard Model (SM) Higgs boson production in association with three jets, all via VBF. We match the NLO calculation available within the parton-level Monte Carlo generator VBFNLO to the parton shower in PYTHIA 6, to the standard angular-ordered HERWIG++ parton shower and to the transverse-momentum-ordered dipole shower implemented in HERWIG++. We employ the POWHEG matching scheme by using the program package POWHEG-BOX. Sizable parton shower corrections to the sub-leading jets are found.

In addition, we discuss the program REPOLO, which has been developed in order to reweight SM VBF Higgs events to account for two different scenarios of physics beyond the SM and to calculate signal-background interference effects needed in heavy Higgs boson searches.

Zusammenfassung

Nach der Entdeckung eines higgsartigen Teilchens am Large Hadron Collider ist es wichtig, die Eigenschaften dieses Teilchens genau zu bestimmen. Einen wichtigen Produktionskanal für solche Messungen bildet hierbei die Vektorboson-Fusion (VBF), da sich durch die charakteristische Detektorsignatur viele Untergründe effektiv unterdrücken lassen.

Um möglichst verlässliche Vorhersagen für Verteilungen zu ermöglichen wurden in dieser Arbeit mehrere VBF-Prozesse auf nächst-führender Ordnung mit drei verschiedenen Partonschauern kombiniert, nämlich die VBF-Produktion elektroschwacher Eichbosonen, eines Higgsbosons mit anomalen Kopplungen und eines Standardmodell-Higgsbosons (SM) in Verbindung mit drei Jets. Dazu wurden die Vorhersagen, die mit NLO-Genauigkeit auf Partonniveau in dem Monte-Carlo-Programmpaket VBFNLO verfügbar sind, mit dem Partonschauer in PYTHIA 6, mit dem winkelgeordneten HERWIG++-Partonschauer und dem transversalimpuls-geordneten Dipolschauer, der auch in HERWIG++ implementiert ist, verbunden. Hierfür wurde das POWHEG-Matchingschema verwendet, das in dem Programmpaket POWHEG-BOX verfügbar ist. Bei der Untersuchung der Prozesse wurden beträchtliche Korrekturen der Partonschauer zu Verteilungen der nicht-führenden Jets gefunden.

Zusätzlich wird das Program REPOLO diskutiert, das entwickelt wurde, um SM-Higgsboson-Ereignisse in VBF umzugewichten. Dadurch können unter anderem anomale Kopplungen des Higgsbosons an SM-Teilchen simuliert oder Signal-Untergrund-Interferenzeffekte berücksichtigt werden, die bei der Suche nach schweren Higgsbosonen eine Rolle spielen.

CONTENTS

CHAPTER 1

INTRODUCTION

All truths are easy to understand once they are discovered,
the point is to discover them.
Attributed to Galileo Galilei

Nowadays, experimental and theoretical High Energy Particle Physics is on the verge of providing one of the missing "truths" of our understanding of nature, the fundamental mechanism giving mass to all known elementary particles. It has been a long, exhausting journey so far which culminated in the formulation of the Standard Model of Particle Physics (SM), which is possibly the most successful theory in the history of physics. In the last century the concept of symmetries emerged as a powerful tool to describe the basic principles of nature. The connection of symmetry transformations and conserved charges has been formulated by Emmy Noether already in 1918 [1, 2]. In quantum field theories like the SM, the invariance of the Lagrangian under local gauge transformations results in conserved charges associated with the underlying gauge group and in additional fields mediating forces among the elementary particles of the theory. Thereby all fundamental interactions contained in the SM can be traced back to the invariance of the Lagrangian under certain symmetry transformations.

The SM is a Yang-Mills theory [3] based on local gauge invariance under transformations of the symmetry group $SU(3)_C \times SU(2)_L \times U(1)_Y$. It describes the strong and electroweak interactions and thereby three of the four fundamental forces of nature. Gravity, the fourth fundamental force, has not yet been achieved to be integrated in the SM to give a description of all known interactions. Quantum Chromodynamics (QCD) [4, 5] describes the strong interactions of the elementary particles carrying the quantum number "color", namely quarks and gluons, commonly referred to as partons. QCD, as an asymptotically free theory, exhibits a huge variety of physical effects related to the running of the strong coupling constant [6, 7], which decreases for high energies and increases rapidly for lower energies. As a consequence, only color singlet bound states of partons, the hadrons, are

observed at large distances. The electroweak sector, formulated in the 1960s by Glashow, Weinberg and Salam [8–10], describes in its earliest version the electroweak interactions of massless quarks and leptons through the exchange of massless force carriers. However, the electroweak gauge bosons $W^{\pm}$ and Z, which mediate the weak interaction, discovered at CERN in 1983 [11–13] are, like the known fermions, massive. A naive introduction of mass terms into the theory would however violate the invariance under electroweak gauge transformations explicitly. A solution to this problem has already been formulated in the 1960s by various authors [14–18]. The proposed mechanism, nowadays called Higgs mechanism, generates masses for gauge bosons and fermions via the spontaneous breaking of the electroweak symmetry by the ground state of the vacuum. In addition, one fundamental scalar particle, the famous Higgs boson, emerges from theory.

The last decades of research in high energy physics have been dedicated to the hunt for the Higgs boson and tremendous theoretical and experimental effort has finally led to the discovery of a new particle with mass around 125-126 GeV at the Large Hadron Collider (LHC) in Geneva by two of the big experiments, ATLAS [19] and CMS [20], in July 2012. One of the major goals of current research is the determination of the properties of this new particle, its spin and CP quantum numbers and its couplings to SM particles. First measurements of these properties have already been obtained with the data collected so far. The new resonance seems to be a CP-even, spin-0 particle with SM-like couplings to gauge bosons and fermions and hence behaves like *the* Higgs boson predicted in the current formulation of the SM. However, the last missing "truth" of the SM, the question whether the spontaneous breaking of the electroweak symmetry is obtained by the minimal form of the Higgs mechanism as incorporated in the SM, is not yet resolved and there is still plenty of room left for physics beyond the SM (BSM), not only in the Higgs sector.

Precise predictions for SM and BSM Higgs boson reactions at the LHC are required in order to further constrain the properties of the discovered boson. To improve leading-order predictions there are basically two approaches, which are valid in complementary energy regimes, namely the calculation of higher-order terms in the perturbative expansion and parton shower corrections. The consideration of next-to-leading order (NLO) corrections in the strong coupling constant is mandatory for a great variety of processes to reduce the theoretical uncertainties of hadron-collider observables to the level of experimental errors. These corrections additionally yield the correct description of one additional hard parton emission. A typical event at the LHC, however, consists of a vast number of hadrons rather than a few partons. The increase of parton multiplicity due to additional soft and collinear emissions from an underlying hard scattering process and the transition of partons to hadrons can be simulated using so-called parton shower Monte Carlo generators. The parton shower implemented in such programs resums the leading infrared logarithms to a hard scattering process.

In this thesis both approaches, parton showers and NLO corrections, have been matched by applying the so-called POWHEG matching scheme [21, 22]. To this end, we have employed the POWHEG-BOX framework [23] and the parton-level Monte Carlo program VBFNLO [24–26] to match various vector-boson fusion (VBF) processes to different parton showers. In VBF two quarks scatter via the exchange of electroweak gauge bosons in the

t-channel, which leads to a very specific event structure with two widely separated hard jets and little hadronic activity in between. This feature can be exploited in experiments to reduce the background stemming from QCD-induced processes.

This thesis is organized as follows: In Chapter 2 we give an introduction to the SM and review the most important aspects of (SM) Higgs physics at the LHC. Chapter 3 comprises an overview of NLO calculations in general and the basic concepts underlying a parton shower algorithm. The matching of these two approaches within the POWHEG framework will be illustrated. Furthermore, the program POWHEG-BOX, which is used throughout this thesis to match NLO predictions to parton showers, is explained.

Chapter 4 contains the first studied processes, W and Z production via VBF. They are matched at NLO accuracy to three different parton showers, to PYTHIA 6 [27], to the standard angular-ordered HERWIG++ parton shower [28–30] and to the fairly new dipole shower implemented in recent versions of HERWIG++ [31, 32]. We will focus on the differences between the three parton shower predictions and discuss the phenomenological implications.

In Chapter 5 we examine the influence of parton shower corrections on Higgs boson production via VBF. We use an effective Lagrangian approach to parametrize deviations of the couplings of the Higgs boson to SM particles in a model-independent way.

The program REPOLO, an add-on to the aforementioned Monte Carlo program VBFNLO, is presented in Chapter 6. REPOLO is able to read in Les Houches event files [33, 34] comprising Higgs production via VBF at LO or NLO and to reweight the individual events to account for different BSM scenarios. Thereby, the process of generating full NLO events and including parton shower and detector simulations for the specific BSM scenario can be circumvented. In addition, REPOLO is capable of simulating signal-background interference effects needed in heavy Higgs boson searches.

In Chapter 7 we discuss the matching of Higgs production via VBF in association with three jets to the parton showers already used before. Special attention is given to the parton shower corrections on the third-hardest jet which for this process has formal NLO accuracy.

Chapter 8 contains a short summary of this work.

CHAPTER 2

THE STANDARD MODEL OF PARTICLE PHYSICS

This chapter is dedicated to the discussion of the foundations of modern high-energy physics, namely the Standard Model of Particle Physics (SM). The SM is reviewed in many textbooks, see e.g. Refs. [35–38]. In this chapter we will use the notation of Ref. [39].

The SM is based on local gauge invariance and describes the electroweak and the strong interaction and thereby three out of the four fundamental forces of nature. The electroweak theory, which will be discussed in Section 2.1, was introduced by Glashow, Salam and Weinberg [8–10] and is based on the $SU(2)_L \times U(1)_Y$ gauge group of the weak left-handed isospin and the hypercharge. The mechanism of breaking the electroweak symmetry down to the electromagnetic $U(1)_Q$ gauge group was introduced by Higgs, Englert, Brout, Guralnik, Hagen and Kibble [14–18] and predicts the existence of the famous Higgs boson as fundamental scalar particle of the theory. This mechanism, nowadays called Higgs mechanism, is the minimal extension of the electroweak theory in order to give masses to fermions and gauge bosons, to restore unitarity [40–43] and to ensure renormalizability [44, 45]. In addition, the $SU(3)_C$ gauge group of Quantum Chromodynamics (QCD) [4, 5], describing the interaction between colored quarks and gluons, is essential for the understanding of reactions at the Large Hadron Collider (LHC) and will therefore be reviewed in Section 2.2. With these fundamental concepts it is possible to calculate cross sections for reactions at the LHC. The most important Higgs boson production modes are described in Section 2.3.

2.1. The Electroweak Sector

Excluding the Higgs boson, which will be discussed later on, the particles of the SM are generally classified into two different groups: fermions with spin 1/2 and gauge bosons or force carriers with spin 1. Temporary, both types of particles are massless. The fermions can be further grouped into three families or generations of quarks and leptons.

Field				I_3	Y	Q
$Q_i =$	$\begin{pmatrix} u \\ d \end{pmatrix}_L$	$\begin{pmatrix} c \\ s \end{pmatrix}_L$	$\begin{pmatrix} t \\ b \end{pmatrix}_L$	$\begin{matrix} 1/2 \\ -1/2 \end{matrix}$	$1/3$	$\begin{matrix} 2/3 \\ -1/3 \end{matrix}$
$u_{R_i} =$	u_R	c_R	t_R	0	$4/3$	$2/3$
$d_{R_i} =$	d_R	s_R	b_R	0	$-2/3$	$-1/3$
$L_i =$	$\begin{pmatrix} \nu_e \\ e^- \end{pmatrix}_L$	$\begin{pmatrix} \nu_\mu \\ \mu^- \end{pmatrix}_L$	$\begin{pmatrix} \nu_\tau \\ \tau^- \end{pmatrix}_L$	$\begin{matrix} 1/2 \\ -1/2 \end{matrix}$	-1	$\begin{matrix} 0 \\ -1 \end{matrix}$
$e_{R_i} =$	e^-_R	μ^-_R	τ^-_R	0	-2	-1

Table 2.1.: The three generations of left- and right-handed quarks and leptons, $f_{L,R} = \frac{1}{2}(1 \mp \gamma_5) f$, with their third component of the weak isospin I_3, their hypercharge Y and their electric charge Q. Neutrinos are assumed to be massless and therefore have only a left-handed component.

The electroweak sector of the SM is a Yang-Mills theory [3] based on the $SU(2)_L \times U(1)_Y$ gauge group of the left-handed weak isospin and the hypercharge. The left-handed fields of each family build an isospin doublet, the right-handed fields are singlets.[1] The fermionic fields and their electroweak quantum numbers are summarized in Table 2.1, where we have used the third component of the weak isospin, I_3, and the hypercharge Y to relate them to the electric charge Q via the Gell-Mann-Nishijima formula

$$Q = \frac{Y}{2} + I_3. \tag{2.1}$$

The electroweak interactions of the fermions and the gauge bosons are described within the Lagrange density

$$\begin{aligned} \mathcal{L}_{\text{ew}} = &-\frac{1}{4} W^a_{\mu\nu} W^{a,\mu\nu} - \frac{1}{4} B_{\mu\nu} B^{\mu\nu} \\ &+ i\bar{L}_i \not{D} L_i + i\bar{e}_{Ri} \not{D} e_{Ri} + i\bar{Q}_i \not{D} Q_i + i\bar{u}_{Ri} \not{D} u_{Ri} + i\bar{d}_{Ri} \not{D} d_{Ri}, \end{aligned} \tag{2.2}$$

where the covariant derivative,

$$D_\mu = \partial_\mu - i g_2 I^a W^a_\mu - i g_1 \frac{Y}{2} B_\mu, \tag{2.3}$$

[1] Since neutrino masses are neglected we omit right-handed neutrino fields.

specifies the interaction of the fermions with the massless gauge bosons B_μ and W^a_μ ($a = 1, 2, 3$) with coupling strengths g_1 and g_2, respectively. The matrices $I^a = \frac{1}{2}\tau^a$ are the three generators of the left-handed weak isospin. The two terms including the field strengths,

$$\begin{aligned} B_{\mu\nu} &= \partial_\mu B_\nu - \partial_\nu B_\mu, \\ W^a_{\mu\nu} &= \partial_\mu W^a_\nu - \partial_\nu W^a_\mu + g_2 \epsilon^{abc} W^b_\mu W^c_\nu, \end{aligned} \tag{2.4}$$

describe the propagation of the force carriers and the self-interactions of the isospin triplet bosons W^a.

Including a mass term of the form $\frac{1}{2} M_V^2 \, W_\mu W^\mu$ in Equation (2.2) would explicitly break the gauge invariance of the Lagrangian. Moreover, mass terms for the fermions,

$$-m_f \bar{\Psi}\Psi = -m_f \left(\bar{\Psi}_R \Psi_L + \bar{\Psi}_L \Psi_R \right), \tag{2.5}$$

are not invariant under $SU(2)_L$ gauge transformations and would therefore break the left-handed isospin symmetry explicitly. However, the electroweak gauge bosons $W^\pm$ and Z discovered at CERN in 1983 [11–13] are massive, likewise the fermions are not massless.

2.1.1. The Higgs Mechanism

A solution to this problem was already introduced in the 1960s by various authors [14–18]. The proposed mechanism, nowadays called Higgs mechanism, generates masses for fermions and gauge bosons via the spontaneous breaking of the electroweak symmetry by the ground state of a newly introduced complex scalar field. Thereby, the W and Z bosons acquire masses, whereas the photon γ remains massless and the $U(1)_Q$ gauge group of Quantum Electrodynamics (QED) remains as an exact symmetry.

In the minimal version of spontaneous symmetry breaking, the electroweak Lagrangian $\mathcal{L}_{\text{ew}}$ as defined in Equation (2.2) is extended by a complex $SU(2)_L$ doublet field Φ with hypercharge $Y = 1$,

$$\Phi = \begin{pmatrix} \phi^+ \\ \phi^0 \end{pmatrix}. \tag{2.6}$$

The renormalizable Lagrangian of a scalar doublet field is generally given by

$$\mathcal{L}_H = \left(D_\mu \Phi\right)^\dagger \left(D^\mu \Phi\right) - \mu^2 \Phi^\dagger \Phi - \lambda \left(\Phi^\dagger \Phi\right)^2. \tag{2.7}$$

The neutral component of Φ acquires a non-zero vacuum expectation value v, which is a necessary condition for spontaneous symmetry breaking, only for negative $\mu^2 < 0$. The parameter λ has to be positive to guarantee the stability of the vacuum. The ground state of the scalar doublet field, Φ_0, within the SM is given by

$$\Phi_0 = \begin{pmatrix} 0 \\ v/\sqrt{2} \end{pmatrix} \text{ with } v = \sqrt{-\frac{\mu^2}{\lambda}} \approx 246 \text{ GeV}. \tag{2.8}$$

The four degrees of freedom of the scalar doublet Φ can be parametrized in terms of three massive would-be Goldstone bosons θ_i, which later on will become the longitudinal polarizations of the massive electroweak gauge bosons in unitary gauge, and one elementary scalar field H with mass $M_H^2 = -2\mu^2$, the Higgs boson,

$$\Phi = \begin{pmatrix} \theta_2 + i\theta_1 \\ \frac{1}{\sqrt{2}}(v + H) - i\theta_3 \end{pmatrix} \xrightarrow{\text{unitary gauge}} \begin{pmatrix} 0 \\ \frac{1}{\sqrt{2}}(v + H) \end{pmatrix}. \tag{2.9}$$

Expanding the scalar Lagrangian defined in Equation (2.7) by the use of Equation (2.9) and after defining the new (physical) fields $W_\mu^\pm$, Z_μ and A_μ for the gauge bosons,

$$W_\mu^\pm = \frac{1}{\sqrt{2}}\left(W_\mu^1 \mp iW_\mu^2\right), \qquad Z_\mu = \frac{g_2 W_\mu^3 - g_1 B_\mu}{\sqrt{g_1^2 + g_2^2}}, \qquad A_\mu = \frac{g_2 W_\mu^3 + g_1 B_\mu}{\sqrt{g_1^2 + g_2^2}}, \tag{2.10}$$

one can read off the mass terms for the gauge bosons, which are bilinear in the fields,

$$M_W = \frac{1}{2} v g_2, \qquad M_Z = \frac{1}{2} v \sqrt{g_1^2 + g_2^2}, \qquad M_\gamma = 0. \tag{2.11}$$

Thereby, the electroweak gauge group $SU(2)_L \times U(1)_Y$ is broken to the electromagnetic $U(1)_Q$ symmetry, whose force carrier is the massless photon.

The mass terms for fermions are integrated in the SM via the Yukawa Lagrangian, which is built of the scalar doublet Φ and the isodoublet $\tilde{\Phi} = i\tau_2 \Phi^*$ with $Y = -1$. The Yukawa Lagrangian reads

$$\begin{aligned} \mathcal{L}_f &= -\lambda_{e,ij} \bar{L}_i \Phi e_{R,j} - \lambda_{d,ij} \bar{Q}_i \Phi d_{R,j} - \lambda_{u,ij} \bar{Q}_i \tilde{\Phi} u_{R,j} + \text{h.c.} \\ &= -\frac{1}{\sqrt{2}} \widetilde{\lambda}_e (v + H)\, \bar{e}_L e_R + \ldots + \text{h.c.}, \end{aligned} \tag{2.12}$$

where the Yukawa matrices $\lambda_{f,ij}$ have to be diagonalized to get the mass eigenstates of the fermions. The mass terms after diagonalization are proportional to the Yukawa couplings $\widetilde{\lambda}_f$,

$$m_f = \frac{\widetilde{\lambda}_f v}{\sqrt{2}}. \tag{2.13}$$

An important implication of the Yukawa Lagrangian in Equation (2.12) is the introduction of flavor mixing in the quark sector, since the mass eigenstates of the fermion fields no longer correspond to their interaction eigenstates with respect to the electroweak W boson. The conversion from interaction to mass eigenstates in the quark sector is parametrized by three mixing angles and one CP-violating phase in the Cabibbo-Kobayashi-Maskawa (CKM) matrix [46, 47].

In summary, the Higgs doublet field introduces mass terms for the gauge bosons (W and Z) and for the fermions. Thereby, one elementary scalar particle emerges from theory, the famous Higgs boson H. Its couplings are proportional to the mass of the respective particle, e.g.

$$g_{Hff} = i\frac{m_f}{v}, \qquad g_{HVV} = -2i\frac{M_V^2}{v}, \qquad g_{HHH} = 3i\frac{M_H^2}{v}. \tag{2.14}$$

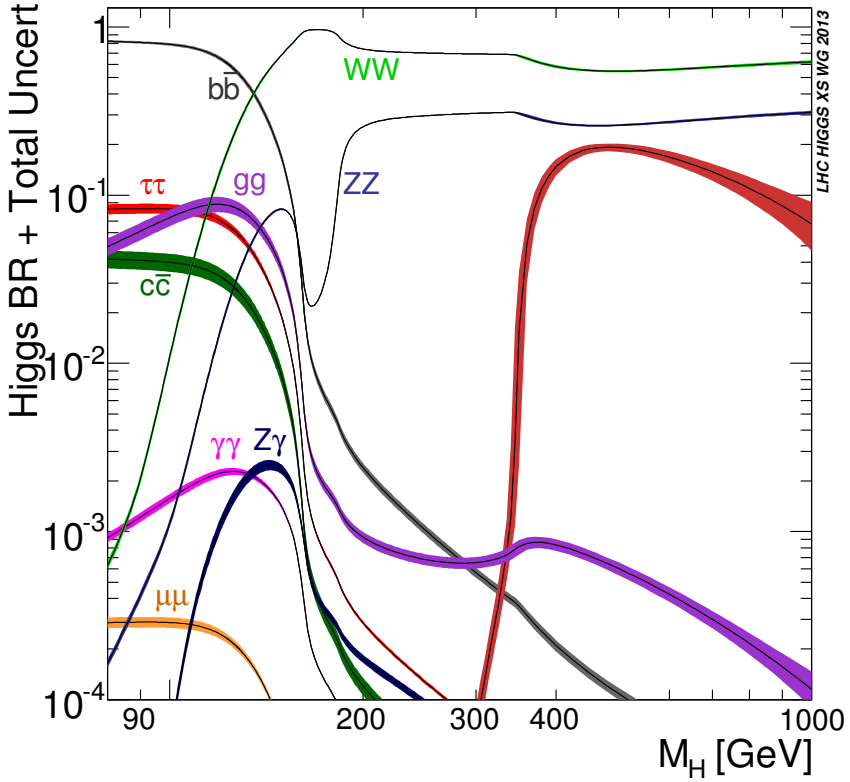

Figure 2.1.: Branching ratio of the SM Higgs boson for the decays into various pairs of SM particles in dependence on the Higgs boson mass M_H. The figure has been taken from Ref. [48].

The branching ratios BR of the Higgs boson for its decays into SM particles, which correspond to the probability that the Higgs boson decays into a specific final state, are displayed in Figure 2.1 in dependence on the Higgs boson mass M_H. The newly discovered boson at the LHC has a mass $M_H \approx 125-126$ GeV [49, 50] and therefore, if it really is *the* SM Higgs boson, predominantly decays into $b\bar{b}$ pairs. The decay of the Higgs boson into two gluons or two photons is mediated via loops of heavy fermions (and the W boson) and is therefore suppressed.

2.2. Quantum Chromodynamics

After having reviewed the electroweak sector, we complement the SM by the illustration of Quantum Chromodynamics (QCD) which is responsible for the strong force. QCD is based on an $SU(3)_C$ gauge group with the new quantum number "color". The eight generators in the fundamental representation, $T^a = \frac{\lambda^a}{2}$, are proportional to the Gell-Mann matrices λ^a. Local gauge invariance results in eight gluon fields G^a_μ, which mediate the strong force. The quarks transform as triplets under the $SU(3)_C$ gauge group, the leptons do not "feel" the strong force and are therefore color singlets.

The Lagrangian of QCD is given by

$$\mathcal{L}_{QCD} = \sum_f \left[i\,\bar{q}_f \not{D}\, q_f - m_f\,\bar{q}_f q_f \right] - \frac{1}{4} G^{a,\mu\nu} G^a_{\mu\nu} \tag{2.15}$$

with the covariant derivative

$$D_\mu = \partial_\mu - i g_s T_a G^a_\mu \tag{2.16}$$

encoding the interaction between gluons and quarks with coupling strength g_s. The field strength tensor for the gluons is given by

$$G^a_{\mu\nu} = \partial_\mu G^a_\nu - \partial_\nu G^a_\mu + g_s f^{abc} G^b_\mu G^c_\nu \tag{2.17}$$

and leads to additional three- and four-gluon vertices, which are a manifestation of the non-abelian structure of QCD. In the Equation (2.17), f^{abc} are the structure constants of the $SU(3)_C$ gauge group.

2.2.1. Asymptotic Freedom and Confinement

Asymptotic freedom implies that the QCD coupling constant, $\alpha_s = \frac{g_s^2}{4\pi}$, is small at short distances. Therefore, quarks and gluons can be treated as free particles within perturbation theory at high energies. On the other side of the energy spectrum, α_s rapidly increases for lower energies and perturbation theory is no longer applicable since quarks and gluons appear only as color-singlet bound states. This effect is known as confinement and its theoretical foundations are still not completely understood, see e.g. the review [51].

However, asymptotic freedom and the running of the strong coupling constant is a well-known feature of non-abelian gauge theories and has been established by Gross, Wilczek and Politzer [6, 7]. The scale dependence of α_s is described by the β-function

$$\beta(\alpha_s) = \mu^2 \frac{\partial \alpha_s}{\partial \mu^2} = \frac{\partial \alpha_s}{\partial \ln \mu^2}, \tag{2.18}$$

where μ denotes the renormalization scale. The β-function is derived from higher-order corrections e.g. to the gluon and quark wave-function renormalization constants and the corrections to the quark-gluon vertex. At the one-loop level the β-function is given by

$$\beta(\alpha_s) = -\alpha_s^2\, b_0 = -\alpha_s^2\, \frac{33 - 2n_f}{12\pi}, \tag{2.19}$$

where n_f denotes the number of active quark flavors at the scale where the β-function is evaluated. Since $\beta(\alpha_s) < 0$, the strong coupling constant decreases when going to higher energies reflecting asymptotic freedom. The evolution of α_s from a reference scale μ_0, where it is measured, to a different scale μ is governed by the solution of Equation (2.18),

$$\alpha_s(\mu^2) = \frac{\alpha_s(\mu_0^2)}{1 + b_0\,\alpha_s(\mu_0^2) \ln\left(\mu^2/\mu_0^2\right)}, \tag{2.20}$$

and resums the leading logarithms in the ratio μ^2/μ_0^2. It is also possible to express the running of the strong coupling constant by the use of a single dimensionful parameter Λ,

$$\alpha_s(\mu^2) = \frac{1}{b_0 \ln\left(\mu^2/\Lambda^2\right)}, \tag{2.21}$$

where, depending on the precise definition, $\Lambda \approx 200$ MeV represents the scale at which the strong coupling constant would diverge within perturbation theory.

2.2.2. Cross Sections at Hadron Colliders

The cross section for two massless partons a and b producing a specific n-particle final state is given by

$$\hat{\sigma}_{ab\to n} = \int \frac{1}{4p_a \cdot p_b} \left|\mathcal{M}_{ab\to n}\left(\Phi_n; \mu_R\right)\right|^2 \mathrm{d}\Phi_n(p_a, p_b; p_1 \ldots p_n). \tag{2.22}$$

The characteristics of the process are encoded in the matrix element $\mathcal{M}_{ab\to n}$, which of course depends on the final-state phase-space variables Φ_n. Additionally, the renormalization scale μ_R enters in the matrix elements as the scale at which the strong coupling constant should be evaluated. Moreover, the residual μ_R dependence may enter due to the inclusion of higher-order effects from perturbation theory, e.g. via the calculation of loop functions. The flux factor is given by $\frac{1}{4p_a \cdot p_b}$. The integration over the final-state particles' momenta can be expressed in terms of the differential phase-space element

$$\mathrm{d}\Phi_n = (2\pi)^4 \, \delta^{(4)}\left(p_a + p_b - \sum_{i=1}^{n} p_i\right) \prod_{i=1}^{n} \frac{\mathrm{d}^3 p_i}{(2\pi)^3 \, 2E_i}. \tag{2.23}$$

After all, as discussed earlier, quarks and gluons are no free particles, but rather bound in hadrons. Due to the asymptotic freedom of the strong coupling constant it is however possible to separate the short-distance partonic process off universal long-distance effects. Thanks to the factorization theorems of QCD [38], the hadronic cross section can be written as

$$\begin{aligned} \sigma &= \sum_{a,b} \int_0^1 \mathrm{d}x_a \, \mathrm{d}x_b \int f_a^{h1}\left(x_a, \mu_F\right) f_b^{h2}\left(x_b, \mu_F\right) \mathrm{d}\hat{\sigma}_{ab\to n}\left(\mu_F, \mu_R\right) \\ &= \sum_{a,b} \int_0^1 \mathrm{d}x_a \, \mathrm{d}x_b \int \mathrm{d}\Phi_n(x_a p_a, x_b p_b; p_1 \ldots p_n) \\ &\qquad \times f_a^{h1}\left(x_a, \mu_F\right) f_b^{h2}\left(x_b, \mu_F\right) \frac{1}{2\hat{s}} \left|\mathcal{M}_{ab\to n}\right|^2 \left(\Phi_n; \mu_F, \mu_R\right). \end{aligned} \tag{2.24}$$

The summation over a and b includes all possible initial-state partons entering the hard subprocess $\hat{\sigma}_{ab\to n}$. The parton distribution functions (PDFs) $f_c^h\left(x_c, \mu_F\right)$ depend on the momentum fraction x_c carried by the parton c relative to the hadron h and the (unphysical) factorization scale μ_F. The momenta of the two incoming hadrons are denoted p_a and p_b. Compared to the partonic cross section, the flux factor is now given by $\frac{1}{2\hat{s}} = \frac{1}{2x_a \, x_b \, s}$, where s denotes the squared hadronic center-of-mass energy. The PDFs contain non-perturbative low-energy effects and therefore have to be fitted to data. The evolution to different scales is perturbative and can be calculated using the Dokshitzer-Gribov-Lipatov-Altarelli-Parisi (DGLAP) equations [52–54].

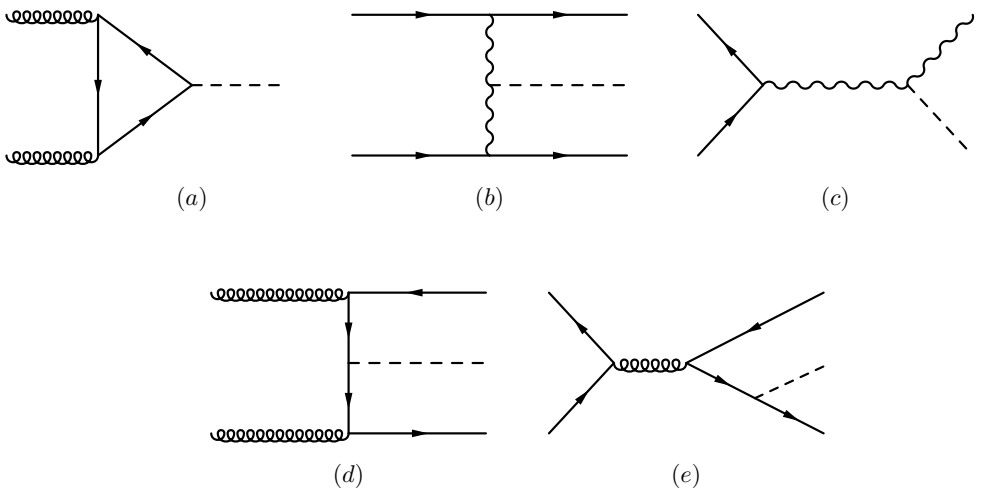

Figure 2.2.: Representative Feynman diagrams for the main production modes of the Higgs boson at the LHC, (a): gluon-fusion through heavy quark loops, (b) vector-boson fusion, (c) Higgsstrahlung off an electroweak gauge boson, (d)–(e) Higgs production in association with a $t\bar{t}$ pair.

2.3. Higgs Boson Production at the LHC

Since the bulk of this work is dedicated to Higgs physics at the LHC, we will now review its most relevant production modes. As we have discussed in Section 2.1.1, the Higgs boson couples proportional to mass. The most important production mechanisms therefore involve heavy particles. Ordered by decreasing cross section at the LHC, they are

- Gluon fusion through heavy quark loops (ggH) (Figure 2.2 (a)),[2]
- Vector- or weak-boson fusion (VBF/WBF) (Figure 2.2 (b)),
- Higgsstrahlung off a W/Z boson (WH/ZH) (Figure 2.2 (c)),
- Production in association with a $t\bar{t}$ pair (ttH) (Figure 2.2 (d)–(e)).

The respective cross sections in dependence on the Higgs boson mass are displayed in Figure 2.3 for the LHC running at a center-of-mass energy of 8 TeV. Gluon fusion is by far the dominant channel. This cross section is known up to next-to-next-to-leading order (NNLO) QCD, both in the heavy top limit and including the finite top mass. The next-to-leading order (NLO) corrections add about +100% to the LO cross section, NNLO QCD corrections add another +50% and even approximate N^{3}LO results account for another +15%, see e.g. Refs [56–59] and references therein. Due to the large uncertainties the calculation of the full N^{3}LO contribution is a topic of current research, see e.g. Refs. [60, 61]. Besides the theoretical uncertainties, ggH is also experimentally challenging since, depending on the decay mode, there are large backgrounds. Moreover, the color structure of ggH leads to an unspecific event structure involving many jets when including additional parton shower effects.

[2]The Feynman diagrams in this work have been drawn using the package FeynMF [55].

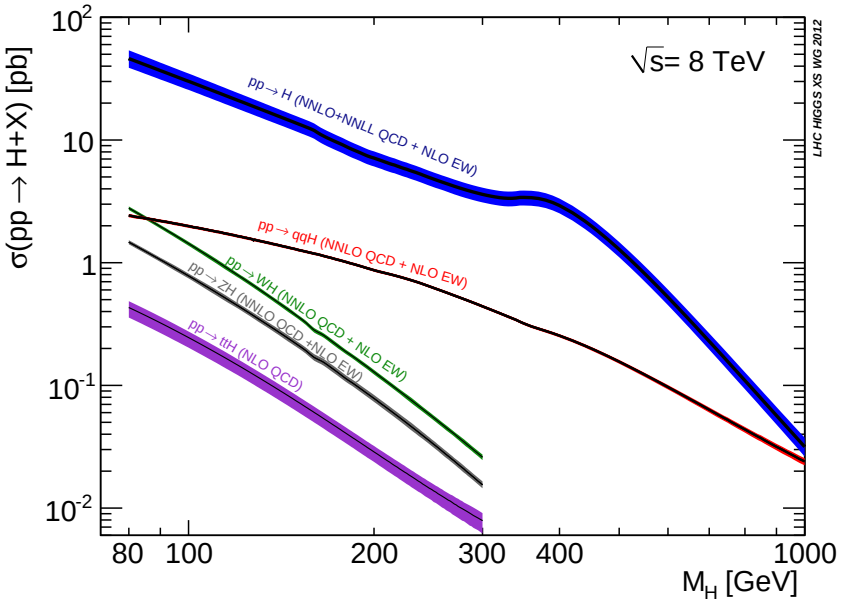

Figure 2.3.: Cross sections for Higgs production at the LHC running at a center-of-mass energy of 8 TeV in dependence on the Higgs mass: ggH (blue), VBF (red), WH (green), ZH (gray) and ttH (violet). The figure is taken from Ref. [48].

Higgs boson production in association with an electroweak gauge boson or a $t\bar{t}$ pair only have had a small influence on the experimental measurements at the LHC with a center-of-mass energy of $\sqrt{s} = 7$ and 8 TeV so far, but will become more relevant after the upgrade of the LHC and the related increase of the center-of-mass energy. The ttH production mode is particularly interesting since it allows for a direct measurement of the top Yukawa coupling.

We will however focus on the VBF production mode, which has the second largest cross section at the LHC. Moreover, a very specific event topology helps to efficiently suppress backgrounds stemming from QCD induced processes. Due to the color-singlet exchange in the t-channel the two jets at LO end up widely separated in rapidity, with the Higgs boson in between. The NLO QCD corrections are of the order of 5-10% [62–64], NNLO QCD and NLO electroweak corrections [65–70] decrease the theoretical uncertainties down to 1-2%. VBF is a promising production channel for measuring the properties and quantum numbers of the Higgs boson at the LHC due to the clean detector signature and the small theoretical uncertainty.

By joint theoretical and experimental effort [56–58] it has been possible to give precise predictions for Higgs physics at the LHC, including inclusive observables and differential distributions, and to formulate strategies for the determination of Higgs properties, like spin and CP quantum numbers. All this has led to the discovery of a new resonance at the LHC [19, 20] with mass $M_H \approx 125 - 126$ GeV, which has SM-like couplings to fermions and gauge bosons and is likely to be a CP-even, spin-0 state [49, 50, 71–84]. The question if this resonance really is *the* Higgs boson of the SM will however not be answered conclusively at the LHC, see e.g. Ref. [85].

CHAPTER 3

MATCHING OF NEXT-TO-LEADING ORDER AND PARTON SHOWER PREDICTIONS

After having reviewed the most important aspects of the SM in the last chapter, with a special focus on Higgs physics, we will now illustrate how precise theoretical predictions for the LHC can be obtained. In Section 3.1 we will shortly introduce the calculation of (differential) observables taking into account higher-order corrections in perturbation theory. Including such NLO (QCD) corrections usually leads to a reduction of the theoretical uncertainties. Other aspects of LHC physics, namely soft and collinear radiation, hadronization and underlying event simulation, are covered by parton shower Monte Carlo generators. The basic concepts of parton showers are explained in Section 3.2. Nowadays, it has become state-of-the-art to match NLO calculations with parton showers to achieve leading-log accuracy for additional radiation. A proper matching can be achieved in two different frameworks, MC@NLO [86] and POWHEG [21, 22]. We will use the latter one throughout this work and we will expound the basic ideas of the POWHEG (POsitive Weight Hardest Emission Generator) method and its implementation in the POWHEG-BOX [23] in Sections 3.3–3.4. In this chapter we will mostly follow the arguments given in Refs. [87, 88].

3.1. Next-to-Leading Order Calculations

To gain high accuracy of cross sections and distributions at hadron colliders, taking into account NLO QCD corrections is mandatory for a great variety of processes to achieve the same accuracy of theoretical predictions and experimental measurements. The cross section for an n-particle final state at NLO consists of three parts, the Born, virtual and real contributions and can schematically be written as

$$\mathrm{d}\sigma_{\mathrm{NLO}} = \Big[B(\Phi_n) + \widetilde{V}(\Phi_n)\Big]\mathrm{d}\Phi_n + R(\Phi_{n+1})\,\mathrm{d}\Phi_{n+1}. \tag{3.1}$$

The Born matrix elements squared, $B(\Phi_n)$, as well as the interference of the Born and virtual amplitude, $\widetilde{V}(\Phi_n)$, depend on the kinematics of the n-particle phase space. The

real-emission part of the cross section contains one additional parton in the final state compared to the Born contributions. In our notation the PDFs are included in the squared matrix elements. The sum over all subprocesses and the integration over the momentum fraction of the two incoming partons are implicit. The divergent terms which are canceled through the renormalization of the PDFs are omitted for the sake of simplicity.

The last two terms of Equation (3.1) are separately infrared (IR) divergent and the virtual part $\widetilde{V}$ additionally contains ultraviolet (UV) divergences. The UV divergences are usually treated via (dimensional) regularization and renormalization of the theory, yielding a UV finite contribution $\widehat{V}$. The IR divergences present in the virtual and real-emission part cancel for IR-safe observables $\mathcal{O}$, which obey

$$\mathcal{O}\Big(\Phi_{n+1}(\Phi_n, \Phi_{\text{rad}})\Big) \to \mathcal{O}\left(\Phi_n\right) \tag{3.2}$$

in the soft and collinear limit, according to the Bloch-Nordsieck [89] and Kinoshita-Lee-Nauenberg [90, 91] theorems for QED and QCD. The $n+1$-particle phase space Φ_{n+1} can be parametrized in terms of the Born phase space Φ_n and three additional integration variables, which describe the phase space for the additional parton of the real-emission contributions, denoted by Φ_{rad},

$$\mathrm{d}\Phi_{n+1} = \mathrm{d}\Phi_n \, \mathrm{d}\Phi_{\text{rad}}. \tag{3.3}$$

The integration boundaries for Φ_{rad} and the Jacobian that is needed for the partitioning of Φ_{n+1} may depend on Φ_n. In the soft or collinear limit, the additional radiation coming from the real-emission contribution cannot be resolved any more due to is low energy or its small angle with respect to one other parton of the underlying Born contribution, which leads to divergences. In standard Monte Carlo generators, as also used in this work, the two IR divergent terms present in Equation (3.1), R and $\widehat{V}$, must be evaluated separately since the final-state multiplicity and therefore the dimension of the phase-space integration differs and the cancellation of the IR singularities between the virtual and real-emission contributions cannot be performed analytically.

A standard procedure to render both virtual and real-emission contributions finite are subtraction algorithms [92–99]. These algorithms exploit the fact that the soft and collinear divergences in R exhibit a universal structure. In order to obtain expressions with the same pointwise divergent behavior as the real contributions, the subtraction terms can be written as the convolution of the respective Born contribution with a universal splitting kernel S that contains the same singularities,

$$C\Big(\Phi_{n+1}(\Phi_n, \Phi_{\text{rad}})\Big) = (B \otimes S)\left(\Phi_n, \Phi_{\text{rad}}\right). \tag{3.4}$$

The local subtraction term C has the same singular behavior as the real - structural form of the splitting kernel can be chosen such that the integration over the additional one-particle phase space can be carried out analytically.

The expectation value for the IR-safe observable $\mathcal{O}$ is obtained from Equation (3.1) by taking into account the respective final state multiplicity and replacing the UV-divergent

virtual contribution $\widetilde{V}$ by the renormalized contribution $\widehat{V}$. Adding the local subtraction term defined in Equation (3.4) to the virtual contribution and subtracting it from the real one renders the NLO result for the observable $\mathcal{O}$ finite,

$$\begin{aligned}\langle\mathcal{O}\rangle &= \int \mathrm{d}\Phi_n \left[B(\Phi_n) + \widehat{V}(\Phi_n)\right] \mathcal{O}(\Phi_n) + \int \mathrm{d}\Phi_{n+1}\, R(\Phi_{n+1})\, \mathcal{O}(\Phi_{n+1}) \\ &= \int \mathrm{d}\Phi_n \left[B(\Phi_n) + \widehat{V}(\Phi_n)\right] \mathcal{O}(\Phi_n) + \int \mathrm{d}\Phi_n \int d\Phi_{\mathrm{rad}}\, C(\Phi_{n+1})\, \mathcal{O}(\Phi_n) \\ &\quad + \int \mathrm{d}\Phi_{n+1}\Big[R(\Phi_{n+1})\, \mathcal{O}(\Phi_{n+1}) - C(\Phi_{n+1})\, \mathcal{O}(\Phi_n)\Big] \\ &= \int \mathrm{d}\Phi_n\Big[B(\Phi_n) + V(\Phi_n)\Big]\mathcal{O}(\Phi_n) + \int \mathrm{d}\Phi_{n+1}\Big[R(\Phi_{n+1})\, \mathcal{O}(\Phi_{n+1}) - C(\Phi_{n+1})\, \mathcal{O}(\Phi_n)\Big].\end{aligned} \tag{3.5}$$

The IR divergences in the n-particle phase space, included in

$$V(\Phi_n) = \widehat{V}(\Phi_n) + \int \mathrm{d}\Phi_{\mathrm{rad}}\, C(\Phi_{n+1}), \tag{3.6}$$

are canceled analytically. The real emission part (the last term in Equation (3.5)) can be integrated using standard Monte Carlo techniques.

NLO calculations reduce the theoretical uncertainties, i.e. the dependence on the (unphysical) renormalization and factorization scale, μ_R and μ_F. The normalization of distributions are changed due to the additional terms in the expansion in α_s. Possible new contributions from additional initial-state particles not present in the Born process but entering in the real-emission part also can lead to large corrections, e.g. gluons in the initial state in Drell-Yan processes only enter in the real-emission contribution. Additionally, jets at high transverse momentum are described accurately. However, the low-$p_{T,j}$ region of the additional radiation originating from the real-emission matrix elements is poorly described, since the transverse momentum is no inclusive observable and the total cross section at NLO diverges in the limit $p_{T,j} \to 0$. Moreover, the whole procedure only yields a parton-level description of the process. Looking at a typical event at the LHC, the multiplicity of partons is, however, very high and the detected particles are hadrons.

3.2. Parton Shower Basics

However, there exists an approach to accurately describe low-p_T jets and exclusive final states at hadron level: Shower Monte Carlo programs (SMC). Such programs, like Pythia 6 [27] or Herwig++ [28–30], which will be used in this thesis, provide the user with all necessary ingredients for a full event simulation. The SMC usually include a huge variety of hard scattering matrix elements and a dedicated shower algorithm which accounts for additional parton emission from the underlying hard scattering process. The resulting partons are afterwards clustered into possibly unstable hadrons, which can further decay into stable particles that can be detected. Additional radiation coming from the underlying event, which describes additional scatterings of the proton remnants not participating in the hard process, is also included in the simulation. We will however focus on the shower algorithm, since we will study the shower effects of different SMC

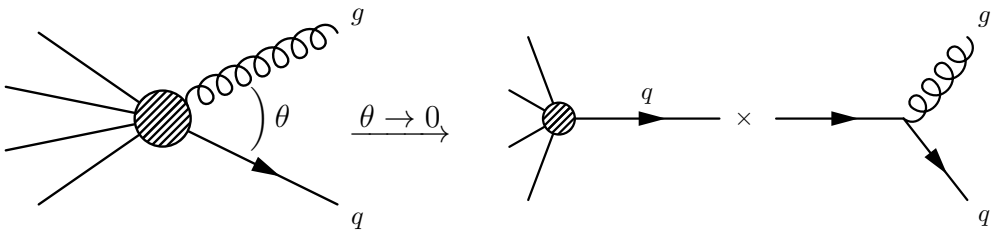

Figure 3.1.: Illustration of collinear factorization for a $q \to qg$ splitting. The dashed circle represents the hard scattering matrix element. The angle between the quark and the gluon is denoted θ.

on vector-boson fusion processes in this work. For an introduction to hadronization and multi-parton interactions we refer to e.g. Ref. [87].

The shower algorithm takes into account the leading IR logarithms which arise from soft and/or collinear partons being emitted from colored particles produced in the hard scattering process. Thereby, the most important QCD effects are included and a description of exclusive final states is possible. The fundamental principle of a shower algorithm is the (collinear) factorization of the cross section into the production of a mother parton i times a splitting function including the emitted parton j in the collinear limit. A pictorial illustration of collinear factorization for the special case of a quark splitting, $q \to qg$, is shown in Figure 3.1. In the plot, θ denotes the angle between the gluon and the emitting quark. The cross section in the collinear limit can be written as

$$\mathrm{d}\sigma_{n+1}\left(\Phi_{n+1}\right) \xrightarrow{\text{collinear limit}} \mathrm{d}\sigma_n\left(\Phi_n\right)\, \mathcal{P}\left(\Phi_{\mathrm{rad}}\right) \mathrm{d}\Phi_{\mathrm{rad}}, \tag{3.7}$$

where the $n+1$-particle cross section σ_{n+1} is factorized into the n-particle cross section and the splitting probability $\mathcal{P}$, which has to be integrated over the additional phase space of the emitted parton, $\mathrm{d}\Phi_{\mathrm{rad}}$.

The probability for the emission of parton j from the mother parton i is given by

$$\mathcal{P}\left(\Phi_{\mathrm{rad}}\right) \mathrm{d}\Phi_{\mathrm{rad}} = \frac{\alpha_s(t)}{2\pi} \frac{\mathrm{d}t}{t} P_{ji}\left(z, \phi\right)\, \mathrm{d}z\, \frac{\mathrm{d}\phi}{2\pi}. \tag{3.8}$$

This equation is again only valid in the collinear limit. The kinematics of the additional parton are expressed in terms of three parameters, ϕ, z and t,

$$\mathrm{d}\Phi_{\mathrm{rad}} = \mathrm{d}t\, \mathrm{d}z\, \frac{\mathrm{d}\phi}{2\pi}. \tag{3.9}$$

The dimensionful variable t vanishes in the collinear limit and parametrizes the angle between the emitter and the emitted parton. It will be chosen later on. The momentum fraction of the parton j relative to the mother parton i is given by the variable z. The concrete definition of z is to some extent arbitrary, as long as it yields the momentum fraction in the collinear limit. The azimuthal angle of the emitted particle j around the axis defined by the emitter i is denoted by the angle ϕ. The P_{ji} are the Altarelli-Parisi splitting functions [53], which depend on the variable z, on the actual splitting ($q \to qg$,

$q \to gq$, $g \to gg$ or $g \to q\bar{q}$) and through the angle ϕ on the spin of the partons involved. The spin-averaged Altarelli-Parisi splitting functions for massless quarks read

$$\begin{aligned} P_{qq}(z) &= C_F \frac{1+z^2}{1-z}, \\ P_{gg}(z) &= C_A \frac{z^4+1+(1-z)^4}{z(1-z)}, \\ P_{gq}(z) &= C_F \frac{1+(1-z)^2}{z}, \\ P_{qg}(z) &= T_R \left(z^2+(1-z)^2\right), \end{aligned} \tag{3.10}$$

where $C_F = \frac{N_c^2-1}{1\,N_c}$ and $C_A = N_c$ are color factors associated with the quarks and gluons, and $T_R = \frac{1}{2}$ is fixed by convention. The functions in Equation (3.10) do not depend on the precise definition of z and t in the collinear limit. Two possible choices for t are

- transverse momentum of j relative to i: $t = k_T^2 = E^2\,\theta^2\,z^2(1-z)^2 + \mathcal{O}(\theta^3)$,
- angular variable: $t = E^2\,\theta^2$,

where E is the energy of the mother parton i.

Since Equation (3.8) holds for any hard process emitting a collinear parton, it is possible to build an iterative algorithm that starts with the hard process, splits off one parton and iterates starting from the $n+1$-particle final state. Thereby, all leading QCD effects associated with collinear emissions can be simulated. However, since all splitting functions, except P_{qg}, contain soft divergences in the limit $z \to 0$ and $z \to 1$, they have to be somehow regularized. This can be achieved by an IR cut-off denoted t_0, which can be interpreted as a resolution criterion for two partons. Therefore, the divergence has no physical effect. This cut-off can be chosen e.g. as a minimum transverse momentum of the emitted parton relative to the emitting parton. The probability for such non-resolvable emissions is then given by the integration of the emission probability from the IR cut-off down to zero and additional virtual contributions to the hard scattering process. There is however an easier way to obtain the probability of non-resolvable emissions, dictated by unitarity: Either a resolvable parton is emitted or not, so the no-emission probability between two scales, t and $t + \mathrm{d}t$, can be written as

$$\begin{aligned} \mathrm{d}\mathcal{P}_{\text{no emission}}\,(t, t+\mathrm{d}t) &= 1 - \mathrm{d}\mathcal{P}\,(t, t+\mathrm{d}t) \\ &= 1 - \frac{\alpha_s(t)}{2\pi}\frac{\mathrm{d}t}{t}\int_{t_0/t}^{1-t_0/t} \sum_j P_{ji}\,(z')\;\mathrm{d}z', \end{aligned} \tag{3.11}$$

where we have inserted Equation (3.8) and have used the spin-averaged splitting functions P_{ji}. Additionally, the ϕ-integration will be omitted from here on since we will for simplicity only consider the spin-averaged splitting functions. The summation over j is taken over all possible splittings of the parton i. The boundaries of the z' integration depend on the precise definition of t and have to be chosen such that the partons are resolvable.

The probability for a parton i to produce no resolvable branching between the scale t and $\bar{t}$ with $t > \bar{t}$ can be written as a splitting of the interval $[\bar{t}, t]$ into a product of n infinitesimal intervals $[t_n, t_n + \mathrm{d}t_n]$. Then one can insert Equation (3.11) and take the limit $N \to \infty$,

$$\begin{aligned}\Delta_i(t, \bar{t}\,) &= \lim_{N\to\infty} \prod_{n=1}^{N} \left(1 - \frac{\alpha_s(t_n)}{2\pi} \frac{\mathrm{d}t_n}{t_n} \int_{t_0/t_n}^{1-t_0/t_n} \sum_j P_{ji}\left(z'\right)\, \mathrm{d}z'\right) \\ &= \exp\left\{-\int_{\bar{t}}^{t} \frac{\mathrm{d}t'}{t'} \frac{\alpha_s(t')}{2\pi} \int_{t_0/t'}^{1-t_0/t'} \sum_j P_{ji}\left(z'\right)\, \mathrm{d}z'\right\}. \end{aligned} \tag{3.12}$$

This is the famous Sudakov factor $\Delta_i(t, \bar{t}\,)$. It includes the leading corrections to the hard process calculated from tree corrections and unitarity. The total probability to produce no resolvable branching down to the IR cut-off t_0 is thus given by

$$\begin{aligned}\Delta_i(t, t_0) &= \exp\left\{-\int_{t_0}^{t} \frac{\mathrm{d}t'}{t'} \frac{\alpha_s}{2\pi} \int_{t_0/t'}^{1-t_0/t'} \sum_j P_{ji}\left(z'\right)\, \mathrm{d}z'\right\} \\ &\approx \exp\left\{-C_F \frac{\alpha_s}{2\pi} \log^2\left(\frac{t}{t_0}\right)\right\}, \end{aligned} \tag{3.13}$$

which resums the leading IR logarithms. The approximate equality is obtained for the special example of $q \to qg$ splittings.

A compact notation for the Sudakov factor defined in Equation (3.12), which we will use later on, has just the lower integration boundary of the t' integration, now labeled with t, as argument,

$$\Delta_S(t) = \exp\left[-\int_t^{t_{\max}} \mathrm{d}t' \int \mathrm{d}z' \, \frac{\alpha_s(t')}{2\pi} \, \frac{1}{t'} \, P(z')\right]. \tag{3.14}$$

The subscript Δ_S indicates that it is the Sudakov factor of the parton shower. The summation over all possible splittings has been included in $P(z)$ and the subscript i has been omitted. The upper boundary for the t' integration has been set to the starting scale of the parton shower, $t_{\max}$. The boundaries of the z' integration are implicit.

So far we have only concentrated on collinear radiation emerging from final-state partons. Another source of logarithmically enhanced contributions are soft gluon emissions. For soft splittings the factorization is only valid at the amplitude level, contrary to the collinear factorization of Equation (3.8). Therefore, interference effects between different amplitudes have in principle to be taken into account and a sequential treatment of soft splittings is a priori not feasible. Due to color coherence it is however possible to include soft splittings in a collinear shower algorithm using the opening angle as evolution parameter. Color coherence describes the effect that gluon emissions from the two legs of a color-connected pair of partons interfere destructively. The net effect of the interference of the two amplitudes, which describe the emission of an additional soft gluon from one or the other partons in Figure 3.2 (*a*), is twofold. The first possibility is that the gluon lies in a cone with an opening angle smaller than θ around one of the color-connected partons (Figure 3.2 (*b*) or (*c*)). It can resolve the color charge of its parent parton. The

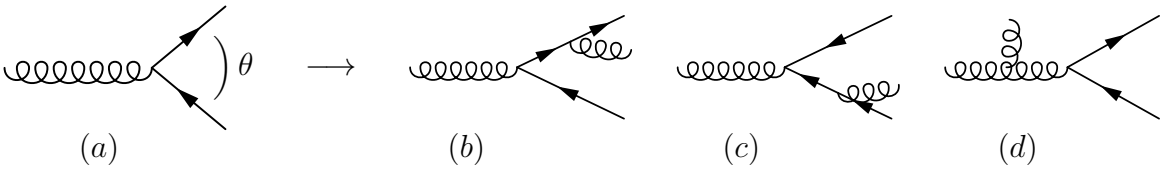

Figure 3.2.: Additional soft gluon emission, the explanation can be found in the text.

other possibility is that the gluon sees only the net color charge of the color-connected pair and is emitted with an opening angle larger than θ. This behavior is equivalent to an emission with an angle larger than θ *before* the splitting in Figure 3.2 (a), as depicted in Figure 3.2 (d). The described interference patterns are correctly taken into account by an angular-ordered shower. Another possibility to include color coherence is a transverse momentum-ordered shower using color dipoles. Initial-state radiation can be included using a backward evolution scheme. The initial-state partons which enter the hard-scattering process are evolved backwards and thereby gain energy with each splitting. For further details we refer to standard textbooks, e.g. Ref. [38].

We have discussed the evolution of the partons produced in the hard process down to the IR cut-off t_0, but still need to define the connection of the parton shower to the hard matrix element and thereby the upper limit or starting scale for the parton shower $t_{\max}$. To avoid double counting that can arise when the shower produces a branching at a scale higher than the typical scale of the hard scattering process, the upper limit of the parton shower evolution should be set to the scale of the hard process. Also, the shower approximation is only valid for low scales. Additionally, the color connections of the partons emerging from the hard scattering process in the $N_c \to \infty$ limit, i.e. the leading color structure, should be considered to account for color coherence effects.

We will now discuss the effect of parton showers on a specific hard scattering process, namely Higgs production via vector-boson fusion (VBF). A sample Feynman diagram for this process at LO has already been shown in Figure 2.2 (b). In Figure 3.3 we show the influence of three different parton showers on the transverse momentum distribution of the hardest jet (left) and on the rapidity of the second hardest jet (right). The input to all three parton showers are 1.5 million unweighted LO events obtained with VBFNLO [24–26], a fully flexible parton level Monte Carlo program for the simulation of, *inter alia*, VBF processes at NLO QCD. In each case, the black curve shows the VBFNLO prediction at LO. The red distributions are obtained using the p_T-ordered PYTHIA shower version 6.4.25 with the Perugia 0-tune (Feb 2009) [27]. The blue curves correspond to the angular-ordered HERWIG++ parton shower version 2.7.0 [28–30] and the turquoise ones to the p_T-ordered HERWIG++ dipole shower [31, 32], which is referred to as DS++ in the following. In the ratio plot, the yellow error band indicates the statistical uncertainty of VBFNLO, the error bars correspond to the statistical uncertainty of the respective shower programs. For all plots shown in this work we have only included the showering stage, i.e. hadronization and underlying event simulations have been omitted.

The input events for the showers have been generated using only mild jet definition cuts ($p_{T_j} > 5$ GeV, $|y_j| < 4.5$) to prevent migration effects. For the plots we have used standard

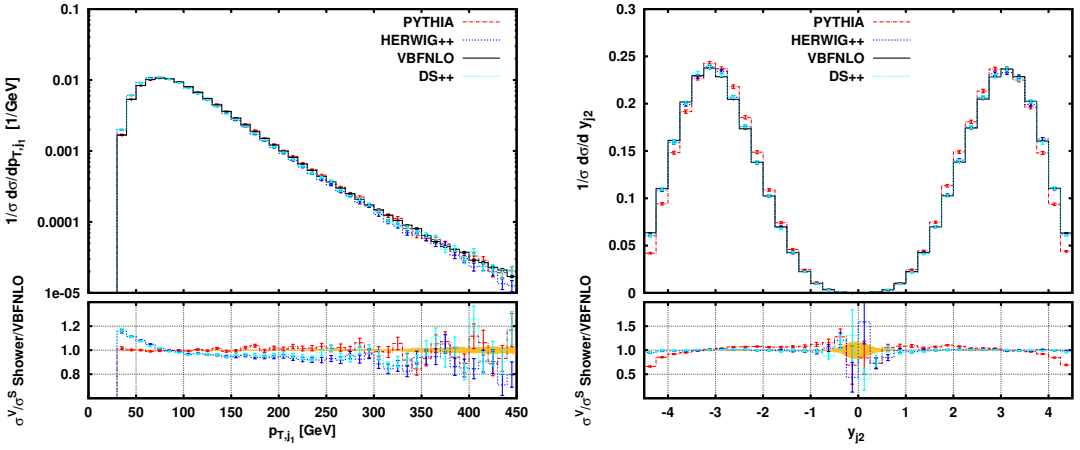

Figure 3.3.: Normalized differential distributions of the transverse momentum of the hardest tagging jet and the rapidity of the second-hardest tagging jet in VBF Higgs production, showered with Pythia, Herwig++ and DS++ (colored lines). The black curves show the original LO distributions obtained with Vbfnlo. The ratio plot shows the deviation of the showered distributions compared to the fixed order ones.

VBF cuts,

$$\begin{array}{lll} p_{T,j} > 20 \text{ GeV}, & p_{T,j}^{\text{tag}} > 30 \text{ GeV}, & |y_j| < 4.5, \\ m_{jj}^{\text{tag}} > 600 \text{ GeV}, & \Delta y_{jj}^{\text{tag}} = |y_1 - y_2| > 4, & y_{j_1} \cdot y_{j_2} < 0. \end{array} \tag{3.15}$$

The two hardest jets are called tagging jets. The respective total cross sections in Figure 3.3 have been factored out since the normalization of the parton showers is only LO accurate. This means that, due to the unitarity of the parton shower, the total cross section without any cuts stays unaltered. Additional radiation however leads to events which will not pass the cuts after the showering stage and therefore reduce the cross section after imposing the VBF cuts given above.

The LO shape of the transverse momentum distribution of the hardest jet is reproduced by Pythia, whereas Herwig++ and DS++ show a shape distortion in the low-p_T region. This discrepancy however just reproduces the shape of the fixed NLO result. The predictions of the two different Herwig++ showers for the rapidity distribution of the second hardest jet are in good agreement and reproduce the fixed-order result. Using Pythia, the jet is located slightly more central.

In VBF, the feature of two widely separated hardest (tagging) jets with little hadronic activity in between is used for the suppression of QCD induced backgrounds. With a so-called central-jet veto (CJV) [100–104] additional radiation in the rapidity gap between the two tagging jets is vetoed. In order to estimate the uncertainty of such a veto, the distributions of additional jets originating from higher-order or shower corrections to VBF have to be known precisely. In Figure 3.4 we therefore show the transverse momentum of the third-hardest jet, which could be a central jet, and its rapidity obtained with the three

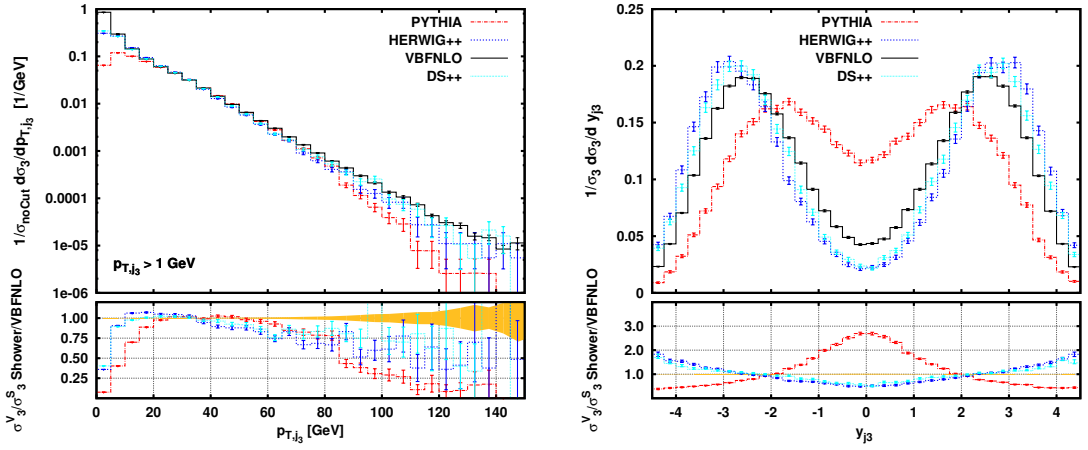

Figure 3.4.: Normalized differential distribution of the transverse momentum of the third-hardest jet and its rapidity. The colored lines show VBF Hjj events showered with PYTHIA, HERWIG++ and DS++ (colored lines), i.e. the third-hardest jet solely is modeled by the respective parton shower. The black curves show the LO distributions for $Hjjj$ production via VBF at LO obtained with VBFNLO. The ratio plot is assigned as in Figure 3.3. For the left plot, the p_{T,j_3} cut has been lowered to 1 GeV, but the cross section with $p_{T,j_3} > 20$ GeV has been used for normalization.

parton showers. They are compared to the LO prediction for Higgs production via VBF in association with three jets obtained with VBFNLO, a sample diagram for this process can be found in Figure 3.5. For the left plot in Figure 3.4, the p_T cut on the non-tagging jets has been lowered to 1 GeV, whereas the standard $p_{T,j} > 20$ GeV cut has been kept for the normalization. Here, the advantage of the shower approach becomes manifest. The low-p_T region is Sudakov suppressed and gives an accurate description of the transverse momentum of the jet down to low values. Contrary to that, the fixed-order prediction diverges in the limit $p_{T,j_3} \to 0$. Overall, the Sudakov damping of PYTHIA is stronger than for the two HERWIG++ showers. On the other end of the transverse momentum spectrum, the showers give a bad description of the jet. Since they only include leading logarithmic effects, the p_T distribution falls off rapidly since the Sudakov factor approaches 1 for $t \to t_{\max}$ and therefore no additional parton splitting is simulated. In this region the matrix elements are better suited to give an accurate prediction.

The striking difference between the two HERWIG++ showers and PYTHIA is visible in the rapidity distribution of the third hardest jet (Figure 3.4, right panel). In PYTHIA much more partons in the central region of the detector are emitted, whereas HERWIG++ and DS++ predominantly emit partons at larger rapidities, closer to the two tagging jets. If one would take the difference between HERWIG++ and PYTHIA as uncertainty estimate for the CJV, the predictive power would be ruined. Additionally, all three shower predictions differ considerably from the fixed-order result.

Therefore it is desirable to match a fixed-NLO calculation with parton showers, on the one hand to benefit both from the accurate normalization and the correct high-p_T jet

behavior and on the other hand to consistently resum the leading IR logarithms. A naive combination of NLO calculations and parton showers would however result in a double counting of radiation, since the parton shower will produce emissions from the Born process, which are also included in the real-emission contributions of the NLO calculation.

3.3. The Powheg Method

One possible solution to the double-counting problem, which will be used in this work, is the POWHEG method [21, 22]. POWHEG is an acronym for POsitive Weight Hardest Emission Generator. We will now review the origin of the double-counting problem and the foundations of the POWHEG approach.

The first emission modeled by the parton shower, starting from an IR-safe observable at LO, is given by

$$\langle \mathcal{O} \rangle_{LO} = \int B\left(\Phi_n\right) \mathrm{d}\Phi_n \Big\{ \Delta_S\left(t^{\min}\right) \mathcal{O}(\Phi_n) + \int_{t_{\min}}^{t_{\max}} \mathrm{d}t' \int \mathrm{d}z' \, \Delta_S\left(t'\right) \frac{\alpha_s(t')}{2\pi} \frac{P(z')}{t'} \mathcal{O}(\Phi_{n+1}) \Big\}, \tag{3.16}$$

The first term in Equation (3.16) is the probability of no resolvable branching of the parton down to the IR cut-off $t_{\min}$. The second term describes one resolvable splitting at the scale t' with $t_{\min} \leq t' \leq t_{\max}$. The boundaries for the z' integration depend on the exact definition of t and z and have been omitted here.

By expanding the Sudakov factor defined in Equation (3.14) in α_s,

$$\Delta_S(t) \approx 1 - \int \mathrm{d}z' \int_t^{t_{\max}} \mathrm{d}t' \, \frac{\alpha_s(t')}{2\pi} \frac{P(z')}{t'}, \tag{3.17}$$

we get the leading terms in in the strong coupling constant. Inserting Equation (3.17) into Equation (3.16) yields for the first splitting

$$\begin{aligned} \langle \mathcal{O} \rangle_{LO}^{PS} \;=\; & \int \mathrm{d}\Phi_n \, B(\Phi_n) \, \mathcal{O}(\Phi_n) - \int \mathrm{d}\Phi_n \, B(\Phi_n) \, \mathcal{O}(\Phi_n) \int_{t_{\min}}^{t_{\max}} \mathrm{d}t' \int \mathrm{d}z' \, \frac{\alpha_s(t')}{2\pi} \frac{P(z')}{t'} \\ & + \int \mathrm{d}\Phi_n \, B(\Phi_n) \int_{t_{\min}}^{t_{\max}} \mathrm{d}t' \int \mathrm{d}z' \, \mathcal{O}(\Phi_{n+1}) \frac{\alpha_s(t')}{2\pi} \frac{P(z')}{t'} + \mathcal{O}(\alpha_s^2). \end{aligned} \tag{3.18}$$

Except for the first term, all contributions given above are formally NLO accurate. Exactly these terms have to be subtracted from an NLO accurate observable to avoid their double counting when acting with a parton shower on it. We therefore start with an IR-safe observable at NLO defined in Equation (3.5) and subtract the second and third term of Equation (3.18),

$$\begin{aligned} \langle \mathcal{O} \rangle_{NLO}^{\mathrm{mod}} \;=\; & \int \mathrm{d}\Phi_n \Big(B(\Phi_n) + V(\Phi_n) \Big) \mathcal{O}(\Phi_n) \\ & + \int \mathrm{d}\Phi_n \, \mathrm{d}\Phi_{\mathrm{rad}} \Big(R(\Phi_{n+1}) \, \mathcal{O}(\Phi_{n+1}) - C(\Phi_{n+1}) \, \mathcal{O}(\Phi_n) \Big) \\ & + \int \mathrm{d}\Phi_n \, B(\Phi_n) \, \mathcal{O}(\Phi_n) \int_{t_{\min}}^{t_{\max}} \mathrm{d}t' \int \mathrm{d}z' \, \frac{\alpha_s(t')}{2\pi} \frac{P(z')}{t'} \\ & - \int \mathrm{d}\Phi_n \int_{t_{\min}}^{t_{\max}} \mathrm{d}t' \int \mathrm{d}z' \, B(\Phi_n) \, \mathcal{O}(\Phi_{n+1}) \frac{\alpha_s(t')}{2\pi} \frac{P(z')}{t'}. \end{aligned} \tag{3.19}$$

Exploiting Equation (3.9), performing the integration over ϕ and a re-arrangement of the terms yields the final result,

$$\begin{aligned}\langle\mathcal{O}\rangle_{NLO}^{\text{mod}} \;=\; & \int \mathrm{d}\Phi_n \Big\{ \Big(B(\Phi_n)+V(\Phi_n)\Big)\,\mathcal{O}(\Phi_n) \\ & + \int_{t_{\min}}^{t_{\max}} \mathrm{d}t' \int \mathrm{d}z'\,\mathcal{O}(\Phi_n)\Big(B(\Phi_n)\,\frac{\alpha_s(t')}{2\pi}\,\frac{P(z')}{t'} - C(\Phi_{n+1})\Big) \\ & + \int_{t_{\min}}^{t_{\max}} \mathrm{d}t' \int \mathrm{d}z'\,\mathcal{O}(\Phi_{n+1})\left(R(\Phi_{n+1}) - B(\Phi_n)\,\frac{\alpha_s(t')}{2\pi}\,\frac{P(z')}{t'}\right)\Big\}. \end{aligned} \tag{3.20}$$

Again, we have kept terms up to $\mathcal{O}(\alpha_s)$. Acting with a parton shower on the modified observable $\langle\mathcal{O}\rangle_{NLO}^{\text{mod}}$ yields by construction NLO accuracy up to terms of $\mathcal{O}(\alpha_s^2)$.

Equation (3.20) can be simplified in two different ways. The first option is known under the name of MC@NLO [86] and will not be considered here. The second option, POWHEG [21, 22], uses

$$\frac{\alpha_s(t)}{2\pi}\,\frac{P(z)}{t} = \frac{R(\Phi_{n+1})}{B(\Phi_n)}, \tag{3.21}$$

which means that in the POWHEG approach the splitting kernels for the first emission are replaced by the ratio of the (singular) real emission contribution and the Born contribution. In the IR limit, the ratio R/B is equivalent to the Altarelli-Parisi splitting kernel. The method is however not restricted to this specific case but can be generalized to arbitrary splitting kernels $K(z,t)$, which are for instance constructed from Catani-Seymour Dipoles [92, 93] like used in DS++ [31, 32].

The first emission is generated according to the POWHEG master formula,

$$\begin{aligned}\mathrm{d}\sigma_{\text{PWG}} = \bar{B}\left(\Phi_n\right)\mathrm{d}\Phi_n \Big\{ & \Delta_{\text{PWG}}\left(\Phi_n, p_T^{\min}\right) \\ & + \Delta_{\text{PWG}}\left(\Phi_n, k_T\right)\,\frac{R\left(\Phi_n,\Phi_{\text{rad}}\right)}{B\left(\Phi_n\right)}\,\Theta\left(k_T - p_T^{\min}\right)\,\mathrm{d}\Phi_{\text{rad}}\Big\}, \end{aligned} \tag{3.22}$$

and takes the form of a standard parton shower step like given in Equation (3.16). The $\bar{B}$-function corresponds to the NLO cross section at fixed underlying Born kinematics Φ_n,

$$\bar{B}\left(\Phi_n\right) = B\left(\Phi_n\right) + V\left(\Phi_n\right) + \int \Big[R\left(\Phi_n,\Phi_{\text{rad}}\right) - C\left(\Phi_n,\Phi_{\text{rad}}\right)\Big]\mathrm{d}\Phi_{\text{rad}}. \tag{3.23}$$

The variables describing the additional emission are given by

$$\mathrm{d}\Phi_{\text{rad}} = \mathrm{d}k_T^2\,\mathrm{d}z\,\frac{\mathrm{d}\phi}{2\pi}. \tag{3.24}$$

The POWHEG Sudakov factor takes the transverse momentum of the emitted particle as evolution variable and reads

$$\Delta_{\text{PWG}}\left(\Phi_n, p_T\right) = \exp\left[-\int \mathrm{d}\Phi'_{\text{rad}}\,\frac{R\left(\Phi_n,\Phi'_{\text{rad}}\right)}{B\left(\Phi_n\right)}\Theta\left(k_T\left(\Phi_n,\Phi'_{\text{rad}}\right) - p_T\right)\right], \tag{3.25}$$

which has the same form as the standard shower Sudakov factor as defined in Equation (3.14), but the splitting functions have been replaced by the real emission contributions over the Born contributions.

Using the POWHEG master formula defined in Equation (3.22), the NLO accuracy of inclusive observables is preserved by construction. Moreover, the first (hard) emission is generated according to the real-emission matrix elements, whereas for soft emissions the leading-log accuracy is preserved due to Equation (3.21).

As has already been stated before, in the POWHEG matching scheme the evolution parameter t is chosen to be the transverse momentum of the emitted parton. Therefore, subsequent radiation handled by a standard parton shower has to be softer than the emitted parton simulated in the POWHEG approach. This is easily achieved for a p_T-ordered shower. For an angular-ordered shower, one has to veto radiation harder than the real emission from POWHEG, since the first emission is not necessarily the hardest one. However, possible soft emissions in an angular ordered shower may be generated in the beginning of the showering algorithm with large angles. These soft, wide-angle partons would be omitted if the veto described above is applied and therefore have to be added back in after the standard shower. Such a parton shower is called truncated vetoed shower. For further details we refer to Refs. [21, 22].

3.4. The Powheg-Box

The POWHEG method described in the last section has been implemented in a publicly available framework called POWHEG-BOX [23], which equips the developer with all needed building blocks to generate the hardest emission according to the POWHEG Sudakov factor defined in Equation (3.25). The POWHEG-BOX code and all available processes can be downloaded from Ref. [105].

The POWHEG-BOX has been used in this thesis to match several VBF processes with parton showers. Therefore, the following building blocks to the program have had to be provided to the program,

1. the flavor structures of the Born and real emission subprocesses,
2. the phase space for the Born process,
3. the Born squared matrix elements $\mathcal{B}$ for each partonic subprocess,
4. the finite part of the interference term between the Born and virtual amplitude,
5. the real emission squared matrix elements,
6. the Born color structure in the limit of a large number of colors.

In the following we review the most important ingredients that have to be implemented. More details can be found in Ref. [23].

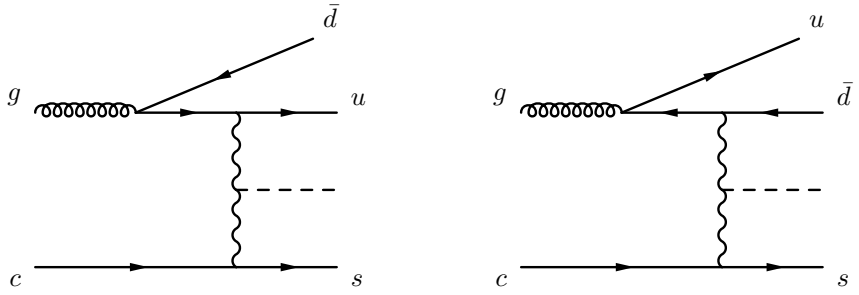

Figure 3.5.: Sample diagrams for a real-emission contribution to Higgs production via VBF.

Flavor Structures

The local subtraction terms needed to render the NLO cross section finite are provided by the POWHEG-BOX in the FKS framework [98, 99]. In FKS, the real emission amplitudes are decomposed into different terms. Each of these terms has at most one divergent soft and/or collinear contribution associated with one parton, the so-called FKS parton. The real emission amplitude squared, which from now on is denoted $\mathcal{R}$, is decomposed according to

$$\mathcal{R} = \sum_i \mathcal{R}_i + \sum_{i,j} \mathcal{R}_{ij}, \tag{3.26}$$

where $\mathcal{R}_i$ denotes the contribution where the FKS parton i is soft and/or collinear to the initial-state partons. For $\mathcal{R}_{ij}$, the FKS parton i is soft/collinear to a final state parton j.

The algorithm to find the singular regions uses the flavor structures of the Born and real-emission processes. As an example we look at Higgs production via VBF. An exemplary flavor structure of a Born subprocess and a corresponding real emission contribution with final-state gluon is given by

$$\left.\begin{array}{ll} \text{Born:} & u\,s \to H\,d\,c \\ \text{real:} & u\,s \to H\,d\,c\,g \end{array}\right\} \text{ 3 regions: } (gd),\ (gc),\ (g0). \tag{3.27}$$

The algorithm within the POWHEG-BOX assigns three singular regions to this process. The gluon as the FKS parton can be soft and/or collinear to the two final state quarks, the corresponding singular regions are denoted (gd) and (gc). Additionally, the gluon can become soft and/or collinear with respect to the two initial-state partons. These (two) singular regions are counted as one and are denoted $(g0)$.

For a real subprocess with a gluon in the initial state, as for example depicted in Figure 3.5,

$$\left.\begin{array}{ll} \text{Born:} & d\,c \to H\,u\,s \\ \text{real:} & g\,c \to H\,u\,s\,\bar{d} \end{array}\right\} \text{ 2 regions: } (gu),\ (g\bar{d}), \tag{3.28}$$

the gluon couples to the upper quark line and can therefore only become soft and/or collinear with respect to the quarks on the same quark line, namely u and $\bar{d}$.

Born Phase Space

The integration routine in the POWHEG-BOX provides an array of real random numbers X_{born} in the range $[0, 1]$. These random numbers are used to calculate the momenta of all particles in the Born process, both in the center-of-mass and in the laboratory frame. Additionally, the Bjorken-x values of the two incoming partons, the squared center-of-mass energy of the Born process and the Jacobian factor,

$$J_{\text{born}} = \left| \frac{\partial \Phi_n}{\partial X_{\text{born}}} \right|, \tag{3.29}$$

have to be provided. The phase space variables for the additional parton in the real-emission part are calculated automatically using three additional random numbers. For processes which exhibit singularities at LO, there are two possibilities to avoid the singular regions, namely generation cuts or Born suppression factors. We will discuss this issue for the processes where it is needed later on.

Born Amplitude

The squared Born matrix elements $\mathcal{B}$ and in addition the color- and spin-correlated Born amplitudes $\mathcal{B}_{ij}$ and $\mathcal{B}_j^{\mu\nu}$ have to be provided. Besides the Born contribution to the NLO cross section, all three amplitudes are needed for the subtraction of the divergences of the squared real-emission matrix elements. The amplitude has to be provided in a form that allows to calculate the Born matrix elements separately for each subprocess defined by the flavor structure.

The color correlated Born amplitude is defined via

$$2s_B \mathcal{B}_{ij} = -N \sum_{\substack{\text{spin,}\\ \text{color}}} \mathcal{M}_{c_k} \left(\mathcal{M}^{\dagger}_{c_k}\right)_{\substack{c_i \to c_i' \\ c_j \to c_j'}} T^a_{c_i, c_i'} T^a_{c_j, c_j'}. \tag{3.30}$$

The flux factor $1/(2s_B)$ should not be included in none of the amplitudes. The Born matrix element $\mathcal{M}_{c_k}$ has $\{c_k\}$ external color indices. The $T^a_{b,c}$ are the color matrices in the fundamental representation for incoming quarks, $T^a_{b,c} = -t^a_{cb}$ for incoming anti-quarks and $T^a_{b,c} = i\, f_{bac}$ for gluons. The normalization factor N can be found in Equation (2.97) of Ref. [22] and contains spin- and color-averaging factors as well as symmetry factors. Due to color conservation, the color-correlated Born amplitudes satisfy

$$\sum_{i, i \neq j} \mathcal{B}_{ij} = C_j \mathcal{B}. \tag{3.31}$$

The sum contains all colored particles in the process. The Casimir invariants for quarks and gluons are given by

$$C_F = \frac{N_c^2 - 1}{2N_c}, \qquad C_A = N_c. \tag{3.32}$$

In addition, for the cancellation of collinear divergences associated with a gluon, the spin-correlated Born amplitudes are needed. In the used convention they are only non-vanishing if the jth parton is a gluon. These squared amplitudes are obtained by leaving the Lorentz index of the gluon uncontracted,

$$\mathcal{B}_j^{\mu\nu} = -N \sum_{\{i\},s_j,s_j'} \mathcal{M}\left(\{i\},s_j\right) \mathcal{M}^\dagger \left(\{i\},s_j'\right) \left(\epsilon_{s_j}^\mu\right)^* \epsilon_{s_j'}^\nu. \tag{3.33}$$

The polarization vectors are normalized to

$$\sum_{\mu,\nu} g_{\mu\nu} \left(\epsilon_{s_j}^\mu\right)^* \epsilon_{s_j'}^\nu = -\delta_{s_j s_j'}, \tag{3.34}$$

where s_i denotes the spin of the ith particle. Exploiting the normalization defined in Equation (3.34) yields

$$\sum_{\mu,\nu} g_{\mu\nu}\, \mathcal{B}_j^{\mu\nu} = -\mathcal{B}. \tag{3.35}$$

Equations (3.31) and (3.35) can be used to test the color- and spin-correlated amplitudes and therefore yield a first check of their implementation. Another check is the cancellation of the divergences in the soft and collinear limit.

Virtual Amplitude

The finite part of the interference between virtual and Born matrix elements, $\mathcal{V}_{\text{fin}}$, has to be provided in conventional dimensional renormalization (CDR). The UV-finite interference terms between the Born and renormalized virtual matrix elements, $\mathcal{M}_B$ and $\mathcal{M}_V$, exhibit a universal structure and for massless partons read

$$\mathcal{V}_b = 2\,\text{Re}\left[\mathcal{M}_V \mathcal{M}_B^*\right] = \mathcal{N}\left[-\sum_i \left(\frac{C_{f_i}}{\epsilon^2} + \frac{\gamma_{f_i}}{\epsilon}\right)\mathcal{B} + \frac{1}{\epsilon}\sum_{\substack{i,j \\ i\neq j}} \ln\left(\frac{2k_i\cdot k_j}{Q^2}\right)\mathcal{B}_{ij} + \mathcal{V}_{\text{fin}}\right], \tag{3.36}$$

with

$$\gamma_q = \frac{3}{2}C_F \qquad \text{and} \qquad \gamma_g = \frac{11}{6}\,C_A - \frac{2}{3}T_R\,n_f. \tag{3.37}$$

The Casimir invariants are defined in Equation (3.32) and n_f denotes the number of active quark flavors. The sum includes all colored partons in the initial and final state. The finite part of the interference between the Born and virtual matrix elements depend on the renormalization scheme (CDR) and on the normalization constant $\mathcal{N}$ in Equation (3.36). The constant $\mathcal{N}$ in the POWHEG-BOX convention is given by

$$\mathcal{N} = \frac{(4\pi)^\epsilon}{\Gamma\left(1-\epsilon\right)}\left(\frac{\mu_R^2}{Q^2}\right)^\epsilon. \tag{3.38}$$

The scale Q is arbitrary and chosen as $Q = \mu_R$.

After adding the integrated FKS dipoles to Equation (3.36) to render the cross section finite, the virtual contributions are given by

$$\mathcal{V} = \frac{\alpha_s}{2\pi}\left(\mathcal{Q}\mathcal{B} + \sum_{\substack{i,j,\\ i\neq j}} \mathcal{I}_{ij}\mathcal{B}_{ij} + \mathcal{V}_{\text{fin}}\right), \tag{3.39}$$

where the factors $\mathcal{Q}$ and $\mathcal{I}_{ij}$ depend on the flavors and momenta of the partons in the process. The functional form of the two factors can e.g. be found in Equation (2.100) and (2.101) of Ref. [22].

Real Amplitude

As for the other squared amplitudes, the real contributions have to be provided such that every flavor structure can be calculated individually. The POWHEG-BOX assigns the singular regions and splits the real contributions into different regions (see Equation (3.26)) automatically. In each singular region, the respective FKS counterterms are added. Before running the actual code, it is checked whether the FKS counterterms and the real contributions cancel in the soft and/or collinear limit in each singular region. This provides a strong check for the assignment of the IR divergent regions and thereby for the flavor structures. Additionally, all Born (correlated) amplitudes can be verified simultaneously since they enter the FKS subtraction terms.

Born Color Structures

The leading Born color structures are needed for the assignment of the color structures including additional radiation. The algorithm within the POWHEG-BOX starts with the Born color structure and assigns the (leading) color to the emitter-emitted pair acting on the assumption of a collinear splitting. In the planar limit this procedure yields a unique color assignment, except for the case of $g \to gg$ splittings which leads to two leading color structures with equal probability. One of the two color structures is then chosen randomly.

In this chapter we have reviewed the most important aspects of NLO and parton shower corrections. These two approaches can be combined within the POWHEG method to accurately describe the first emission from a hard underlying process and to take further radiation emerging from parton showers into account. The POWHEG method has been implemented into the publicly available POWHEG-BOX framework. The program takes the standard building blocks of an NLO calculation as input and supplies Les Houches event files [33, 34] which can be interfaced to transverse-momentum ordered or vetoed truncated angular-ordered parton showers. The POWHEG-BOX has been used in this thesis to match several VBF processes to parton showers, namely electroweak gauge boson production, Higgs boson production with anomalous couplings and Higgs boson production in association with three jets, all at NLO accuracy. The details of the implementation and phenomenological results are described in the following chapters.

CHAPTER 4

ELECTROWEAK GAUGE-BOSON PRODUCTION VIA VECTOR-BOSON FUSION

After having reviewed the most important aspects of the matching between parton showers and NLO calculations, we will now discuss the first processes considered in this thesis, namely electroweak gauge-boson production via vector-boson fusion. The work presented in this chapter has been published in *JHEP* **1304** (2013) 057 [106].

4.1. Introduction

After the discovery of a Higgs-like boson at both ATLAS [19] and CMS [20], we have taken one step closer towards the understanding of electroweak symmetry breaking. As already mentioned in Section 2.3, vector-boson fusion (VBF) is an important production mode of the Higgs boson. Before discussing Higgs production in VBF in detail in Chapters 5–7, we begin our discussion with three related processes: W^+, W^- and Z production in VBF, where the latter has already been measured by CMS [107, 108] and ATLAS [109].

Generally, VBF results in a very specific detector signature. Due to the color singlet exchange in the t-channel, the two hardest jets are widely separated in rapidity and usually lie in opposite detector hemispheres. This feature, as mentioned before, can be used for an efficient suppression of QCD-induced backgrounds. Additionally, a so-called central-jet veto (CJV) [100–104] can be applied. With this special cut no hard jets in the rapidity gap between the two tagging jets are allowed. Therefore, the distributions of the additional sub-leading jets need to be known precisely to estimate the theoretical uncertainties of the CJV. In order to get an accurate simulation of the distribution of the third hardest (first sub-leading) jet, which could be a central jet, the matching of an NLO prediction and a full shower simulation is desirable. Such a matched calculation will be discussed in the following.

Since the cross section for electroweak gauge-boson production via VBF is higher than for the SM Higgs boson and the final state is substantially simpler than in the Higgs

boson case, W and Z production via VBF can be used to test the theoretical predictions before moving on to the Higgs boson process (see Ref. [110]). Additionally, electroweak gauge-boson production via VBF can be used to study deviations of the triple gauge-boson couplings from their SM value [111, 112]. To detect such a deviation, the SM prediction has to be known very precisely. Therefore, we have implemented W and Z production in VBF with subsequent leptonic decays into the first and second generation in the POWHEG-BOX [23] to give an NLO prediction which can be interfaced with parton showers. The fixed-order α_s corrections to the cross section have already been calculated in Ref. [113] and the NLO electroweak corrections are known as well [114]. VBF Z production has already been interfaced to parton showers by using the POWHEG-BOX [115]. The QCD-induced Zjj and Wjj production modes [116, 117] are also part of the POWHEG-BOX [118, 119] and can be used to test the efficiency of VBF cuts for background suppression.

One goal of this work is to gain experience in interfacing an existing NLO code at fixed order in α_s with the POWHEG-BOX. Electroweak gauge boson production via VBF offers enough complexity to study the compatibility of the POWHEG-BOX and parts of the VBFNLO framework [24–26], a fully flexible parton-level Monte Carlo program for cross sections and distributions at NLO accuracy. One important aspect of the study is the analysis of the dependence of the presented processes on the parton shower. To this end, we explore the influence of the p_T-ordered shower in PYTHIA 6 [27] as well as the vetoed, angular-ordered shower in HERWIG++ [28, 29] and the fairly new p_T-ordered HERWIG++ Dipole Shower [31, 32], in the following referred to as DS++. From these predictions we can estimate the influence of missing soft wide-angle radiation (truncation) in the angular ordered shower.

This chapter is organized as follows: In Section 4.2 we review the details of the numerical calculation of all three processes, focusing on the subtleties of the matching between VBFNLO and the POWHEG-BOX. In Section 4.3 we show results of our calculation, showered with PYTHIA, HERWIG++ and DS++. We conclude in Section 4.4.

4.2. Elements of the Implementation

The processes under consideration are $pp \to l^+\nu_l\, jj$, $pp \to l^-\bar{\nu}_l\, jj$ and $pp \to l^+l^-\, jj$ with $l = \mu, e$, which are at $\mathcal{O}(\alpha^4)$ at LO. Contributions from $q\bar{q}$ annihilation with a hadronically decaying gauge boson are treated as part of diboson production and therefore disregarded. The processes will be referred to as electroweak Vjj production or V production via VBF ($V = W^\pm$ or Z). They are quite similar concerning the contributing Feynman diagrams and the phase-space integral, which has to be solved. Therefore we delineate their properties using the example of electroweak W^+jj production.

As described in Section 3.4, the publicly available POWHEG-BOX framework [23] equips the developer with all needed subroutines to go from a fixed-order NLO calculation in QCD to event files in the Les Houches format [33, 34] which then can be interfaced with a truncated parton shower. We have used this framework for the implementation of electroweak Vjj production. In the following we discuss some aspects of the implementation in detail.

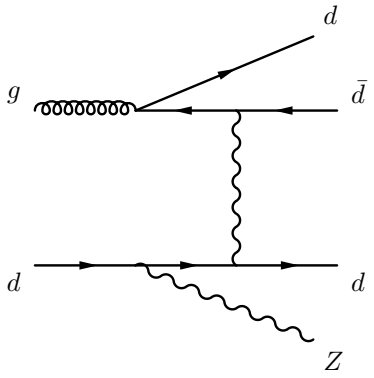

Figure 4.1.: Real-emission diagram contributing to VBF Z production.

4.2.1. Flavor Structures

One subtlety in the implementation arises from the IR subtraction terms. These terms are provided by the POWHEG-BOX in the FKS framework [98, 99] and are calculated automatically using the flavor structures of the Born and real-emission subprocesses.

If one considers the real-emission diagram for VBF Z production depicted in Figure 4.1, the two d quarks in the final state should be kept distinct, since due to the color-singlet exchange in the t-channel, only the d quark on the upper quark line leads to a collinear singularity. The algorithm to find the singular regions in the POWHEG-BOX, however, uses just the combinatorics and assigns two singular regions to the diagram, one for each d quark being collinear to the incoming gluon. This behavior is due to the POWHEG-BOX expecting flavor structures that are already symmetrized with respect to the final-state particles. A solution to this problem is described in Ref. [120]: With the so-called tagging, same flavor fermions on the upper and lower quark line internally get a different flavor (tag) to keep them distinct. These tags are only used to assign the possible radiation regions, which are searched for automatically within the POWHEG-BOX.

4.2.2. Matrix Elements

The matrix elements have been adopted from the VBFNLO implementation explained in detail in Ref. [113]. We will discuss the most important aspects of their implementation in the POWHEG-BOX by means of the process $pp \to l^+\nu_l\, jj$. As has been stated before, diagrams containing $q\bar{q}$ annihilation (see Figure 4.2, sample diagrams (a) and (b)), which we call diboson or WV production with one vector boson decaying hadronically, are disregarded since their contribution is negligible when imposing typical VBF cuts [113].

Using this definition of the process seven types of diagrams contribute to Vjj production via VBF at LO. For W^+ production via VBF, seven sample diagrams are depicted in Figure 4.2 (c)–(i), where due to charge conservation only the structure (e) or (f) contributes for a given flavor structure. Five of the shown topologies (Figure 4.2 (c)–(g)) consist of resonant production of the vector boson with leptonic decay. We account for spin correlations of the final-state leptons and off-shell effects of the gauge bosons through a modified version of the complex-mass scheme [121] with real $\sin^2\theta_W$ and a Breit-Wigner

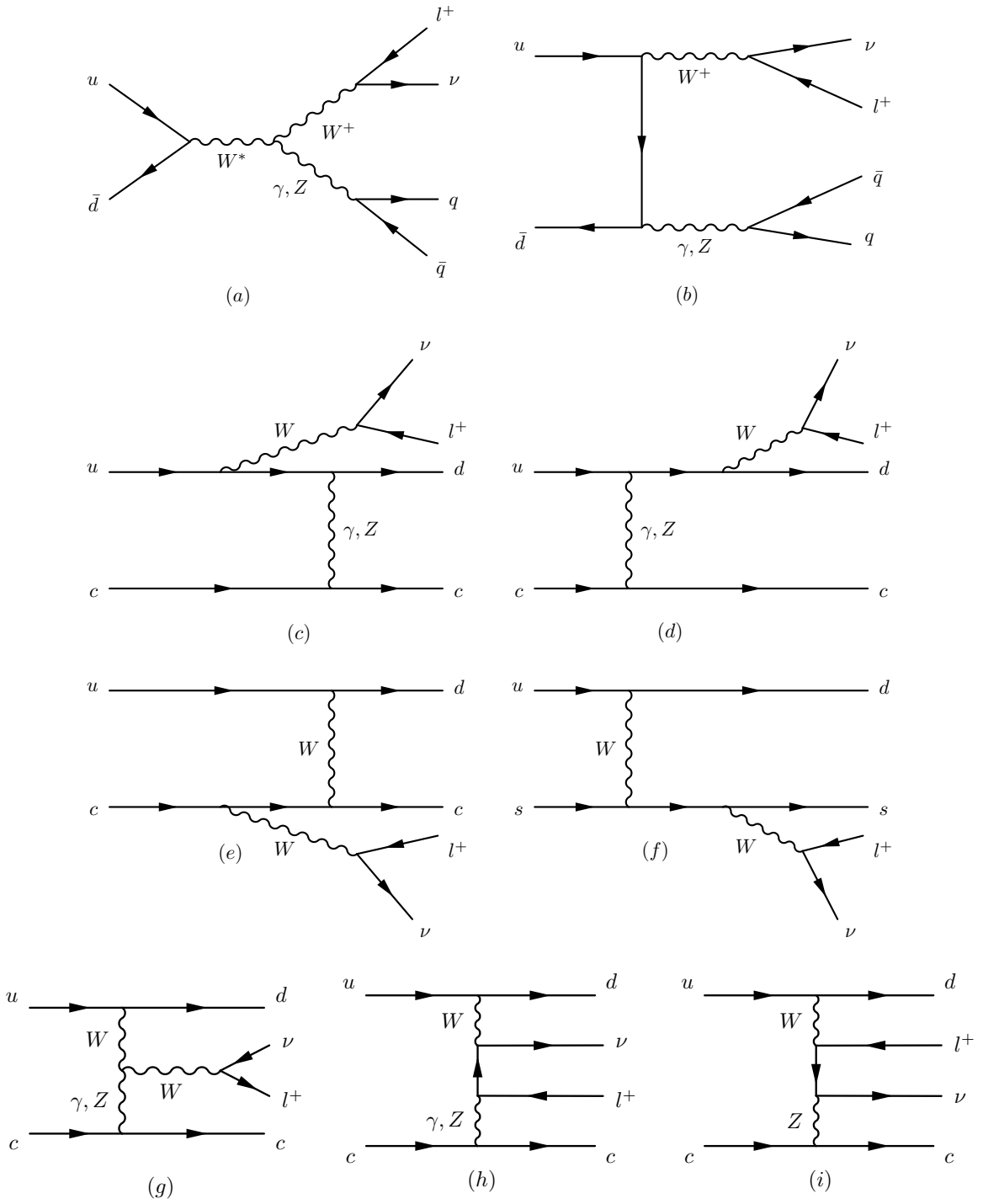

Figure 4.2.: Possible diagrams contributing to $pp \to l^+\nu_l\, jj$ at $\mathcal{O}(\alpha^4)$. The first two diagrams ((a), (b)) are categorized as contributions to diboson production and are neglected (see text for details). The other diagrams display seven possible tree-level contributions considered in W^+ production in VBF, where depending on the flavor structure, only (e) or (f) arises. Diagrams (c)–(g) show resonant graphs. Non-resonant graphs like (h) and (i) have also been included.

integration of the propagator over the whole phase space. In addition to the resonant diagrams, the process comprises non-resonant diagrams like shown in Figure 4.2 (h) and (i).

We neglect fermion masses and contributions from b quarks. Furthermore, the Cabibbo-Kobayashi-Maskawa (CKM) matrix is set to the unit matrix. Due to the unitarity of the CKM matrix, this is no approximation to the calculation as long as the flavor of the jets is not tagged and the third-generation fermions are omitted.

The diagram topologies for electroweak Zjj production are analogous to those shown in Figure 4.2 for Wjj production via VBF. Since leptonic decays are included in the calculation, also the contributions of charged leptons emerging from the decay of off-shell photons are taken into account.

As illustrated in Section 3.4, the spin- and color-correlated Born matrix elements are needed to construct the FKS subtraction terms. The spin-correlated Born matrix elements as defined in Equation (3.33) vanish since in the used convention they only contribute if there are external gluons at tree level. The color-correlated amplitudes are

$$\mathcal{B}_{ij} = \begin{cases} C_F\,\mathcal{B} & \text{if quarks } i \text{ and } j \text{ are on the same quark line,} \\ 0 & \text{otherwise.} \end{cases} \tag{4.1}$$

Here, $\mathcal{B}$ denotes the squared Born matrix element.

In Figure 4.3, possible real-emission topologies with initial-state gluons are depicted. Both virtual vector bosons illustrated in diagrams (a) and (b) are time-like and contain one vector boson that decays into a quark-anti-quark pair. This is a real-emission contribution to WV production and, as stated before, therefore treated as a separate process, which is not considered here. Figures 4.3 (c) and (d) show two valid topologies which are taken into account. Final-state gluon diagrams can be obtained by crossing.

Already at LO, up to two t-channel photons are present in electroweak Vjj production. Consequently, the Born cross section diverges if integrated over the whole available phase space. However, the cross section is well defined when requiring two jets fulfilling minimal jet-definition criteria. To eliminate the singularities arising without the requirement of two observable jets, amplitudes with a t-channel photon with a low virtuality of $Q^2 < 4\,\mathrm{GeV}^2$ are suppressed with a large damping factor of 10^{-20}, as used in Ref. [115]. At NLO, requiring two observable jets does not render the cross section finite due to an additional collinear divergence caused by the t-channel photon exchange, which is absorbed via the photon PDF. In our approach, we impose the aforementioned $Q^2 < 4\,\mathrm{GeV}^2$ suppression and replace the missing piece by $p\gamma \to VjjX$ production. In the following the missing $p\gamma \to VjjX$ piece is considered as a separate electroweak contribution to Vjj production and, since these contributions are quite small when typical VBF cuts are imposed, they have been neglected.

The virtual corrections consist of vertex and box diagrams. The finite terms of the inter-

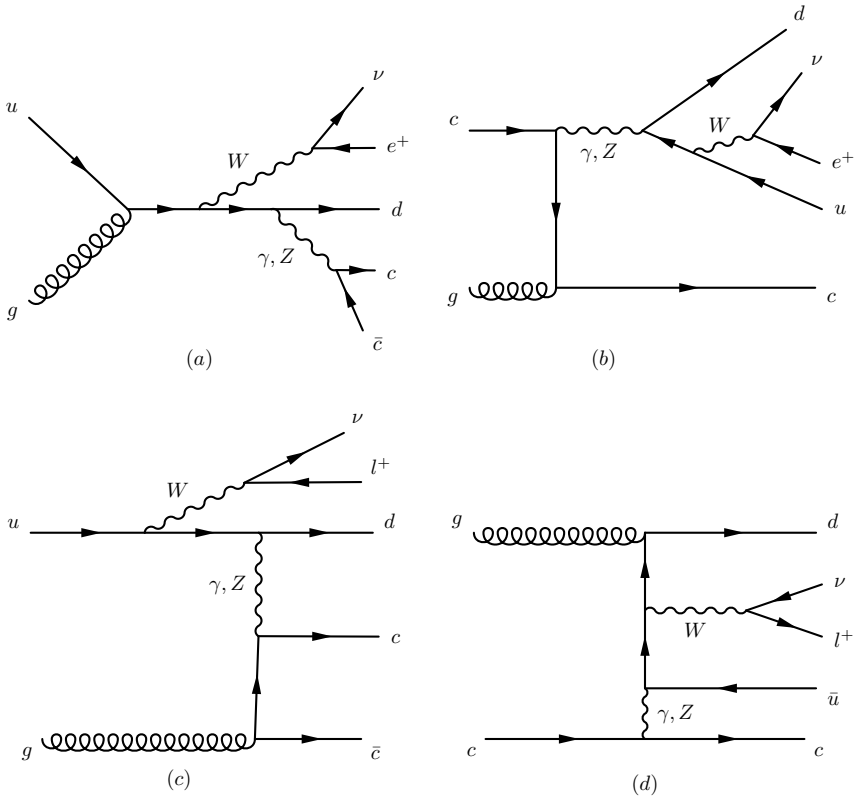

Figure 4.3.: Real-emission diagrams for W^+ production via VBF: (a) and (b) are strongly suppressed in the VBF region and are treated as a different process not investigated here, (c) and (d) show sample diagrams for gluon-induced amplitudes. Diagrams with final-state gluons are obtained by crossing.

ference between Born and virtual contributions read [113]

$$\begin{aligned}\mathcal{V}_{\text{fin}} &= C_F \left(-\ln^2\left(\frac{\mu_R^2}{s_{21}}\right) - 3\ln\left(\frac{\mu_R^2}{s_{21}}\right) - \ln^2\left(\frac{\mu_R^2}{s_{43}}\right) - 3\ln\left(\frac{\mu_R^2}{s_{43}}\right) - 16 \right) |\mathcal{M}_B|^2 \\ &+ 2\,\text{Re}\left[\mathcal{M}_B^* \,\widetilde{\mathcal{M}}_V\right], \end{aligned} \tag{4.2}$$

where the appropriate normalization used in the POWHEG-BOX (see Equation (2.92) from Ref. [22] or Equation (3.38)) has been factored out. $\mathcal{M}_B$ denotes the Born matrix element, $\widetilde{\mathcal{M}}_V$ are the finite terms originating from box corrections. Here, μ_R is the renormalization scale, s_{21} and s_{43} are the time-like squared momenta of the exchanged weak bosons (W, Z or γ) in the t-channel.

4.2.3. Phase Space

As already mentioned in the last section, for Zjj production via VBF we include virtual photons decaying into massless leptons, which leads to a singularity. Therefore, we require the invariant dilepton mass to be higher than 20 GeV. In addition, the cross section for all three considered processes is only well defined when imposing standard jet definition

cuts. Therefore, the integration over the phase-space variables has to be restricted to guarantee meaningful results. We have implemented three different procedures to cure these singularities in the Born phase-space integral.

The first procedure is adopted from Ref. [115] and maps the random numbers given by the integration routine to the physical momenta of the partons. To avoid divergent Born contributions, the user can impose cuts on the transverse momentum of the two partons in the final state. This option is not recommended since this hard cut in the phase space may influence the final showered result, which should not be sensitive to this generation cut.

An alternative option for a phase space with divergent Born contributions has been introduced in Ref. [122]. There, a so-called Born suppression factor $F(\Phi_n)$ is used to suppress the generation of momenta in the singular underlying Born configurations. The underlying Born kinematics are then generated in the POWHEG-BOX according to a modified $\bar{B}_{\text{supp}}$ function,

$$\bar{B}_{\text{supp}} = \bar{B}(\Phi_n)\, F(\Phi_n). \tag{4.3}$$

The Born suppression factor $F(\Phi_n)$ has to be chosen such that the resulting $\bar{B}_{\text{supp}}$ is integrable. As a consequence, only weighted events can be generated, since for every phase-space point the factor $F(\Phi_n)$ has to be divided out again. A suitable parametrization of $F(\Phi_n)$, which has already been used in Ref. [115], is

$$F(\Phi_n) = \left(\frac{p_{T,j_1}^2}{p_{T,j_1}^2 + \Lambda_{p_{T_j}}^2}\right)^k \left(\frac{p_{T,j_2}^2}{p_{T,j_2}^2 + \Lambda_{p_{T_j}}^2}\right)^k, \tag{4.4}$$

where the p_{T,j_i} denote the transverse momenta of the final-state partons. The two parameters $\Lambda_{p_{T_j}}$ and k can be changed by the user, with default values of 10 GeV and 2, respectively. With this definition, $F(\Phi_n)$ suppresses the generation of partons with small transverse momenta. An examination of the generation cut and the Born suppression factor for dijet production can be found in Ref. [123].

The third procedure for the phase-space integration uses LO unweighted events as phase-space generator. These unweighted events are already flat in the Born phase space and therefore serve as a perfect LO phase-space generator. Consequently, the optimization of the grid for the underlying Born kinematics can be omitted and only the real-emission variables have to be optimized during the Monte Carlo integration. This procedure also speeds up the generation of POWHEG events. Here, we use unweighted events generated by VBFNLO. However, the unweighted input events have to be provided with a different weight to guarantee the correct normalization of the cross section. In a Monte Carlo integration the LO cross section is calculated as

$$\sigma_{\text{LO}} = \frac{1}{N}\sum_{i=1}^{N} J_i \left|\mathcal{M}_B\left(\Phi_n^{(i)}\right)\right|^2 \text{pdf}\left(\Phi_n^{(i)}\right) = \frac{1}{N}\sum_{i=1}^{N} J_i\, \mathcal{M}_{B,\text{pdf}}^2\left(\Phi_n^{(i)}\right), \tag{4.5}$$

where $\mathcal{M}_{B,\text{pdf}}^2(\Phi_n^{(i)})$ denotes the numerical value of the squared Born matrix element including PDFs using the kinematics of the phase-space point i, and J_i is the Jacobi factor.

$\mathcal{M}^2_{B,\mathrm{pdf}}(\Phi_n^{(i)})$ is calculated within the POWHEG-BOX, so the Jacobi factor has to be provided as the reweighting factor for the input events. It is given by

$$J_i = \frac{\sigma_{LO}}{\mathcal{M}^2_{B,\mathrm{pdf}}\left(\Phi_n^{(i)}\right)}. \tag{4.6}$$

We have used this third method for the numerical analysis presented in Section 4.3, unless not stated otherwise.

4.2.4. Checks and Comparisons

To ensure that the results shown in the next section are correct, we have performed several checks and comparisons. The slightly modified VBFNLO matrix elements used in the POWHEG-BOX implementation have been checked phase-space pointwisely against the original VBFNLO ones. Very good agreement between 11 to 15 digits has been found. Hence also the evaluation of the couplings, which is slightly different than in VBFNLO, could be validated. The subtraction of IR singularities in the POWHEG-BOX is done in the FKS framework with automatically generated local subtraction terms. We have checked that the ratio of the real contributions and the subtraction terms approaches one in all singular regions associated with one specific parton. Therefore the IR divergences cancel which additionally ensures that all flavor structures of the Born and real-emission contributions are taken into account.

Another strong test is the comparison of LO and NLO cross sections and differential distributions with other programs. The distributions involving final-state particles agree between the POWHEG-BOX and VBFNLO implementations within statistical errors of at most 1%. In order to validate the three different phase-space operation modi, we have compared cross sections and distributions at fixed order and after event generation using all three different options.

As mentioned before, there exists another implementation of electroweak Zjj production within the POWHEG-BOX [115]. We have compared our implementation with the other one using generation cuts in the phase space generator. The matrix elements agree phase-space point by phase-space point at the level of at least 10 relevant digits. Additionally, cross sections and differential distributions at NLO and after event generation have been compared and good agreement within statistical uncertainties has been found.

4.3. Numerical Results

In this section we present numerical results obtained with the POWHEG-BOX for W and Z production via VBF. Special attention is given to the influence of different parton showers on the distribution of the third-hardest jet.

The cross sections and distributions shown below are calculated for the LHC running at a center-of-mass energy of 8 TeV. We use the `CT10` PDF set [124] with $\alpha_s(M_Z) = 0.11798$, as implemented in the LHAPDF package [125]. The electroweak couplings are calculated using

tree-level relations with the input parameters $M_W = 80.398$ GeV, $M_Z = 91.1876$ GeV and the Fermi constant $G_F = 1.16637 \cdot 10^{-5}$ GeV^{-2}. The obtained values for the total width of the electroweak gauge bosons are $\Gamma_Z = 2.5084$ GeV and $\Gamma_W = 2.0977$ GeV. The resulting QED fine structure constant is $\alpha_{\text{QED}} = 1/132.341$ and the weak mixing angle is $\sin^2\theta_W = 0.2226$. Recombination of partons into jets is done according to the anti-k_T algorithm [126] provided by the FastJet-package [127, 128] with default distance parameter $R = 0.5$. The factorization and renormalization scale are set to the mass of the produced vector boson, $\mu_F = \mu_R = M_V$.

All jets originating from the NLO calculation or the parton shower are demanded to have a minimum transverse momentum of

$$p_{T,j} > 20 \text{ GeV}, \tag{4.7}$$

as well as a rapidity bounded by

$$|y_j| < 4.5 \tag{4.8}$$

to be well observable by the experiments. Additionally, we require the two highest-p_T jets, called tagging jets, to satisfy

$$p_{T,j}^{\text{tag}} > 30 \text{ GeV}. \tag{4.9}$$

We require the leptons to lie in the central region of the detector and have a non-vanishing transverse momentum,

$$|y_l| < 2.5 \qquad \text{and} \qquad p_{T,l} > 20 \text{ GeV}. \tag{4.10}$$

Since electroweak Zjj production includes contributions from $\gamma^* jj \to l^+ l^- jj$ one is forced to impose a cut on the invariant mass of the lepton pair to avoid singularities,

$$m_{ll} > 20 \text{ GeV}. \tag{4.11}$$

All leptons should be separated from each other and from the jets,

$$\Delta R_{ll} > 0.1 \qquad \text{and} \qquad \Delta R_{jl} > 0.4, \tag{4.12}$$

where the lego-plot separation is given by $\Delta R_{ij} = \sqrt{(y_i - y_j)^2 + (\phi_i - \phi_j)^2}$, with ϕ_i denoting the azimuthal angle of particle i.

As already mentioned before, the VBF detector signature with one very forward and one very backward jet and little hadronic activity in the rapidity gap between the two tagging jets can be used for QCD background suppression. An additional feature of Vjj production in VBF is, that the decay products of the weak boson tend to be located in the rapidity gap. We therefore demand the typical VBF cuts,

$$m_{jj}^{\text{tag}} < 600 \text{ GeV}, \quad \Delta y_{jj}^{\text{tag}} > 4, \quad y_{j1}^{\text{tag}} \times y_{j2}^{\text{tag}} < 0, \quad y_{j,tag}^{min} + 0.2 < y_l < y_{j,tag}^{max} - 0.2. \tag{4.13}$$

As has already been explained in Section 3.3, the events generated by the Powheg-Box can be interfaced with any p_T-ordered shower like Pythia or the Dipole Shower

	W^+jj	W^-jj	Zjj
VBFNLO	(254.0 ± 0.1) fb	(134.6 ± 0.1) fb	(24.48 ± 0.02) fb
POWHEG@NLO	(253.9 ± 0.3) fb	(134.4 ± 0.2) fb	(24.47 ± 0.07) fb
POWHEG+PYTHIA	(251.0 ± 0.8) fb	(131.7 ± 0.5) fb	(24.48 ± 0.18) fb
POWHEG+HERWIG++	(249.8 ± 0.8) fb	(131.2 ± 0.5) fb	(24.08 ± 0.18) fb
POWHEG+DS++	(245.2 ± 0.8) fb	(128.0 ± 0.5) fb	(23.56 ± 0.18) fb

Table 4.1.: Cross sections for electroweak Vjj production with subsequent decay of the vector boson into the first lepton family including VBF-cuts (Equations (4.7)–(4.13)). The NLO cross section has been obtained with the new POWHEG-BOX implementation and matches the VBFNLO prediction. PYTHIA, HERWIG++ and DS++ results include parton shower effects, but neither hadronisation nor effects from underlying event simulations.

DS++ implemented in HERWIG++. Using angular-ordered showers, like the standard HERWIG++ shower, radiation harder than the real emission from the matrix element has to be eliminated. This is possible using Les Houches event [33, 34] files as input. However, additional wide-angle, soft radiation is missing and has to be added back in after the usual shower as explained in detail in Ref. [21, 22]. Unfortunately, this feature called truncation is not present in the used HERWIG++ release. Nevertheless, the effect of this additional soft radiation can be estimated from the comparison of HERWIG++ with the p_T-ordered DS++.

In the analysis presented below we are mostly interested in parton shower effects. Therefore we do not take into account hadronization or underlying-event simulations. We use PYTHIA version 6.4.25 with the Perugia 0-tune (Feb 2009) and HERWIG++ version 2.6.1a for the standard shower and for DS++. The cross sections for all three processes at fixed order and after showering using the VBF cuts defined in Equations (4.7)–(4.13) are listed in Table 4.1.

Figure 4.4 shows distributions of the leading jets and leptons in electroweak Vjj production. The top panel depicts the rapidity of the second tagging jet and the transverse momentum of the positron in electroweak W^+jj production. The lower panel displays the transverse momentum distribution of the hardest jet in W^-jj production and the invariant mass of the two tagging jets for Z production via VBF. In all four plots, the new POWHEG-BOX results interfaced with PYTHIA, HERWIG++ and DS++ as well as NLO predictions obtained with VBFNLO are shown. The ratio plot always compares the three shower predictions with the fixed-order result obtained with VBFNLO. The normalization of the curves varies for the different attached showers due to the different cross sections after including additional radiation and applying cuts. This discrepancy is caused by events which slightly migrate by parton shower effects to phase-space regions that do not obey the required cuts. However, as expected, this difference is the only one between the shower and NLO predictions. The shape of the various curves stays unaltered. In summary, observables constructed from the two tagging jets or the charged leptons and neutrinos are hardly affected by additional parton shower radiation. The VBF signature

of the events is therefore preserved.

On the other hand, parton shower effects become more pronounced in the distributions of the third-hardest jet, where the corresponding matrix elements are only LO accurate. The top left panel of Figure 4.5 displays the transverse momentum distribution of the first non-tagging jet for electroweak W^+jj production. The cut on the transverse momentum has been lowered to $p_{T,j_3} > 1$ GeV to show the damping of the soft divergence due to the Sudakov factor, which is almost the same for Pythia, Herwig++ and DS++. For a moderate jet p_T between 20 and 50 GeV, Herwig++ predicts more jets than Pythia but matches the NLO prediction, whereas Pythia and DS++ are in good agreement. The tail of the distribution with $p_T \gtrsim 75$ GeV shows lower rates for all three showers than the NLO calculation, since additional hard and/or wide-angle radiation from the parton showers leads to partons which are not re-clustered into the third-hardest jet and may potentially lead to additional sub-leading jets.

The other three plots of Figure 4.5 show the location of the third-hardest jet relative to the tagging jets,

$$y_3^* = y_{j_3} - \frac{y_{j_1} + y_{j_2}}{2}, \tag{4.14}$$

for all three processes studied here with the usual VBF cuts of Equations (4.7)–(4.13). On average, the two tagging jets are located at $\langle |y_{j_1} - y_{j_2}| \rangle / 2 \approx 2.6$. Accordingly, $|y_3^*| \lesssim 2.6$ typically corresponds to the rapidity gap between the tagging jets and $|y_3^*| \gtrsim 2.6$ to the third jet being positioned between the tagging jets and the beam axis. For all three processes under consideration Pythia tends to radiate additional partons into the rapidity gap which then get re-clustered into the third-hardest jet. In addition, the region between the tagging jets and the beam axis is less populated with hard jets than predicted at NLO. Herwig++ and DS++ give the same prediction but are contrary to Pythia: in the rapidity gap, the rates are lower than predicted by the NLO calculation, whereas more jets between the tagging jets and the beam axis are observed.

Since the QCD part of electroweak gauge-boson production and Higgs boson production via VBF is essentially the same, we can qualitatively compare the shower effects on the distribution of the third-hardest jet. As has been shown in Section 3.2, Figure 3.4, the two Herwig++ showers and Pythia give nearly contradictory predictions for the rapidity distribution of the third-hardest jet in Higgs boson production via VBF, when considering only the parton shower corrections to the LO process. Taking into account the matrix elements for the real radiation in Vjj production via VBF, the discrepancy between the three parton showers are partly resolved. The damping in the low p_{T,j_3} region is dictated by the Powheg Sudakov factor and only additional radiation modeled by the respective parton shower coming from the two tagging jets or off the third-hardest parton can modify the y_3^* distribution, since the real-emission matrix elements are correctly taken into account.

The origin of the remaining differences between the three parton shower predictions for the distribution of the third-hardest jet can be studied by varying different parameters. This will be illustrated using the example of W^+ production via VBF. However, the main findings are the same for electroweak W^-jj and Zjj production. The left panel

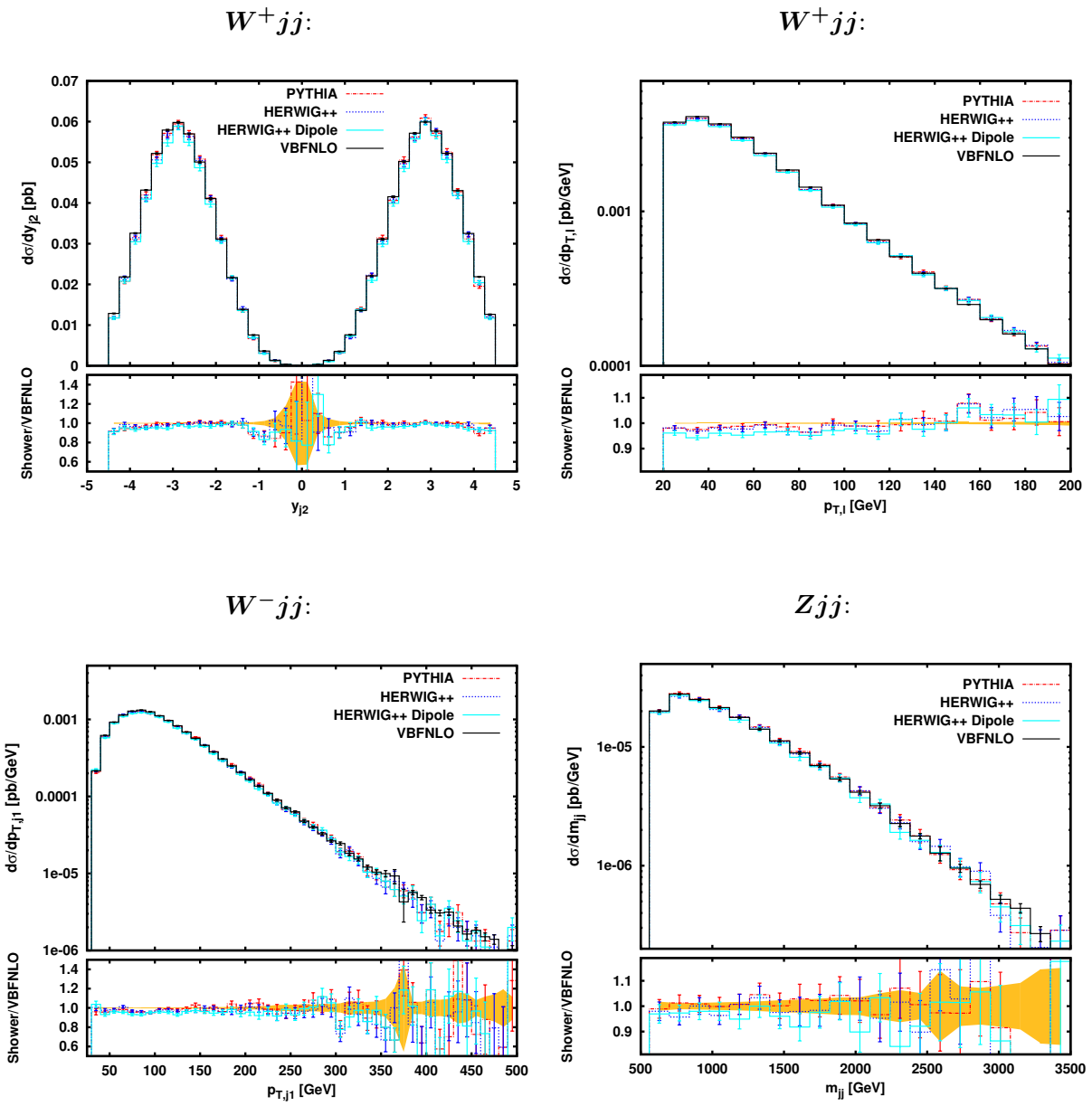

Figure 4.4.: Distributions of the leading jets and leptons in electroweak Vjj production. Top panel: Differential cross-section of the rapidity of the second hardest tagging jet (left) and the transverse momentum of the charged lepton (right) of the POWHEG prediction, compared to the fixed-order curves of VBFNLO (black solid line) for W^+jj production via VBF. The (red) dashed-dotted line shows the prediction of the POWHEG result showered with PYTHIA, the (blue) dotted line corresponds to the angular-ordered HERWIG++ shower and the (turquoise) solid line to DS++. The error bars show the statistical error of the integration, the yellow error band in the ratio plot gives the statistical error on the fixed-order NLO result of VBFNLO.
Lower panel: Transverse-momentum distribution of the hardest jet in W^- production via VBF (left) and the invariant tagging-jet mass for Zjj production (right). Colors and line styles are given above.

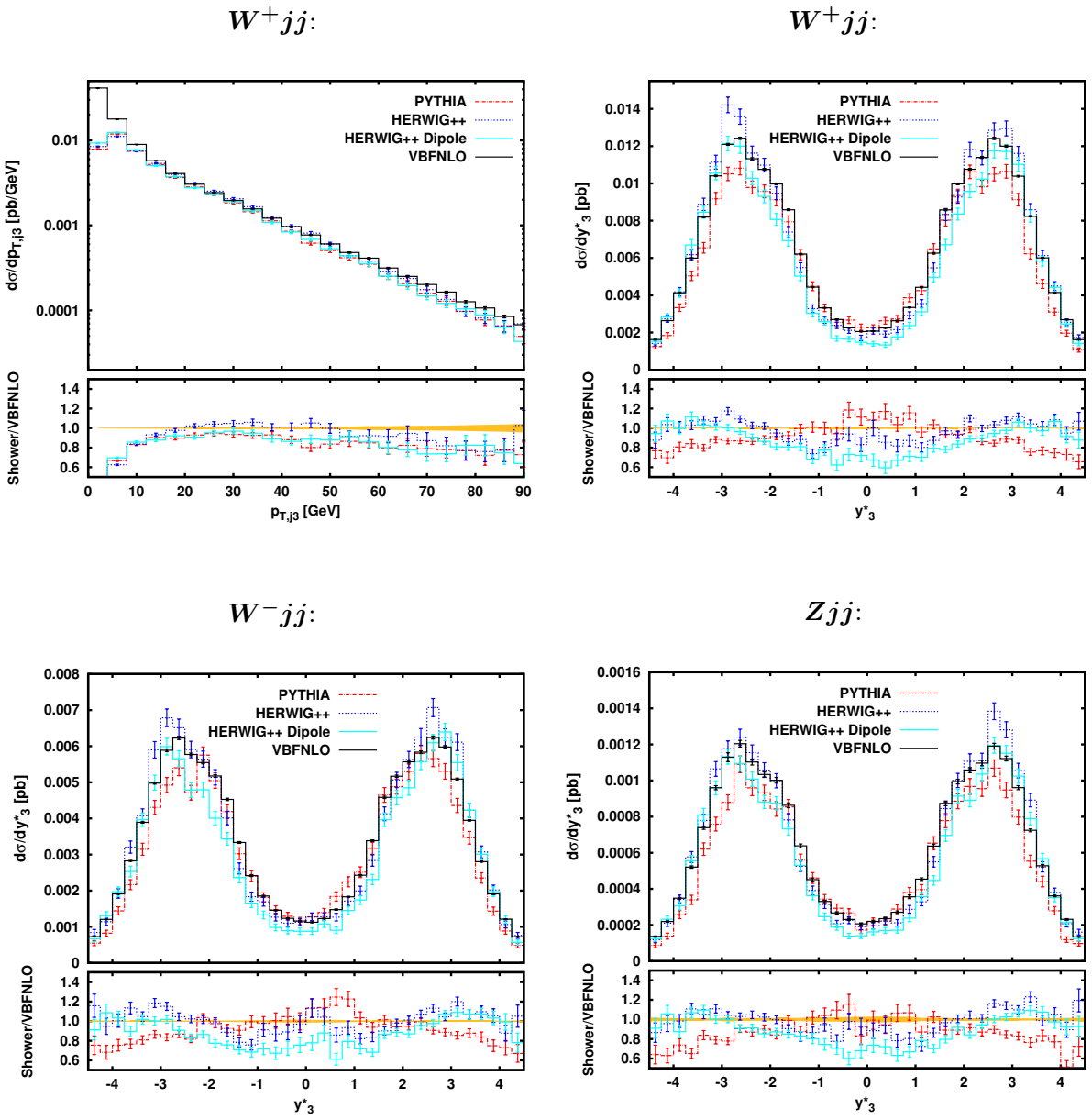

Figure 4.5.: Top panel: Differential distribution of the transverse momentum of the third jet with $p_{T,j_3} > 1$ GeV (left) and the variable y_3^* defined in Equation (4.14) (right) including all cuts, comparing the predictions of the three parton showers to the fixed-order distributions of VBFNLO for electroweak W^+jj production.
Lower panel: y_3^* distribution for W^-jj (left) and Zjj production via VBF (right).
The line styles are assigned as in Figure 4.4.

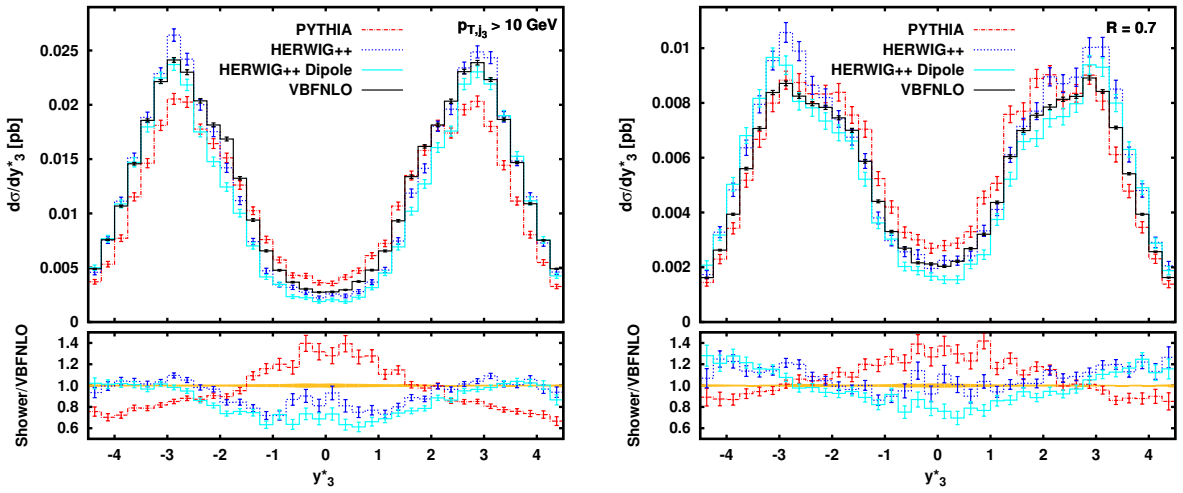

Figure 4.6.: Differential y_3^* distribution for electroweak W^+jj production as defined in Equation (4.14). Left: The standard cut on the transverse momentum has been lowered to $p_{T,j_3} > 10$ GeV. Right: The distance parameter of the jet algorithm has been increased to $R = 0.7$. The line styles are assigned as in Figure 4.4.

of Figure 4.6 shows the y_3^* distribution for a lowered cut on the transverse momentum of the third jet, $p_{T,j_3} > 10$ GeV. Therefore more soft partons lead to visible jets. Obviously, the distinction between PYTHIA and the two HERWIG predictions gets more pronounced. This difference is due to the fact that PYTHIA tends to emit more soft partons, whereas HERWIG++ and DS++ preferentially emit partons in the collinear region between the beam axis and the tagging jets. This conclusion is supported by the observation that the y_3^* distribution is fairly unaffected by the variation of the p_{T,j_3} cut for the two HERWIG++ siblings. Compared to the NLO distribution, the ratio of the curves remains unaltered. This can be best seen in the lower panel of the respective plots. The collinear region between the tagging jets and the beam axis is well described, whereas the jet rates in the central region are lower than for the fixed-order result. In contrast, PYTHIA predicts more jets in the rapidity gap than for a higher cut on the transverse momentum.

To test whether this conclusion is correct, we study the distribution of y_3^* for larger values of R (Figure 4.6, right). There, the distance parameter R of the anti-k_T algorithm is increased to $R = 0.7$ compared to $R = 0.5$, which has been used before. The cut on the transverse momentum of the third-hardest jet is reset to the standard value, $p_{T,j} > 20$ GeV. A first comparison between this plot and the top right panel of Figure 4.5 shows that the overall rate increases for all three showers compared to the respective NLO prediction. This increase is due to the fact that more soft and/or collinear partons are clustered into the third-hardest jet, which increases the possibility that the jet is accepted. Again, the jet activity in the central region is increased for PYTHIA due to uncorrelated, soft radiation. In contrast, HERWIG++ and DS++ produce collinear radiation between the tagging jets and the beam remnant, which leads to jets with high $|y_3^*|$. Therefore, only the increment of R and not the $p_{T,j}$ cut affects the shape of y_3^* for the two HERWIG++

siblings.

It is also worthwhile noticing that HERWIG++ and DS++ predict the same behavior for the y_3^* distribution. This implies that additional wide-angle soft radiation, which is included in DS++, plays a minor role in this process and truncated shower effects can be omitted. The difference between HERWIG++ and DS++ on the one side, and PYTHIA on the other side in fact seems to depend on how the available phase space is filled with additional soft and collinear radiation.

To corroborate the argument on the difference between PYTHIA and the two HERWIG++ showers we investigate the differential jet shape [129] $\rho(r)$ of the third-hardest jet,

$$\rho(r) = \frac{1}{\Delta r} \sum_{\text{parton} \in j_3} \frac{p_{T,\text{parton}}(r - \Delta r/2, r + \Delta r/2)}{p_{T,j_3}}, \tag{4.15}$$

which is a measure for the jet energy flow. The $\rho(r)$ definition of Equation (4.15) is based on Equation (4) from Ref. [130] and has been slightly modified to solely take the third-hardest jet into account. The distance r between the third-hardest jet and the partons contributing to it in the rapidity-azimuthal angle plane,

$$r = \sqrt{(\phi_{j_3} - \phi_{\text{parton}})^2 + (y_{j_3} - y_{\text{parton}})^2}, \tag{4.16}$$

ranges from $\frac{\Delta r}{2}$ to $R - \frac{\Delta r}{2}$, where Δr is a free parameter. The $p_{T,\text{parton}}(r_1, r_2)$ designates the transverse momentum of partons in an annulus between radii r_1 and r_2, i.e. $r_1 \leq r < r_2$. The sum includes all partons which are recombined into the third-hardest jet. For the plots shown below we use $\Delta r = 0.1$. The differential jet shape $\rho(r)$ is normalized,

$$\int_0^R \rho(r) \mathrm{d}r = 1. \tag{4.17}$$

For the argument given below the position of the third-hardest jet with respect to the tagging jets is crucial. To divide the phase space into the rapidity gap and the region between the tagging jets and the beam axis we use the variable

$$z_3^* = \frac{y_3^*}{|y_{j_1} - y_{j_2}|}. \tag{4.18}$$

The two tagging jets are localized at $|z_3^*| = 0.5$, thus $|z_3^*| < 0.5$ corresponds to the rapidity gap and $|z_3^*| > 0.5$ to the region between the tagging jets and the beam axis.

Figure 4.7 shows the differential jet shape $\rho(r)$ averaged over all contributing jets for the three hardest jets in the top panel. In addition, $\rho(r)$ is displayed for the third-hardest jet in different areas of the phase space in the lower panel, all with a distance parameter $R = 0.7$. The differential jet shape for the two hardest jets shows almost no dependence on the shower in use, whereas the first sub-leading jet is evidently sensitive to shower corrections. This effect will now be examined in more detail. The upper right panel shows $\rho(r)$ for the whole available phase space. The jets obtained with PYTHIA are moderately broader than with HERWIG++ and DS++. More partons with $r > 0.1$ are combined

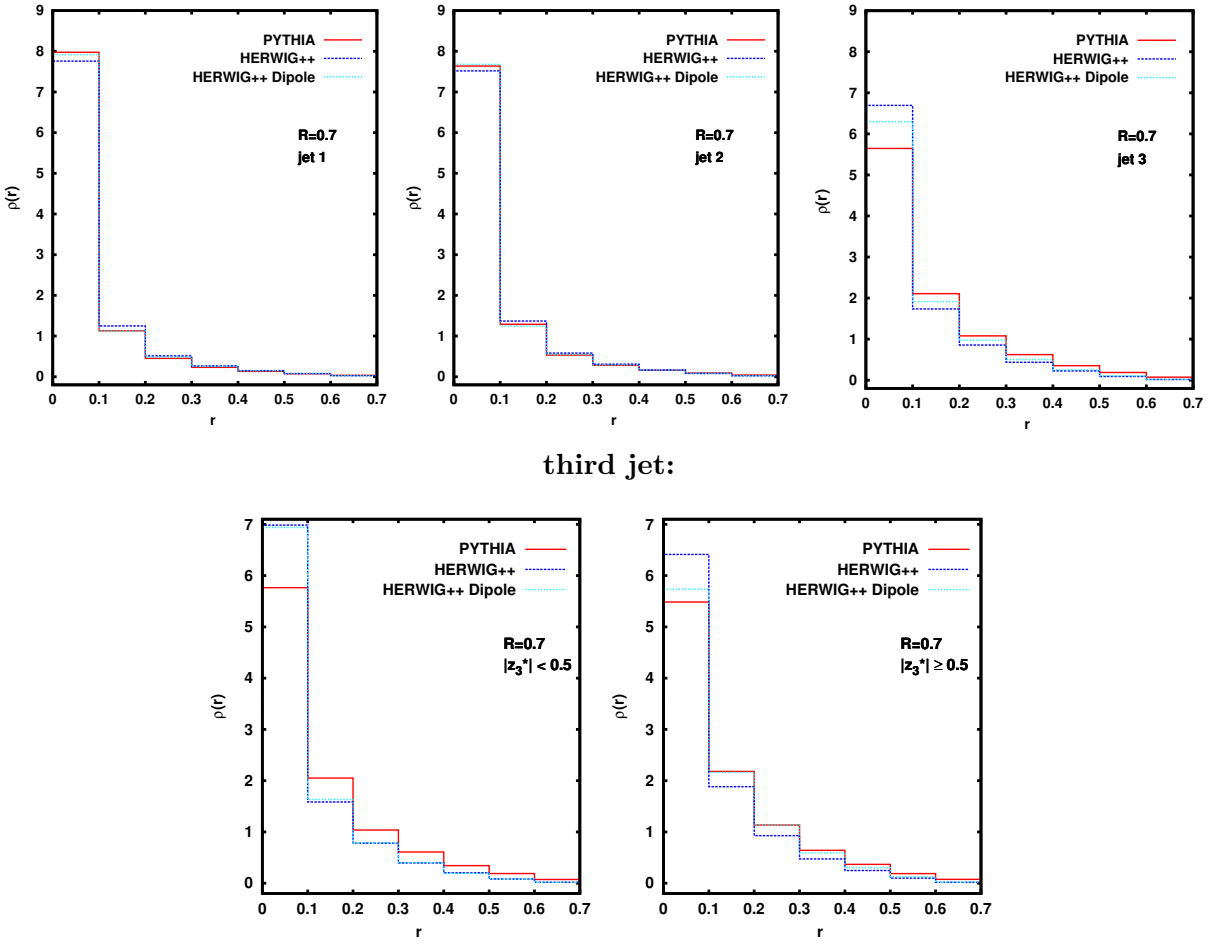

Figure 4.7.: Top panel: Differential jet shape $\rho(r)$ defined in Equation (4.15) for $R = 0.7$ and $\Delta r = 0.1$ for the three hardest jets.
Lower panel: $\rho(r)$ for the third-hardest jet divided into different regions of the phase space. The line styles are assigned as in Figure 4.4.

into the third-hardest jet than for the other two showers. In the lower left panel the differential jet shape for the third-hardest jet ending up in the rapidity gap between the two tagging jets is shown. The lower right panel displays the collinear region between the tagging jets and the beam axis. A striking observation is, that the difference between Herwig++ and Pythia in large part emerges from jets in the central region. This matches the observation described above and is also correlated with the population of the available phase space with additional radiation. Soft, wide-angle emissions are fairly uncorrelated to the radiating parton, which can broaden the jet. On the other hand, collinear radiation is emitted in the vicinity of the mother parton and therefore leads to narrow jets. For Pythia, the jets are essentially broader in the rapidity gap, whereas $\rho(r)$ is almost the same for Pythia and DS++ in the collinear region. This region can almost be seen as an inclusive jet sample, which is adequately well described by all three parton showers, see e.g. Ref. [130]. Compared to Herwig++, DS++ predicts slightly

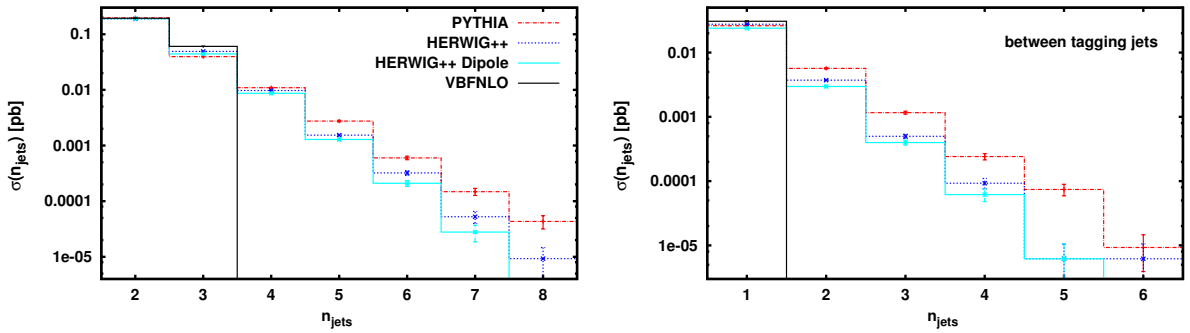

Figure 4.8.: Jet multiplicity with the standard cuts of Equations (4.7)–(4.13) for jets in the whole allowed phase space (left) and in the rapidity gap between the tagging jets (right). The line styles are assigned as in Figure 4.4.

broader jets for $|z_3^*| > 0.5$. This difference can be traced back to the relatively low IR cut-off on the Sudakov factor in DS++, which leads to soft radiation at the end of the showering stage. When increasing this cut-off, the differential jet shape and the rate of the third jet of the two showers come close to each other.

Now we can explain why the PYTHIA prediction lies below the HERWIG++ one for the transverse momentum of the third-hardest jet, see Figure 4.5. Since PYTHIA jets are broader due to wide-angle radiation, some partons which do not get re-clustered into the jet take away parts of the p_T of the original parton. In HERWIG++, on the contrary, narrow-angle radiation off the third-hardest parton as well as additional radiation from the two tagging jets end up in the third-hardest jet. This can be seen in the p_{T,j_3} distribution for large distance parameters $R \geq 0.5$, where the rate exceeds the NLO prediction. Radiation off the two tagging jets can also be observed for PYTHIA, but the distance parameter R has to be increased even more. When normalizing to the total cross section, the HERWIG++ and DS++ predictions are in good agreement. The soft radiation in DS++ due to the mentioned low IR cut-off of the Sudakov factor can lead to a lower rate of the third-hardest jet once a minimum p_T and a maximum rapidity threshold on the tagging jets are set.

As explained in the introduction to this chapter, it is important to know the distributions of the third-hardest and the other subsequent jets in the rapidity gap to estimate the error on a CJV. The multiplicity of jets is quite different for the three showers (Figure 4.8). In the left panel, the jet multiplicity for the jets in the whole allowed phase space is shown. The first three jets are given by the hard matrix elements and are reasonably well described by PYTHIA, HERWIG++ and DS++, but with cut-dependent differences for the distributions of the third-hardest jet. Additional jets solely originate from the parton showers and therefore depend on how the available phase space is filled with soft and collinear partons. Since PYTHIA radiates more uncorrelated, softer partons, they can build a sub-leading jet on their own, whereas the narrow-angle radiation in HERWIG++ and DS++ implies fewer jets surviving the jet criteria defined in Equations (4.7)–(4.8), (4.12). This effect is even more pronounced in the rapidity gap, as shown in the right panel of Figure 4.8. We again stress that HERWIG++ as a vetoed angular-ordered shower shows the same behavior as its p_T-ordered sibling DS++. Therefore, at least for the processes studied

here, the effect of truncation can be neglected.

4.4. Conclusions

W and Z production via VBF are important processes at the LHC, since they provide the possibility to study the VBF topology and CJV techniques before moving on to the important and more complex Higgs production process. Since distributions are sensitive both to NLO and shower corrections, we have implemented Wjj and Zjj production via VBF in the POWHEG-BOX to interface the NLO calculation with different parton showers. One important result of this analysis is that the distributions of the tagging jets and the leptonic W and Z decay products are largely unaffected by additional radiation simulated with PYTHIA, HERWIG++ and DS++. The shape of these distributions remains unaffected, whereas the overall normalization changes slightly. This change arises from the migration of some events to phase-space regions not incorporated within the cuts due to additional radiation off the NLO partons.

On the contrary, the third-hardest jet, whose matrix elements only enter the calculation at LO, is sensitive to the details of the parton shower in use. The effect is cut dependent, but can easily be of the order of $30 - 40\%$ in distributions, see e.g. Figure 4.6. However, the distinction between the three parton showers is considerably smaller than for Higgs boson production via VBF at LO, see Figure 3.4.

In principle, HERWIG++ as a vetoed shower cannot be used in combination with the POWHEG-BOX, since wide-angle soft radiation from truncation is missing. However, we expect the effect of this additional radiation to be small, since HERWIG++ is in good agreement with the p_T-ordered DS++. Nevertheless, sizable differences between PYTHIA and HERWIG++ are present in the distributions of the non-tagging jets. The differences of the showers can be traced back to the population of the available phase space with additional radiation. PYTHIA seems to favor rather soft partons, which are likely to end up in the rapidity gap between the two tagging jets. The two HERWIG++ showers essentially leave the rapidity gap unaltered, but preferentially radiate collinear partons between the tagging jets and the beam axis. The soft, wide-angle radiation leads to a relatively broad (third-hardest) jet for PYTHIA in the rapidity gap, whereas the small-angle radiation in HERWIG++ and DS++ results in narrow jets. Additionally, a lower jet multiplicity is observed for the latter programs.

These differences between the three shower predictions reflect remaining uncertainties of available NLO predictions. They are mostly present in the distributions of the third-hardest jet, since it is only LO accurate, and have to be taken into account when comparing the predictions to data.

The code which has been used to obtained these results can be found on the POWHEG-BOX homepage [105].

CHAPTER 5

HIGGS BOSON PRODUCTION VIA VECTOR-BOSON FUSION WITH ANOMALOUS COUPLINGS

In this and the following Chapters we will focus on Higgs boson production in vector-boson fusion (VBF). We start our discussion by looking at the SM and possible deviations in the context of anomalous couplings.

5.1. Introduction

After the discovery of a new boson at the LHC [19, 20], the most important task is to determine its properties, namely the couplings to SM particles, its spin and CP quantum numbers. Tremendous joint theoretical and experimental efforts [56–58] have been made on the way to the discovery of the resonance and they are now focused on pinning down these quantum numbers. Although the measurements seem to favor a SM Higgs boson, other beyond the SM (BSM) possibilities, like a spin-2 or a spin-0 CP-even particle with an admixture of CP-odd couplings, cannot be excluded yet [72–84].

Most of the studies aiming to measure the spin and CP properties of the newly found boson involve differential distributions of the final state particles, which, as we have already seen in the last chapter, can be sensitive to both NLO and shower corrections. In VBF the Higgs boson is produced via quark-scattering mediated by weak gauge boson exchange in the t-channel, $qq' \to qq'H$. The NLO QCD corrections to the SM process have been known for quite some time [62–64] and even NNLO QCD, NLO electroweak and mixed QCD and EW contributions have been calculated [65–70, 131, 132]. To account for parton shower effects, this process has also been matched to parton showers in the POWHEG [21, 22] and MC@NLO [86] framework [120, 133–135].

One striking feature of VBF processes is that a modified coupling structure of the produced scalar particle to the vector-bosons fusing in the t-channel is translated to the distributions of the tagging jets. This property can be used to determine the CP quantum numbers

of the Higgs boson and to set limits on anomalous couplings of the Higgs boson to electroweak bosons [136–139]. The deviations of these couplings from their respective SM values can be parametrized in terms of an effective Lagrangian [140]. For this effective Lagrangian approach the NLO QCD corrections to the VBF process are known [141, 142] and the matching to parton showers with MadGraph5_aMc@Nlo has recently been published [143]. In the present work we use the Powheg method and its implementation in the Powheg-Box framework [23] to combine the NLO QCD calculation with parton showers. Some parts of the program are adopted from the already existing SM code [120], the matrix elements needed for anomalous couplings are taken from Vbfnlo [24–26].

This chapter is organized as follows: In Section 5.2 we introduce possible deviations of the Higgs couplings using an effective Lagrangian approach. Section 5.3 reviews the implementation of the beforehand explained anomalous couplings in the Powheg-Box. In Section 5.4 we derive couplings for a singlet scalar boson reproducing the SM event rates, which can act as Higgs imposter [144–148]. In Section 5.5 we present differential distributions resulting from the introduced scenarios described in Section 5.4. In Section 5.6 we will conclude.

5.2. Effective Lagrangian Approach

Deviations of the SM Higgs couplings to electroweak gauge bosons can be parametrized in an effective Lagrangian density, consisting of the SM Lagrangian supplemented by higher-dimensional operators [140],

$$\mathcal{L}_{\text{eff}} = \mathcal{L}_{\text{SM}} + \sum_i \frac{f_i^{(5)}}{\Lambda} \mathcal{O}_i^{(5)} + \sum_i \frac{f_i^{(6)}}{\Lambda^2} \mathcal{O}_i^{(6)}. \tag{5.1}$$

Here, Λ denotes the scale where new physics enters, f_i are the dimensionless coupling constants for the corresponding operators $\mathcal{O}_i^{(k)}$, with k indicating the mass dimension. In the following we refer to any spin-0 state with couplings described by the effective Lagrangian or by the SM Lagrangian as Higgs boson H.

Starting from an $SU(2)_L$ doublet field ϕ, only operators with dimension 6 (or larger) contribute to the effective Lagrangian defined in Equation (5.1), since an even number of covariant derivatives and an even number of doublet fields have to be combined to built a Lorentz and isospin scalar. When imposing gauge and Lorentz invariance one is left with 11 CP-even operators [149–153] containing the scalar field ϕ, the covariant derivative D_μ and the field strength tensors $W_{\mu\nu}$ and $B_{\mu\nu}$. Three of them contain only gauge fields and the covariant derivatives, two operators solely modify the Higgs self couplings. Therefore, only six CP-even (and three CP-odd) operators contribute to the HVV vertex ($V = W^\pm, Z, \gamma$). In the following we will disregard two of the CP-even operators: One contributes only to the Z mass and is heavily restricted by the measured ρ-parameter [154], the other has large contributions to the S-parameter [155, 156, 149], which constrains BSM contributions to the Z-boson self energy.

Overall, we are left with the following effective Lagrangian [142, 157],

$$\begin{aligned}\mathcal{L}_{\text{eff}} &= \frac{f_W}{\Lambda_6^2}\mathcal{O}_W + \frac{f_B}{\Lambda_6^2}\mathcal{O}_B + \frac{f_{WW}}{\Lambda_6^2}\mathcal{O}_{WW} + \frac{f_{BB}}{\Lambda_6^2}\mathcal{O}_{BB} \\ &+ \frac{f_{\widetilde{W}W}}{\Lambda_6^2}\mathcal{O}_{\widetilde{W}W} + \frac{f_{\widetilde{B}B}}{\Lambda_6^2}\mathcal{O}_{\widetilde{B}B} + \frac{f_{\widetilde{B}}}{\Lambda_6^2}\mathcal{O}_{\widetilde{B}}. \end{aligned} \tag{5.2}$$

The operators are given by

$$\begin{aligned} \mathcal{O}_{BB} &= \phi^\dagger \widehat{B}_{\mu\nu}\widehat{B}^{\mu\nu}\phi, & \mathcal{O}_{\widetilde{B}B} &= \phi^\dagger \widehat{\widetilde{B}}_{\mu\nu}\widehat{B}^{\mu\nu}\phi, \\ \mathcal{O}_{WW} &= \phi^\dagger \widehat{W}_{\mu\nu}\widehat{W}^{\mu\nu}\phi, & \mathcal{O}_{\widetilde{W}W} &= \phi^\dagger \widehat{\widetilde{W}}_{\mu\nu}\widehat{W}^{\mu\nu}\phi, \\ \mathcal{O}_{B} &= (D_\mu\phi^\dagger)\widehat{B}^{\mu\nu}(D_\nu\phi), & \mathcal{O}_{\widetilde{B}} &= (D_\mu\phi^\dagger)\widehat{\widetilde{B}}^{\mu\nu}(D_\nu\phi), \\ \mathcal{O}_{W} &= (D_\mu\phi^\dagger)\widehat{W}^{\mu\nu}(D_\nu\phi), \end{aligned} \tag{5.3}$$

with

$$\widehat{W}_{\mu\nu} = ig_2 T^a W^a_{\mu\nu}, \qquad \widehat{B}_{\mu\nu} = ig_1 \frac{Y}{2} B_{\mu\nu}. \tag{5.4}$$

The $SU(2)_L$ and $U(1)_Y$ generators are denoted by T^a and Y, respectively, g_2 and g_1 are the SM $SU(2)_L$ and $U(1)_Y$ gauge couplings and $\widetilde{V}_{\mu\nu}$ denotes the dual field strength tensor.

Another possible parametrization of the effective Lagrangian for dimension-6 operators is given in the mass eigenstate basis of the gauge bosons and the physical Higgs boson [158–160] and has been used by the L3 Collaboration [161]. The coupling parameters in this parametrization, d, d_B, Δg_1^Z and $\Delta\kappa_\gamma$ and the respective CP-odd coupling constants, are related to the coefficients f_i/Λ_6^2 of the effective Lagrangian defined in Equation (5.2) according to [24–26, 142]

$$\begin{aligned} d &= -\frac{M_W^2}{\Lambda_6^2}\, f_{WW}\,, & \widetilde{d} &= -\frac{M_W^2}{\Lambda_6^2}\, f_{\widetilde{W}W}\,, \\ d_B &= -\frac{M_W^2}{\Lambda_6^2}\,\frac{\sin^2\theta_w}{\cos^2\theta_w}\, f_{BB}\,, & \widetilde{d}_B &= -\frac{M_W^2}{\Lambda_6^2}\,\frac{\sin^2\theta_w}{\cos^2\theta_w}\, f_{\widetilde{B}B}\,, \\ \Delta\kappa_\gamma = \kappa_\gamma - 1 &= \frac{M_W^2}{2\Lambda_6^2}\,(f_B + f_W)\,, & \widetilde{\kappa}_\gamma &= \frac{M_W^2}{2\Lambda_6^2}\, f_{\widetilde{B}}\,, \\ \Delta g_1^Z = g_1^Z - 1 &= \frac{M_Z^2}{\Lambda_6^2}\,\frac{f_W}{2}\,. \end{aligned} \tag{5.5}$$

For a scalar particle H_S, disregarding $SU(2)_L$ relations, another parametrization for anomalous couplings to electroweak gauge bosons is required, using an effective Lagrangian involving dimension-5 operators [141],

$$\begin{aligned}\mathcal{L}_{\text{eff}} &= \frac{g_{5e}^{HZZ}}{2\Lambda_5} H_S Z_{\mu\nu}Z^{\mu\nu} + \frac{g_{5o}^{HZZ}}{2\Lambda_5} H_S \widetilde{Z}_{\mu\nu}Z^{\mu\nu} + \frac{g_{5e}^{HWW}}{\Lambda_5} H_S W^+_{\mu\nu}W^{-\mu\nu} + \frac{g_{5o}^{HWW}}{\Lambda_5} H_S \widetilde{W}^+_{\mu\nu}W^{-\mu\nu} + \\ &\frac{g_{5e}^{HZ\gamma}}{\Lambda_5} H_S Z_{\mu\nu}A^{\mu\nu} + \frac{g_{5o}^{HZ\gamma}}{\Lambda_5} H_S \widetilde{Z}_{\mu\nu}A^{\mu\nu} + \frac{g_{5e}^{H\gamma\gamma}}{2\Lambda_5} H_S A_{\mu\nu}A^{\mu\nu} + \frac{g_{5o}^{H\gamma\gamma}}{2\Lambda_5} H_S \widetilde{A}_{\mu\nu}A^{\mu\nu}. \end{aligned} \tag{5.6}$$

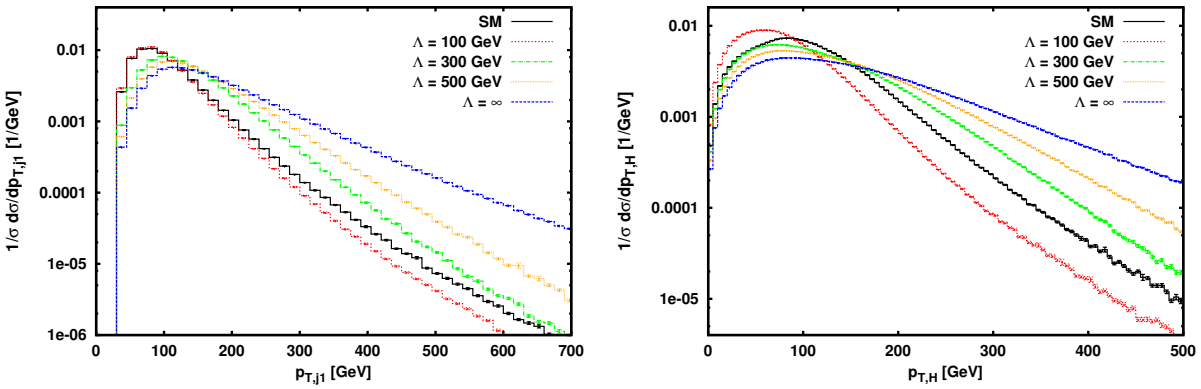

Figure 5.1.: Form-factor dependence of transverse momentum distributions of the hardest jet (left) and the scalar particle (right) for H production in VBF for $\sqrt{s} = 8$ TeV at the LHC. The colored lines correspond to different scales for F_1 as defined in Equation (5.7), $\Lambda = \infty$ means no form factor is applied. The curves are at LO and have been obtained with VBFNLO [24–26].

The CP-even or CP-odd nature of the operators is labeled by the subscript e or o. As for the L3 parametrization in Equation (5.5), the gauge fields have been transformed into the mass eigenstate basis.

In order to model effective, momentum-dependent HVV couplings we use two different form factors as described in Refs. [141, 142],

$$F_1 = \frac{\Lambda^2}{q_1^2 - \Lambda^2} \frac{\Lambda^2}{q_2^2 - \Lambda^2}, \tag{5.7}$$

$$F_2 = -2\,\Lambda^2\, C_0\Big(q_1^2, q_2^2, (q_1+q_2)^2, \Lambda^2\Big), \tag{5.8}$$

which are multiplied to each vertex containing anomalous couplings. Here, q_1 and q_2 denote the momenta of the vector bosons in the t-channel and C_0 is the scalar one-loop three-point function in the notation of Ref. [162]. They mimic new physics entering at a scale Λ at the loop level and thereby can be chosen to suppress unitarity-violating amplitudes.

The effect of the form factor on the transverse-momentum distribution of the hardest tagging jet and the scalar particle is shown in Figure 5.1. For the plot we have used the L3 notation of the dimension-6 operators with the following parameters,

$$d = 0.1, \qquad \Delta g_1^Z = 0.1, \qquad \widetilde{d} = 0.15, \qquad d_B = \Delta\kappa_\gamma = \widetilde{d}_B = \widetilde{\kappa}_\gamma = 0. \tag{5.9}$$

The SM Higgs couplings have been set to zero and typical VBF cuts have been imposed, see Equations (4.7)–(4.9) and (4.13). This parameter point has only been chosen to exemplify the influence of a form factor on distributions although it is already excluded, since the signal strengths are not compatible with LHC data [50, 71, 163]. In the plot, the transverse momentum of the hardest jet and of the scalar particle produced in VBF

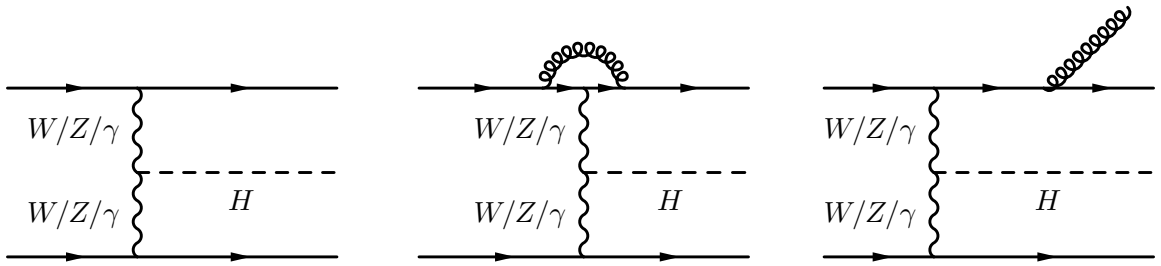

Figure 5.2.: Sample diagrams for Higgs production via VBF including anomalous HVV vertices. The t-channel photon exchange may occur due to anomalous tree-level $H\gamma\gamma$ and/or $HZ\gamma$ vertices.

is shown for the SM and the parameter point defined in Equation (5.9). The colored lines show the curves for various form-factor scales Λ with the form factor F_1 from Equation (5.7) compared to the SM (black). *Prima facie*, unitarity is violated at relatively low transverse momenta for high form-factor scales Λ. A thorough investigation using the "Dipole Form Factor Calculation Tool for Anomalous Couplings in VBFNLO" [164] reveals that, for the parameters defined in Equation (5.9) without a form factor, unitarity is violated above 500 GeV in electroweak gauge-boson scattering, $V_1V_2 \to V_3V_4$, taking into account all neutral V_1V_2/V_3V_4 combinations [165, 166]. To delay unitarity violation to scales above 8 TeV, which is the center-of-mass energy used here, the form-factor scale has to be $\Lambda \leq 487$ GeV. Another notable point is that a form factor can lead to distributions which mimic the SM prediction, a fact that will be explored later on in more detail.

5.3. Elements of the Implementation

In this section we describe the implementation of Higgs boson production via VBF including anomalous HVV vertices in the POWHEG-BOX. Most parts are similar to Z production via VBF (see Section 4.2).

Sample diagrams for the LO, virtual and real contributions are depicted in Figure 5.2. Since we are only interested in Higgs production without subsequent decay no other than the shown types of graphs contribute. The photon exchange in the t-channel is not present in the SM case, since the photon coupling to the SM Higgs boson is loop-induced. Using effective dimension-5 or 6 operators, tree-level couplings are possible. The flavor structures for the Born and real subprocesses are the same as in electroweak Zjj production. Again, the determination of the singular regions is handled by tagging of the quark lines as described in Section 4.2.1. The matrix elements for the Born and real contributions as well as the routines to calculate the SM and the anomalous couplings are taken from VBFNLO [24–26]. External b-quark contributions are neglected and the CKM matrix is set to the unit matrix, which is exact as long as the flavor of the jets is not tagged and quark masses are omitted. Again, the spin-correlated Born matrix elements are not needed since there are no external gluons at tree level (see Equation (3.33)). The color-correlated Born amplitudes are the same as for V production via VBF defined in Equation (4.1). The virtual corrections with anomalous couplings are the same as in the SM case and contain

only vertex corrections [113, 120] (see Figure 5.2). The finite part of the interference between the Born and virtual matrix elements, as defined in Equation (3.36), read

$$\mathcal{V}_{\text{fin}} = C_F \left(-\ln^2\left(\frac{\mu_R^2}{s_{21}}\right) - 3\ln\left(\frac{\mu_R^2}{s_{21}}\right) - \ln^2\left(\frac{\mu_R^2}{s_{43}}\right) - 3\ln\left(\frac{\mu_R^2}{s_{43}}\right) - 16 \right) \mathcal{B}\,, \tag{5.10}$$

where the POWHEG-BOX convention of the normalization (see Equation (3.38)) has been adopted. $\mathcal{B}$ denotes the squared Born matrix element. Again, μ_R is the renormalization scale, s_{21} and s_{43} are the time-like momenta squared of the two exchanged weak bosons (W, Z or γ).

The three parametrizations of anomalous Higgs boson couplings explained in Section 5.2 have been adopted from VBFNLO. The coupling and form-factor parameters can be changed individually. Additionally, the HWW and HZZ tensors present in the SM Lagrangian and the loop-induced SM $H\gamma\gamma$ and $HZ\gamma$ couplings can be multiplied by a global factor.

Even though there already exists a well-tested version of VBF Higgs production in the POWHEG-BOX [120], we use a slightly modified version of this process's phase-space generator. The modifications are required due to photons, which can be exchanged in the t-channel and therefore lead to singularities without proper jet-definition cuts, as described in Section 4.2. These contributions can be cured as described in the last chapter, either by a generation cut on the transverse momentum of the final-state partons or by the Born suppression factor $F(\Phi_n)$ of Equation (4.4). In addition, contributions at LO and NLO with a t-channel photon with virtuality $Q^2 < 4\,\text{GeV}^2$ have to be suppressed with a large damping factor in order to compensate for the singularities arising in the real emission diagrams, as already used in Refs. [106, 115].

The SM matrix elements have been tested against a modified version of the existing POWHEG-BOX SM code [120], which does neither take into account b quarks in the initial or final state nor CKM effects. On the matrix element level, agreement to at least 10 digits has been found. Cross sections and distributions have been compared as well and agree on the sub-per mille level. Using anomalous couplings, matrix elements, cross sections and distributions have been compared with VBFNLO and very good agreement has been found.

5.4. Setup of the Model

For our numerical analysis in Section 5.5, we use the parameter points and form factors given in Table 5.1. For the two scenarios called FF1E and FF2E, which differ in the used form factor, we assume that the new boson discovered at the LHC is not the SM Higgs particle, but a neutral scalar singlet H_S which acts as a Higgs imposter. Therefore, we can use the dimension-5 operators of Equation (5.6). The task of electroweak symmetry breaking is still performed by a SM Higgs boson with a mass above the current exclusion limits for a heavy Higgs boson of roughly 700 GeV [167, 168]. Two of the three scenarios studied here have been derived in Ref. [169]. We will now shortly summarize the determination of these two parameter points.

Parameter Point	Form factor	Coupling parameters
FF1E	F_1, $\Lambda = 100$ GeV	$\Lambda_5 = 200$ GeV, $g_{5e}^{HWW} = -3.282$, $g_{5e}^{HZZ} = 5.058$, $g_{5e}^{H\gamma\gamma} = -5.827 \cdot 10^{-3}$, $g_{5e}^{HZ\gamma} = 9.430 \cdot 10^{-3}$.
FF2E	F_2, $\Lambda = 30$ GeV	$\Lambda_5 = 200$ GeV, $g_{5e}^{HWW} = 1.836$, $g_{5e}^{HZZ} = 2.778$, $g_{5e}^{H\gamma\gamma} = 3.264 \cdot 10^{-3}$, $g_{5e}^{HZ\gamma} = -4.108 \cdot 10^{-3}$.
FF1O	F_1, $\Lambda = 200$ GeV	$\frac{f_{WW}^{\text{odd}}}{\Lambda_6^2} = 5.577 \cdot 10^{-5}$ GeV^{-2}, $\frac{f_{BB}^{\text{odd}}}{\Lambda_6^2} = 5.577 \cdot 10^{-5}$ GeV^{-2}.

Table 5.1.: Form factors and anomalous coupling parameters used for the analysis in Section 5.5. The parameter points FF1E and FF2E are derived using the dimension-5 operators defined in Equation (5.6), for FF1O the parametrization in Equation (5.2) has been used. All other couplings of the Higgs boson to electroweak gauge bosons have been set to zero. The effective gluon-gluon-Higgs coupling and the fermion couplings only enter via the width of the Higgs boson and have been set to their respective SM value.

The anomalous couplings and form factors have been set to values reproducing the SM event rates. First, the form factor scale has been chosen such that the transverse momentum spectra of the two tagging jets in VBF roughly match the corresponding SM curves. Figure 5.1 illustrates the dependence of the p_T spectrum on the scale of the first form factor F_1 of Equation (5.7). In a second step, equations for the event rates, $R_{XY} = \sigma_X \cdot BR_Y$, in dependence on the anomalous couplings have been derived, separately for the production cross section σ_X and the branching ratio of a particular decay channel BR_Y. The formula for the VBF cross section has been deduced using VBFNLO. For gluon fusion in the heavy-top limit, MADGRAPH [170] has been used. The SM couplings of the Higgs boson have been set to zero and only the anomalous couplings have been considered. Although evidence for the Higgs boson decaying to a pair of τ leptons has recently been found [171, 172], couplings of the scalar particle to fermions have been neglected, but could be included in the analysis. Since we only consider non-fermionic final states, only the top quark coupling would have sizable influence on the analysis. It is however encoded in the effective ggH_S coupling.

The following decay modes have been examined,

$$\begin{aligned} &H_S \to \gamma\gamma, \\ &H_S \to Z\gamma \to l^+l^-\gamma, && l = e,\mu, \\ &H_S \to ZZ \to l_1^+l_1^-\, l_2^+l_2^-, && l_{1/2} = e,\mu, \\ &H_S \to W^+W^- \to l_1^+\nu_1\, l_2^-\bar{\nu}_2, && l_{1/2} = e,\mu. \end{aligned} \tag{5.11}$$

The respective expressions in dependence on the anomalous couplings again have been derived using VBFNLO. Afterwards, a χ^2-fit using `MINUIT` version 94.1 [173] has been performed. The values for the anomalous couplings given in Table 5.1 give the lowest χ^2/d.o.f. value for all combinations of branching ratios and production modes (χ^2/d.o.f. = 0.2/16 for both FF1E and FF2E) and can reproduce the SM production cross sections and decay rates. The effective coupling of the Higgs boson to gluons is given by $g_{ggH_S}^{\mathrm{FF1}} = 1.102 \cdot 10^{-2}/\Lambda_5$ and $g_{ggH_S}^{\mathrm{FF2}} = 1.226 \cdot 10^{-2}/\Lambda_5$ with $\Lambda_5 = 200$ GeV.

The other scenario in Table 5.1, FF1O, is an example for purely CP-odd couplings. Although this scenario is already strongly disfavored by experimental data [72–84], we include it to validate the code for CP-odd couplings. Again, the SM couplings of the Higgs boson to electroweak gauge bosons have been set to zero. For more realistic studies it is possible to use CP-even operators combined with CP-odd ones.

In the analysis presented in Section 5.5 the couplings to fermions and gluons are set to their respective SM values for all three scenarios, since they only enter via the width of the scalar particle.

5.5. Numerical Results

The results in this section are obtained assuming a scalar boson with mass $M_H = 126$ GeV for the LHC running at a center-of-mass energy of 8 TeV. We use the `CT10` PDF set [124] with $\alpha_s(M_Z) = 0.11798$ as implemented in the LHAPDF package [125]. The renormalization and factorization scales are set to M_H. The electroweak couplings are calculated via tree-level relations from the input parameters $M_W = 80.398$ GeV, $M_Z = 91.1876$ GeV and the Fermi constant $G_F = 1.16637 \cdot 10^{-5}$ GeV^{-2}. Recombination of partons into jets is done according to the anti-k_T algorithm [126] provided by the FASTJET-package [127, 128] with a distance parameter $R = 0.5$.

We demand at least two well observable jets with a minimum transverse momentum and a maximal rapidity, ensured by

$$p_{T_j} > 20 \text{ GeV} \qquad \text{and} \qquad |y_j| < 4.5. \tag{5.12}$$

The two jets with highest transverse momentum, called tagging jets, are additionally forced to have

$$p_{T_j}^{\mathrm{tag}} > 30 \text{ GeV} \tag{5.13}$$

and a large invariant mass,

$$m_{jj}^{\mathrm{tag}} > 600 \text{ GeV}, \tag{5.14}$$

Scenario	VBFNLO	PWG@NLO	PWG+PYTHIA	PWG+HERWIG++
SM	(305.3 ± 0.2) fb	(305.4 ± 0.2) fb	(292.6 ± 0.6) fb	(286.9 ± 0.6) fb
FF1E	(305.4 ± 0.3) fb	(305.8 ± 0.4) fb	(291.7 ± 0.6) fb	(288.6 ± 0.6) fb
FF2E	(305.4 ± 0.3) fb	(305.2 ± 0.4) fb	(296.2 ± 0.7) fb	(295.7 ± 0.7) fb
FF1O	(304.7 ± 0.2) fb	(304.5 ± 0.3) fb	(295.7 ± 1.0) fb	(289.9 ± 1.0) fb

Table 5.2.: Cross sections for the SM and the scenarios defined in Table 5.1. The first and second column compare the NLO cross sections obtained with VBFNLO and our new implementation. The last two columns show the cross sections for the POWHEG sample showered with PYTHIA and HERWIG++.

to suppress the background from QCD-induced processes. To further suppress these backgrounds, we additionally exploit the VBF signature of two largely separated tagging jets in opposite detector hemispheres,

$$\Delta y_{jj}^{\text{tag}} = |y_1 - y_2| > 4 \qquad \text{and} \qquad y_{j_1} \cdot y_{j_2} < 0. \tag{5.15}$$

The decay of the Higgs boson has not been taken into account and we therefore do not require additional cuts on the possible decay products.

In Table 5.2, we show the cross sections for the SM and the different scenarios defined in Table 5.1. For comparison of fixed order NLO cross sections the value obtained with VBFNLO and the new implementation in the POWHEG-BOX (PWG@NLO) are listed. For the showered results we have used PYTHIA, version 6.4.25 with the Perugia 0-tune (Feb 2009) [27], and HERWIG++, version 2.6.1b [28, 29], respectively, both without hadronization and underlying-event simulation. As already stated in Section 4.3, it is, strictly speaking, not correct to use HERWIG++ as a non-truncated shower in combination with POWHEG-BOX events. We have however seen that the influence of wide-angle soft radiation is negligible in W and Z production via VBF. Since the QCD part of gauge boson and Higgs production is similar, we assume that the effects of truncation are also negligible for this case. We postpone the comparison of HERWIG++ and DS++ [31, 32] to Chapter 7, where we study Higgs production in association with three jets via VBF.

Figure 5.3 displays the differential distributions of the invariant mass of the two tagging jets (top) and the transverse momentum (middle) as well as the rapidity of the hardest jet (bottom), showered with PYTHIA (left) and HERWIG++ (right). In Figure 5.4 the transverse momentum distribution of the second hardest jet (top) and the Higgs boson (middle) as well as the azimuthal angle difference between the two tagging jets (bottom) is shown. All distributions are normalized to the respective total cross section. The distributions in Figures 5.3 and 5.4 show that anomalous couplings combined with the form factors considerably change the tagging jet distributions with respect to the SM. The upper ratio plot of each figure demonstrates BSM effects. While the invariant mass of the two tagging jets (Figure 5.3, top) only receives moderate modifications compared to the SM, BSM effects are evidently more pronounced for the transverse momentum and rapidity spectra.

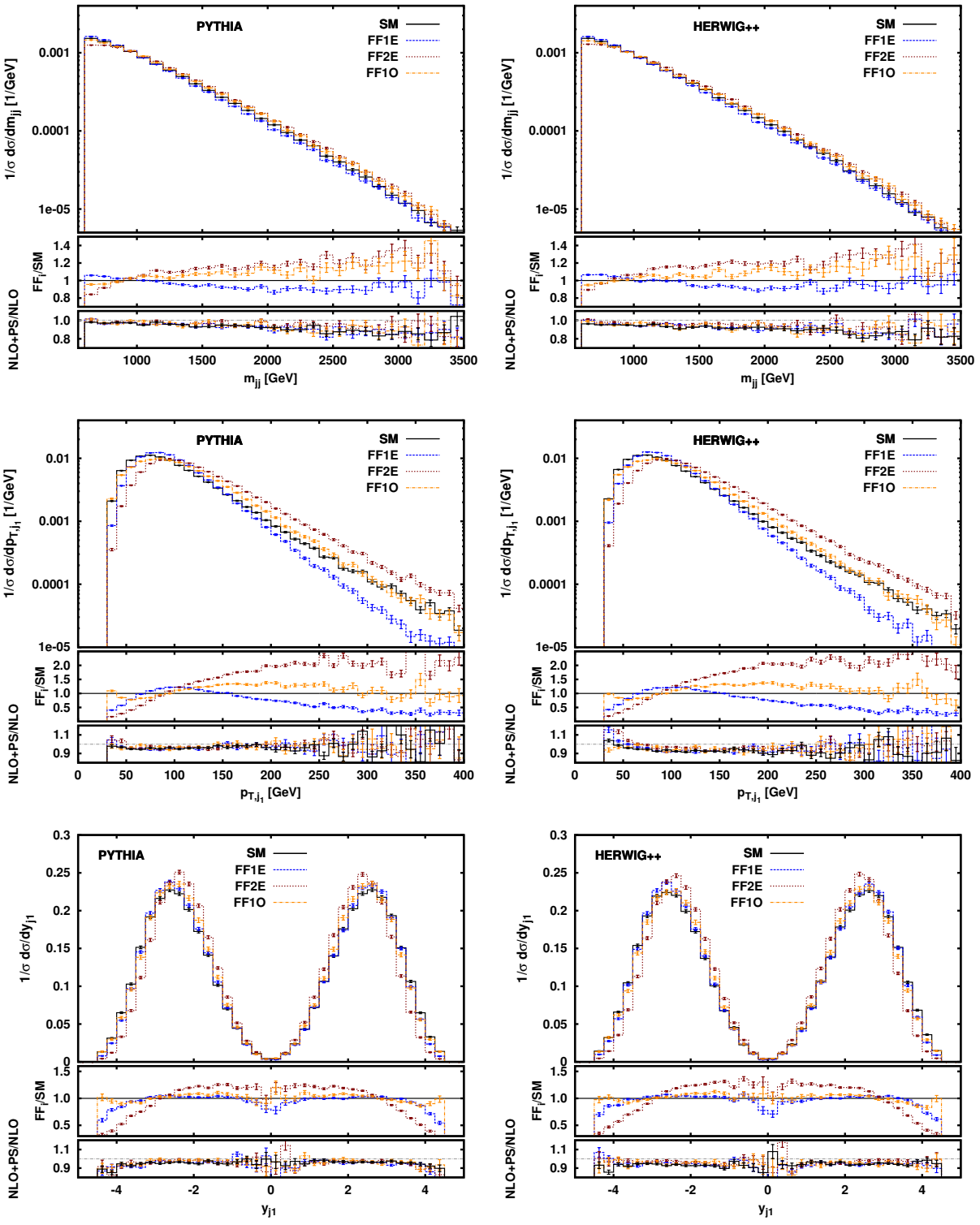

Figure 5.3.: Invariant tagging jet mass (top), transverse momentum (middle) and rapidity of the hardest jet (bottom), showered with PYTHIA (left) and with HERWIG++ (right), respectively. All differential distribution are normalized to the respective cross section from Table 5.2. In each figure, the top ratio plot compares the different BSM scenarios to the SM. The lower ratio plot displays the difference between the showered and the fixed order result. For the ratio plots the normalization has been omitted.

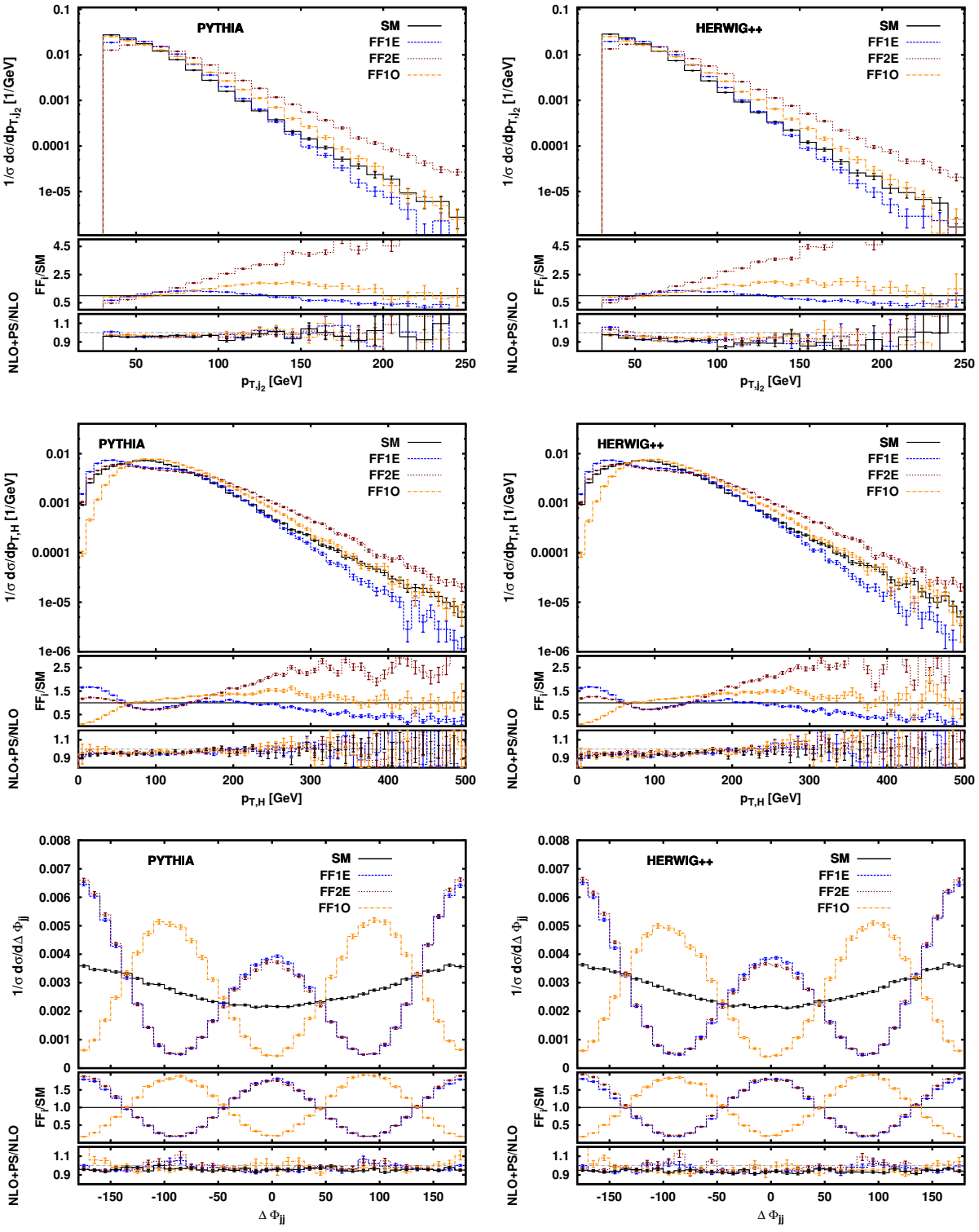

Figure 5.4.: Distributions of the transverse momentum of the second tagging jet (top), of the transverse momentum of the Higgs(-like) boson (middle) and of the azimuthal angle difference of the two tagging jets (bottom), showered with Pythia (left) and Herwig++ (right). The ratio plots are assigned as in Figure 5.3.

For FF1O the tail of the p_{T,j_1} distribution (Figure 5.3, middle) and the y_1 distribution (Figure 5.3, bottom) are almost indistinguishable from the SM curve. The low-p_{T,j_1} region and the p_{T,j_2} distribution (Figure 5.4, top) show deviations. However, the overall agreement with the SM is best, compared to the two singlet scenarios. For FF1E, the damping of the form factor results in a lower event rate in the high-p_T region of the tagging jets compared to the SM. Additionally, the peak of the two tagging jet distributions is shifted to slightly higher values. This property is correlated with the corresponding rapidity distribution, which is lower than in the SM for $|y_1| \gtrsim 3.5$, corresponding to fewer soft jets.

In comparison, for FF2E the damping in the tail of the distribution is much lower and the curve including anomalous couplings by far exceeds the SM distribution. Since those hard jets are more likely produced in the central detector region, the rapidity of the hardest jet is shifted towards zero compared to the SM or to the other scenarios. Additionally, fewer low-p_T tagging jets are expected than in the SM since the cross section has been adjusted to match the SM prediction. Therefore the excess of jets in the high-p_T region has to be compensated. Also the transverse momentum spectrum of the Higgs boson (Figure 5.4, middle) shows sizable deviations from the SM. This shape difference also influences the kinematics of the Higgs decay products.

The argument given above already indicates that the SM Higgs boson can easily be distinguished from singlets parametrized by pure dimension-5 operators like in Equation (5.2). It is possible to adjust the rates and cross sections, but already the tagging jet distributions differ considerably due to the needed low form-factor scale. This behavior has an interesting consequence, especially in the case of the form factor F_2 from Equation (5.8). A form factor of this kind is physically well motivated, since it actually appears in the calculation of triangle graphs. Therefore, the form factor F_2 is particularly adequate to parametrize the effect of (heavy) non-SM particles with a mass at the scale Λ running in loops and inducing effective couplings between the SM particles. It is thus not possible to reproduce the tagging jet distributions of the SM under the assumption of purely loop-induced couplings of the Higgs boson. Already the fitted values for the couplings given in Table 5.1 indicate that the source of the WW/ZZ and $\gamma\gamma/Z\gamma$ couplings cannot be at the same scale, since the values of the coupling parameters show a strong hierarchy.

In general, deviations from the SM Higgs Lagrangian parametrized by higher-dimensional operators will lead to unitarity violating contributions to the S-matrix. They can be suppressed by form factors, which additionally can be adjusted to reproduce the SM tagging jet distributions. It is therefore necessary to look at distributions that do not depend on the form-factor scale to determine the CP properties of the Higgs-like particle discovered at the LHC, like the azimuthal angle difference between the two tagging jets, $\Delta\Phi_{jj}$. As has been discussed in Ref. [136, 142], $\Delta\Phi_{jj}$ is a promising observable to pin down the CP-quantum numbers of the Higgs boson produced in VBF, see the bottom panels of Figure 5.4. The SM distribution is rather flat. The behavior is very different for purely CP-even couplings. Most parts of the cross section lie in the region where the two tagging jets and the beam axis lie in a plane, with two pronounced dips at $\pm 90°$. For CP-odd couplings, the behavior is exactly opposite. The $\Delta\Phi_{jj}$ distribution peaks at $\pm 90°$ and

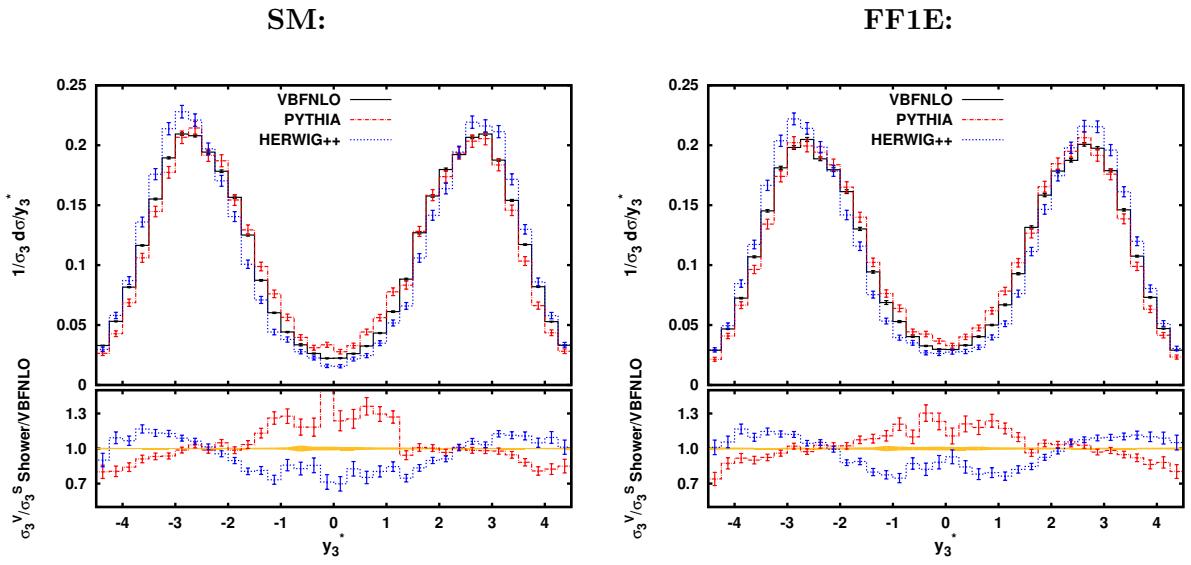

Figure 5.5.: Differential y_3^* distribution as defined in Equation (4.14) for the SM (left) and the parameter point FF1E (right), both normalized to the three-jet cross section. The black curve shows the fixed NLO prediction obtained with VBFNLO, red and blue are the POWHEG-BOX results showered with PYTHIA and HERWIG++. The lower panel shows the ratio between the shower prediction and the fixed-order result.

almost vanishes at 0° and ±180°. In summary, the $\Delta\Phi_{jj}$ distribution is very sensitive to the CP nature of the scalar particle produced in VBF and can therefore be used to distinguish between the SM Higgs boson and scalar particles with CP-even or CP-odd couplings to electroweak gauge bosons.[3]

We now discuss the parton shower effects on the distributions shown in Figures 5.3 and 5.4. The lower panel of each plot shows the ratio between the showered POWHEG-BOX and the NLO prediction. As we already have seen in Chapter 4 and as has been stated for the SM in Ref. [120], the distributions of the tagging jets and electroweak particles are largely unaffected by parton shower effects, apart from the change in the overall normalization, both for HERWIG++ and PYTHIA.

Small differences between the shower corrections for the SM and for the predictions with anomalous couplings occur in the low transverse momentum region of the tagging jets close to the cut, for both parton showers. This inequality is best observed in the lower ratio plot of each figure. The reason for this behavior is that already at fixed order the distributions are very different and a migration of events to the allowed phase-space region is more likely for the parameter points FF1E and FF2E after including parton shower corrections. Additionally, these effects occur in phase-space regions where the prediction with anomalous couplings lies far below the SM curve. The disparity is slightly larger for HERWIG++, but the overall agreement of the two showers is satisfying. For

[3]Also the SM vs. spin-2 distinction can be addressed in the $\Delta\Phi_{jj}$ distribution, see Ref. [174].

the rapidity of the tagging jet, the transverse momentum of the Higgs boson and the azimuthal angle difference between the two tagging jets, the influence of the respective parton shower is only present in the overall normalization of the various curves. Therefore, the discriminative power of the $\Delta\Phi_{jj}$ distribution persists even after including parton shower effects.

As for the SM, differences between the used parton showers become visible starting from the third-hardest jet, whose matrix elements enter the calculation only at LO. In Figure 5.5 we show the rapidity of the third-hardest jet relative to the two tagging jets, see Equation (4.14). The distributions are normalized to the respective three-jet cross section. We observe qualitatively the same behavior as in the discussion of electroweak gauge boson production in VBF presented in Chapter 4. Additionally, the parton shower effects for the SM (left) and the singlet scenario FF1E (right) are essentially the same. We will analyze the non-tagging-jet distribution in VBF Higgs production more thoroughly in Chapter 7.

5.6. Conclusions

We have implemented VBF Higgs boson production with anomalous couplings to electroweak gauge bosons in the POWHEG-BOX. The implementation is based on the already existing SM code [120] and extended by the matrix elements for anomalous couplings based on VBFNLO [24–26]. Three different parametrizations and two form factors have been implemented and can easily be adjusted by the user.

We have shown predictions for three different scenarios and the influence of form factors on these predictions. Observables related to the two tagging jets are hardly affected by parton showers and can be used to distinguish a SM Higgs boson from a scalar Higgs imposter whose couplings to SM particles are parametrized by dimension-5 operators. Additionally, the azimuthal angle difference of the two tagging jets is a suitable observable to distinguish between CP-even and CP-odd couplings of scalar particles to electroweak gauge bosons, even after including parton shower effects.

An important result of this analysis is, that parton shower effects barely depend on the nature of the produced scalar particle. Noticeable differences between parton shower effects on the SM and on the examined BSM scenarios only occur in phase-space regions close to cuts due to the migration of events, or where the BSM curves lie far below the SM ones. Therefore it is possible to perform a parton shower on generated NLO events and *afterwards* take anomalous couplings into account by reweighting SM events. We will explain this method in more detail in the next chapter.

CHAPTER 6

REPOLO

In this chapter we present the program Repolo, an add-on to the parton-level Monte Carlo generator Vbfnlo [24–26]. Repolo can be used to reweight Les Houches event files [33, 34] generated for SM Higgs production via vector-boson fusion (VBF) to account for two different beyond the SM (BSM) scenarios or for signal-background interference effects, which are important for heavy Higgs boson searches. Part of this work has been presented in the "Handbook of LHC Higgs Cross Sections: 3. Higgs Properties", CERN-2013-004 [58].

6.1. Introduction

To exploit the physics potential of the LHC, accurate simulations of both signal and background processes have to be provided. These include, besides generating NLO events with a subsequent parton shower, also a full detector simulation. Running all these tasks is, however, time consuming and computationally intensive. Therefore, we have developed the Repolo framework, which allows to change certain parameters of the NLO events, like for instance the couplings of the Higgs boson to electroweak gauge bosons parametrized by an effective Lagrangian like introduced in Chapter 5. Since the event kinematics stay unaltered during the reweighting, the parton shower effects and detector simulation of the SM events can be reused.

Repolo, which stands for REweighting POwheg events at Leading Order, takes Les Houches event (LHE) files as input and assigns a new weight to each event by using the Vbfnlo framework. The reweighting is achieved by calculating the ratio of the squared matrix element with the chosen reweighting option and the squared matrix element of the input event within the SM. LO in Repolo thereby refers to the fact that the new weight is calculated according to the kinematics of each event, which signifies that we distinguish between Born and real-emission matrix elements. Virtual corrections and the corresponding subtraction terms for Born-like kinematics are not taken into account. The

method has been developed and tested for Higgs boson production in VBF, but can easily be generalized to other classes of processes like for instance triple gauge-boson production.

REPOLO has two fields of application: BSM predictions and heavy Higgs reweighting. The first running mode comprises the reweighting of SM events by the use of anomalous couplings or by a spin-2 model and is explained in Section 6.2. The latter application is used to account for signal-background interference effects in searches for a heavy Higgs boson, which we describe in Section 6.3.

6.2. BSM Predictions

One application of REPOLO is the reweighting of SM events to account for two different BSM scenarios, namely anomalous Higgs boson couplings or a spin-2 model. The idea of the program is as follows: REPOLO reads in a LHE file and, using the VBFNLO framework and a `perl` script, creates a new event file where each SM event is reweighted by a factor

$$\frac{|\mathcal{M}_{\mathrm{BSM}}|^2}{|\mathcal{M}_{\mathrm{SM}}|^2}. \tag{6.1}$$

Here, $\mathcal{M}_{\mathrm{SM}}$ and $\mathcal{M}_{\mathrm{BSM}}$ denote the matrix elements of the SM and the chosen BSM scenario, respectively.

6.2.1. Details of the Implementation

REPOLO can reweight SM events to two different types of BSM scenarios: anomalous HVV couplings as described in Section 5.2 and a spin-2 model explained in detail in Refs. [174–176]. In the latter model the interactions of a singlet spin-2 boson T to electroweak gauge bosons is parametrized by an effective Lagrangian with mass-dimension 5,

$$\mathcal{L}_{\mathrm{singlet}} = \frac{1}{\Lambda} T_{\mu\nu} \left(f_1 B^{\alpha\nu} B^{\mu}{}_{\alpha} + f_2 W_i^{\alpha\nu} W^{i,\mu}{}_{\alpha} + 2 f_5 (D^{\mu}\Phi)^{\dagger} (D^{\nu}\Phi) \right). \tag{6.2}$$

As in the anomalous HVV case, Λ is the energy scale of the underlying new physics. The parameters f_i denote free coupling constants, which can be adjusted to reproduce SM-like rates. The mass of the spin-2 particle is a free parameter. The couplings to fermions and gluons are not present here since they do not enter in VBF processes with subsequent decay into gauge bosons, but can be included [175]. In contrast to the graviton Lagrangian [177], the coupling constants f_i are independent, free parameters and not fixed to the same value by the underlying theory.

Also in this BSM model, unitarity is violated above a certain energy scale. To suppress these unphysical contributions to the S-matrix, a form factor similar to F_1, as defined in Equation (5.7), is used,

$$f(p_1^2, p_2^2, k_{\mathrm{sp2}}^2) = \left(\frac{\Lambda_{\mathrm{ff}}^2}{|p_1^2| + \Lambda_{\mathrm{ff}}^2} \cdot \frac{\Lambda_{\mathrm{ff}}^2}{|p_2^2| + \Lambda_{\mathrm{ff}}^2} \cdot \frac{\Lambda_{\mathrm{ff}}^2}{|k_{\mathrm{sp2}}^2| + \Lambda_{\mathrm{ff}}^2} \right)^{n_{\mathrm{ff}}}, \tag{6.3}$$

where p_1^2 and p_2^2 are the invariant masses of the gauge bosons in the t-channel and k_{sp2}^2 denotes the invariant mass of the spin-2 particle in the s-channel. The scale of the cut-off Λ_{ff} and the suppression power n_{ff} are free parameters. All the variables of the model can be set in the file `spin2coupl.dat`, parameters for anomalous HVV vertices are specified in `anom_HVV.dat`.

The reweighting procedure in Repolo has four parts,

1. the specification of the input parameters,
2. the import of the momenta from the LHE event file,
3. the matrix-element calculation,
4. the reweighting of the original file using a `perl` script.

The main input parameters can be set in `repolo.dat`, the main input file for Repolo. All important parameters which can be adjusted are explained in Appendix A. The key parameter is the `procID`, which specifies the used process. So far, VBF Higgs production with all non-hadronic decay modes as implemented in Vbfnlo are available. Additionally, the BSM model and the respective coupling parameters have to be set in the aforementioned input files. With this information, the couplings needed for the matrix-element evaluation are initialized.

Afterwards, the events from the LHE file have to be imported. The main structure of such files is explained in Appendix B. The `init` block of the LHE file is not relevant. First, for each `event` block the number of particles `NUP` is read in. From this number we decide whether the event has Born or real-emission kinematics. For VBF Higgs production without subsequent decay of the scalar boson, `NUP` $= 6$ corresponds to a real-emission event, while `NUP` $= 5$ exhibits Born kinematics. In a Powheg-Box LHE file, which exhibits formal NLO accuracy, nearly all events have real-emission kinematics, as they are generated according to the Powheg formula as defined in Equation (3.22). The additional radiation is described by the real-emission matrix element, whereas virtual corrections only enter via the normalization, i.e. the total cross section. Therefore it is sufficient to consider only the LO (Born and real-emission) matrix elements in the ratio defined in Equation (6.1) to preserve NLO accuracy, as long as the QCD corrections to the chosen BSM scenario and the SM only differ in the occurring coupling constants, which factorize for VBF Higgs production for individual phase-space points. In Repolo, the `NUP` information determines which matrix element, Born or real emission, will be evaluated later on.

Afterwards, the particle IDs, color information and momenta are read in. Since the LHE file also contains information on the incoming particles, the whole event kinematics and color flow can be deduced. One important point for the real-emission kinematics is the position of the gluon for final-state radiation. The color flow determines whether the gluon is emitted from the upper or lower quark line. This information is used later on when evaluating the real-emission matrix elements. The momenta of the colored and colorless particles are used in the following stage. There, the squared matrix elements within the SM and the BSM scenario, $|\mathcal{M}_{\text{SM}}|^2$ and $|\mathcal{M}_{\text{BSM}}|^2$, are calculated and stored in two files,

`rew_sm.dat` and `rew_bsm.dat`. As mentioned before, we distinguish between Born and real-emission kinematics. For events with three partons in the final state, the position of the gluon (incoming or outgoing, upper or lower quark line) is taken into account. The PDFs are not needed here, since they cancel in the ratio defined in Equation (6.1). Also the scale μ_R used to calculate $\alpha_s(\mu_R)$ has no influence since the same power of α_s appears in $\mathcal{M}_{\rm SM}$ and $\mathcal{M}_{\rm BSM}$ and the kinematics is the same for each event. Since for $H \to \gamma\gamma$ and the two $H \to ZZ$ decay modes full off-shell effects and spin correlations are included, the standard random helicity summation used in VBFNLO has had to be changed into a full helicity summation.

In the last step, a `perl` script assigns a new weight,

$$\texttt{XWGTUP}_{\rm new} = \frac{|\mathcal{M}_{\rm BSM}|^2}{|\mathcal{M}_{\rm SM}|^2}\,\texttt{XWGTUP}_{\rm old}, \tag{6.4}$$

to each event in the original LHE file. With this definition of the new weight, $\texttt{XWGTUP}_{\rm new}$, the method works for both weighted and unweighted events in the LHE input file.

As we will see below, the reweighting method does, however, have limitations in regions where

$$|\mathcal{M}_{\rm SM}|^2 \ll |\mathcal{M}_{\rm BSM}|^2.$$

In these regions a single point with a large reweighting factor can effectively destroy a distribution.

6.2.2. Results

In this section we validate the REPOLO method using three examples for BSM physics, the parameter point FF1E defined in Section 5.4, a Higgs boson with SM-like couplings and an additional admixture of CP-odd couplings, and the aforementioned spin-2 model.

We first come back to the parameter point FF1E defined in Table 5.1. As we have seen in the last chapter, the used form-factor scale $\Lambda = 100$ GeV results in a sizable damping in the high-p_T tales of the hardest jet and the scalar particle compared to the SM. Therefore we now vary the form-factor scale Λ using REPOLO to see if a different scale is better suited to reproduce the SM curves.

In Figures 6.1 and 6.2 we show various normalized distributions for the parameter point FF1E with different scales of the form factor F_1, defined in Equation (5.7), and for the SM. In the left column, the NLO predictions obtained with VBFNLO are displayed, the right column shows the reweighted distributions at the LHE level using REPOLO. For the reweighted curves we have used 1 million POWHEG-BOX SM events generated for the discussion in Chapter 5 as input. We have imposed typical VBF cuts as defined in Equations (5.12)–(5.15). The upper and lower panel in Figure 6.1 display the transverse momentum of the hardest jet and of the scalar particle produced in VBF. The lowest form-factor scale $\Lambda = 100$ GeV reproduces the SM curves best. Higher scales Λ imply too

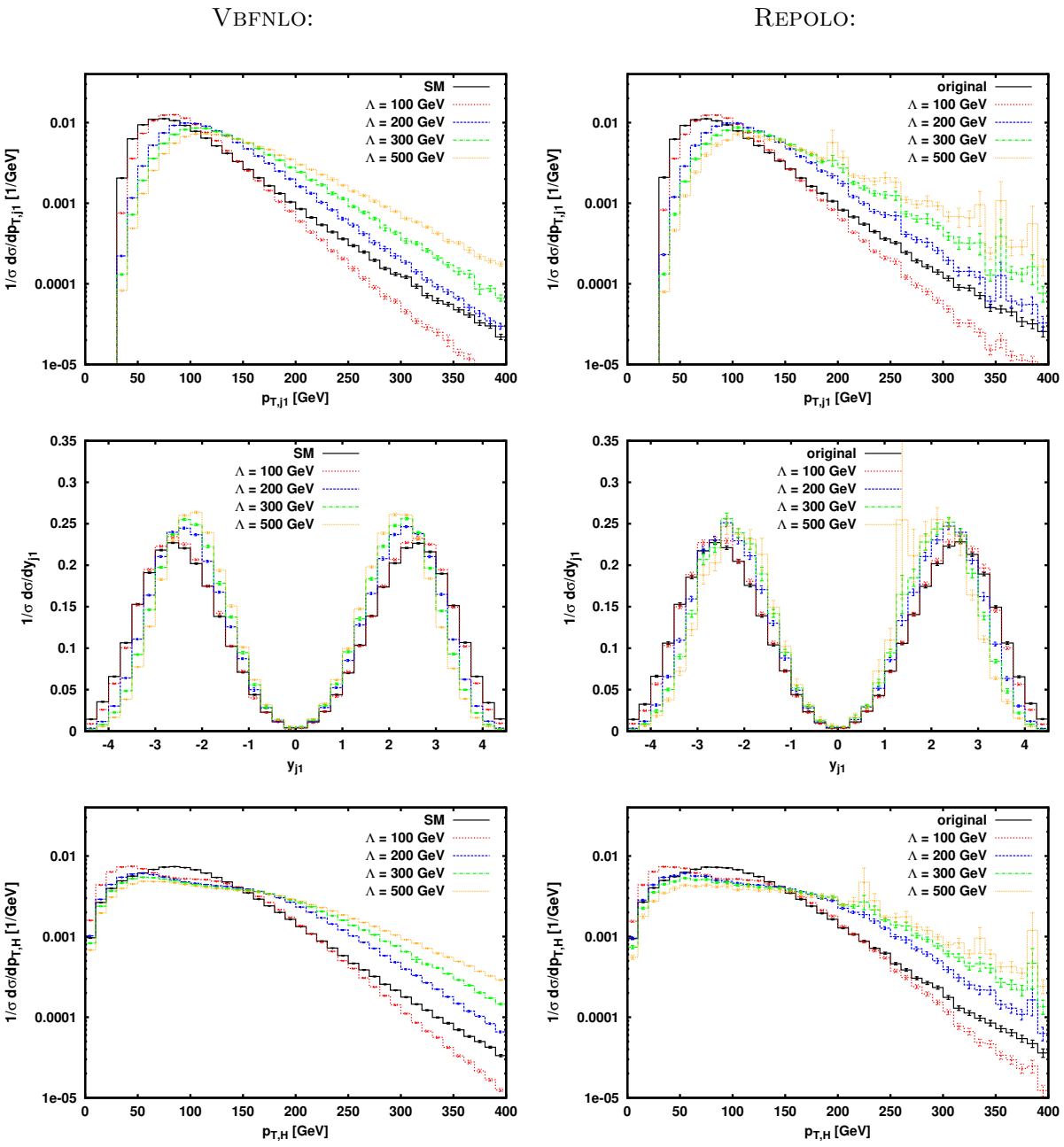

Figure 6.1.: Differential distribution of the transverse momentum of the hardest jet (upper panels), of its rapidity (middle panels) and of the transverse momentum of the scalar boson (lower panels) for the SM (black) and the parameter point FF1E defined in Table 5.1 for different form-factor scales Λ (colored lines). The left plots show the distributions obtained with VBFNLO at NLO accuracy, the right ones the reweighted distributions at the LHE level obtained with REPOLO using POWHEG-BOX SM events as input.

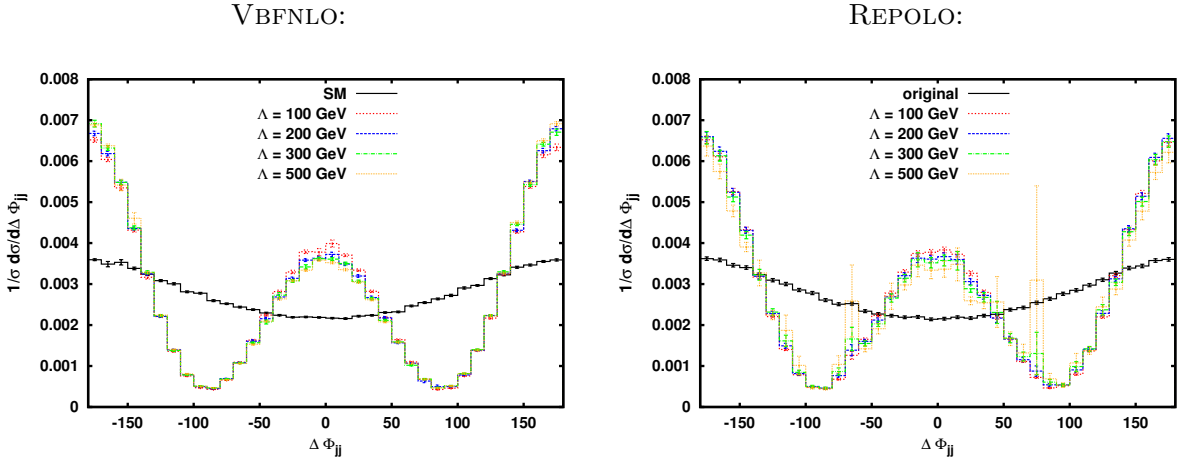

Figure 6.2.: Differential distribution of the azimuthal angle difference of the two tagging jets in the SM (black) and with the parameter point FF1E for different form-factor scales Λ (colored lines). The left plots show the distributions obtained with VBFNLO at NLO accuracy, the right ones the reweighted distributions obtained with REPOLO at the LHE level using POWHEG-BOX SM events as input.

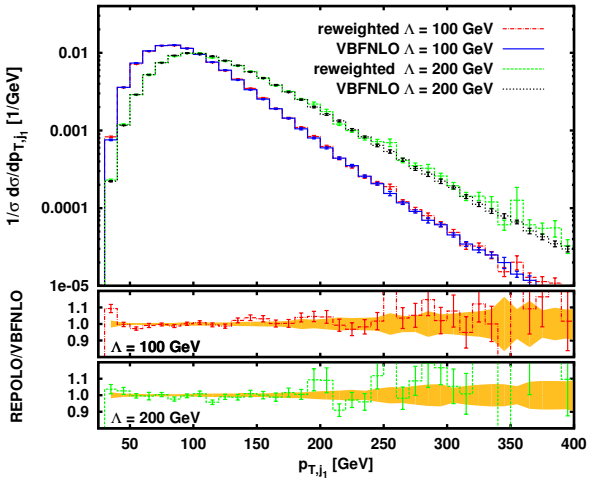

Figure 6.3.: Differential distribution of the transverse momentum of the hardest jets for the parameter point FF1E with two different form-factor scales Λ, obtained with VBFNLO and REPOLO, normalized to the respective cross section. The two lower panels of the figure show the ratio between the REPOLO and the VBFNLO prediction for $\Lambda = 100$ GeV and 200 GeV. The yellow error band indicates the statistical error of the respective VBFNLO distribution.

little damping and/or the peak of the transverse momentum distribution of the tagging jet is shifted to higher values.

Clearly, Repolo is able to reproduce the Vbfnlo predictions. The $\Lambda = 100$ GeV and $\Lambda = 200$ GeV curves obtained with the two programs are in very good agreement. In Figure 6.3 we display the comparison between the two predictions for the transverse momentum distribution of the hardest jet. Starting from $\Lambda = 300$ GeV, the overall compliance between Vbfnlo and Repolo is still satisfying, but the distributions get more and more spiky. There are two reasons for this behavior: On the one hand, statistics get worse since there are not many events with partons that end up in the tails of the p_T distributions. On the other hand, the BSM curves are enhanced by approximately one order of magnitude compared to the SM.

In these regions the procedure has its limitation, since a single point with a large reweighting factor can effectively destroy a distribution. The consequences are shown in the middle panel of Figure 6.1 and in Figure 6.2, where the rapidity of the hardest tagging jet and the azimuthal angle difference between the two tagging jets is displayed. Especially for a form-factor scale $\Lambda = 500$ GeV there are large fluctuations. To cure this behavior, one should either increase statistics in phase-space regions where the SM is suppressed compared to the BSM prediction or use dedicated cuts to prevent the reweighting of these events. If the BSM distributions show only mild deviations from the SM, it is however possible to safely reweight the SM LHE files using Repolo, which is true for low form-factor scales Λ in Figure 6.1 and 6.2. As mentioned before, NLO effects are adequately taken into account and therefore the NLO accuracy of the LHE input file is preserved.

After we have shown that the method used in Repolo works, but has its limitations in certain phase-space regions, we now look at a more realistic, SM-like scenario by means of anomalous couplings: the SM Lagrangian and the couplings derived there get an additional contribution of three CP-odd operators in the parametrization used by the L3 collaboration [161],

$$\frac{g}{2M_W}\widetilde{d}_B \left(\cos^2\theta_W H\widetilde{A}_{\mu\nu}A^{\mu\nu} - \sin 2\theta_W H\widetilde{A}_{\mu\nu}Z^{\mu\nu} + \sin^2\theta_W H\widetilde{Z}_{\mu\nu}Z^{\mu\nu}\right) \tag{6.5}$$

with $\widetilde{d}_B = 0.15$. Together with the form-factor F_1 from Equation (5.7) with a scale $\Lambda = 100$ GeV the production cross section stays almost unaltered compared to the SM due to the dominance of the W exchange in the t-channel, whereas the decay rates of the Higgs boson into $\gamma\gamma$, $Z\gamma$ and ZZ are enhanced. Although this enhancement is too large to be compatible with LHC data [49, 50, 71, 163], this scenario has been selected to show the influence of an admixture of CP-odd couplings on distributions.

In Figure 6.4 we demonstrate the influence of these additional CP-odd couplings on the transverse momentum distribution of the hardest jet, the invariant mass of the two tagging jets and the azimuthal angle difference between the two tagging jets. For the analysis we have again imposed typical VBF cuts (Equations (5.12)–(5.15)). As input we have used 1 million SM events obtained with the Powheg-Box and have reweighted them using Repolo. In the plot, the reweighted curve is at the LHE level, whereas the SM and

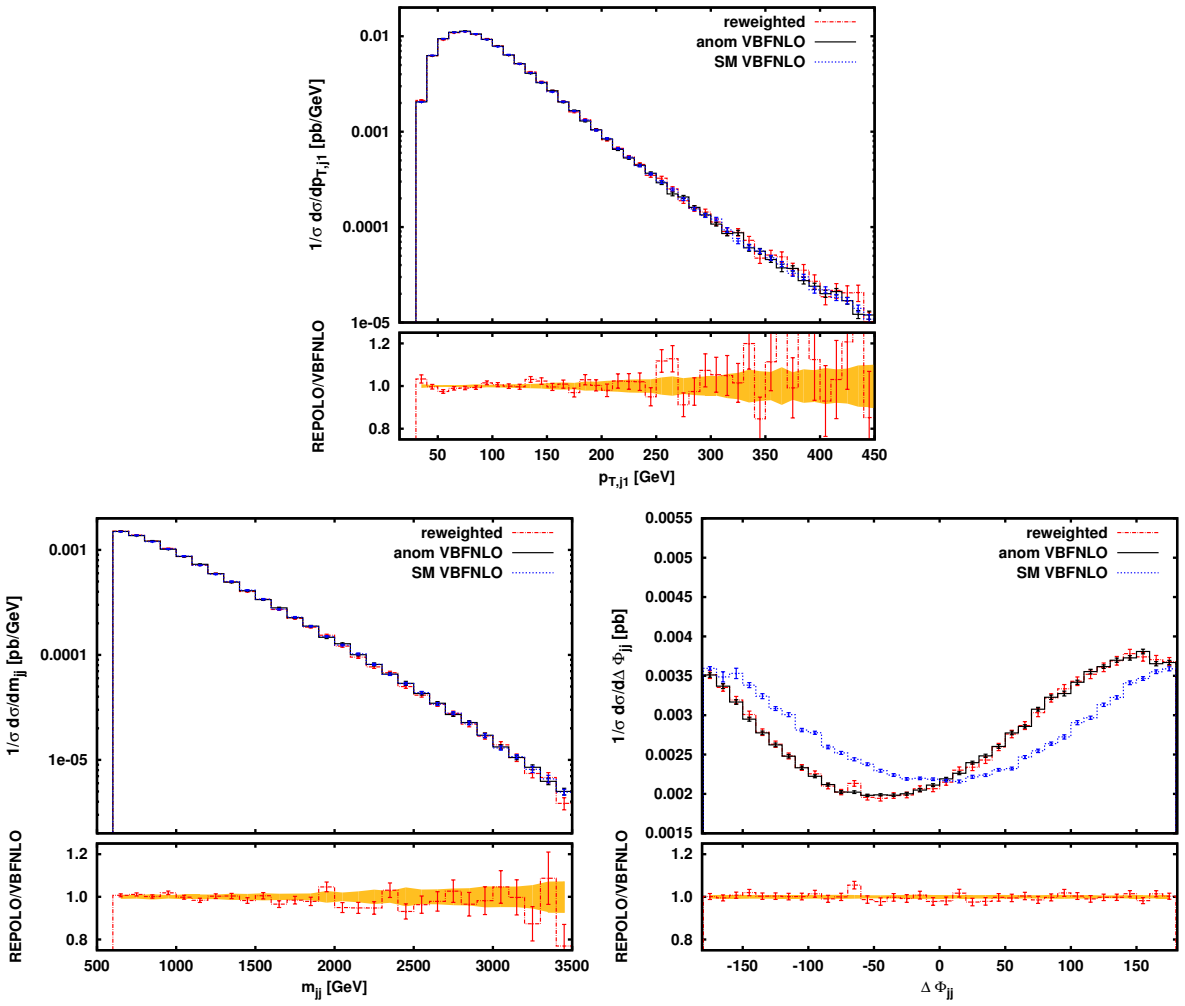

Figure 6.4.: Transverse momentum of the hardest tagging jet (top), invariant tagging jets mass (bottom left) and azimuthal angle difference between the two tagging jets (bottom right) for VBF Higgs production in the SM (blue) and with an additional admixture of CP-odd couplings (see Equation (6.5)) obtained with VBFNLO (black) and with REPOLO (red). The reweighted curve is at the LHE level, the VBFNLO prediction exhibits NLO accuracy. The lower panel of each plot shows the ratio of the BSM predictions obtained with REPOLO and VBFNLO.

BSM curves to compare with are fixed NLO distributions obtained with VBFNLO. The ratio plots display the deviations of the respective reweighted distribution compared to the VBFNLO curve with the admixture of CP-odd couplings as specified in Equation (6.5). Obviously, the agreement between the two is excellent and the NLO accuracy of the SM LHE file is indeed preserved. Additionally, only the azimuthal angle difference between the two tagging jets is affected by the anomalous couplings, while the other distributions, like the invariant tagging jet mass, stay unaltered compared to the SM. Therefore it is essential to look at differential distributions to distinguish the SM Higgs boson from a BSM scenario where an admixture of CP-odd couplings is present.

We give one last example for the application of BSM physics using REPOLO, the spin-2 model introduced in Equation (6.2). We use the scenario defined in Ref. [175], since with the parameters specified there, the decay rates, VBF cross section and some distributions can mimic a SM Higgs boson. The parameters for the couplings are chosen as

$$f_1 = 0.04, \qquad f_2 = 0.08, \qquad f_5 = 10.0, \qquad \Lambda = 6.4 \text{ TeV}, \tag{6.6}$$

and the parameters for the form factor as defined in Equation (6.3) are

$$n_{\text{ff}} = 3 \qquad \text{and} \qquad \Lambda_{\text{ff}} = 400 \text{ GeV}. \tag{6.7}$$

For this example we have used 5 million LO VBF Higgs events generated with VBFNLO taking into account the decay of the Higgs boson into two photons. Taking NLO events produced with the help of the POWHEG-BOX would have also been possible, but a large number of events is required to receive meaningful results and the decay of the Higgs boson into two photons is not included in the POWHEG-BOX. We have once again imposed typical VBF cuts (Equations (5.12)–(5.15)) and, in addition, very inclusive cuts for the photons,

$$|\eta_\gamma| < 3.5, \qquad p_{T,\gamma} > 5 \text{ GeV}, \qquad R_{\gamma\gamma} > 0.1 \qquad \text{and} \qquad R_{j\gamma} > 0.4. \tag{6.8}$$

In Figure 6.5 we display the transverse momentum distribution of the two tagging jets (top), the azimuthal angle difference between the two tagging jets (bottom left) and the two photons (bottom right). Again, the lower panel of each plot shows the ratio of the reweighted events compared to the LO VBFNLO prediction for the spin-2 scenario defined in Equation (6.6). The agreement between the two distributions is excellent. From the physics point of view it is important to notice that such a spin-2 model is able to mimic a SM Higgs boson concerning the tagging jet distributions. Nevertheless, the azimuthal angle difference between the two tagging jets and the two photons can be used to distinguish the SM from such a BSM scenario. However, these azimuthal angle differences are again distribution measurements and can therefore be influenced by parton shower effects, which can be simulated using the distribution reweighted with REPOLO.

In conclusion it can be said that the method used in REPOLO works very well to reweight SM LHE files to account for BSM physics. Even NLO accuracy is preserved when taking POWHEG-BOX input files. However, there are some drawbacks mainly due to statistical fluctuations since a single point with a large weight can effectively destroy distributions.

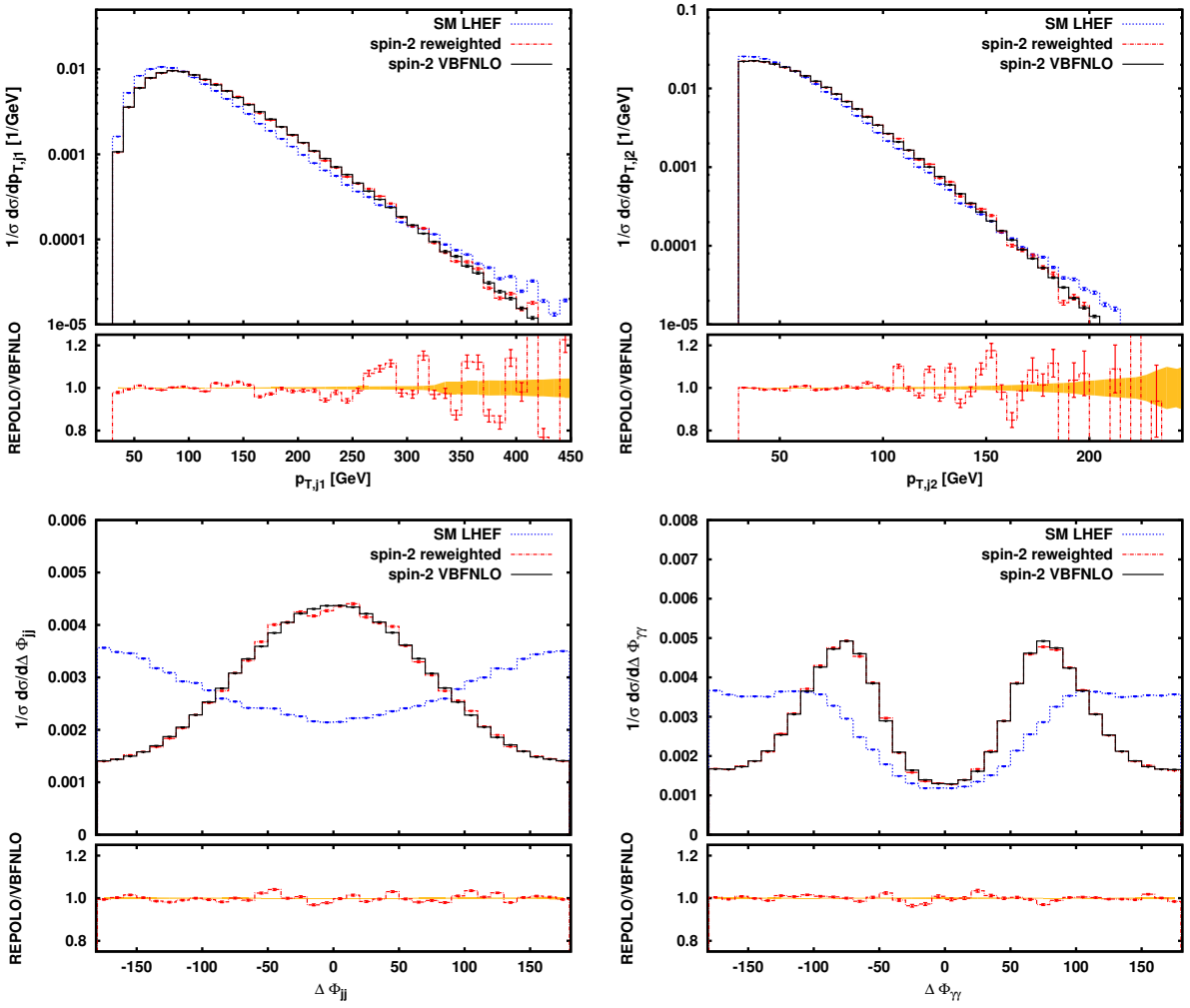

Figure 6.5.: Transverse momentum distribution of the two tagging jets (top) and azimuthal angle difference between the two tagging jets (bottom left) and the two photons emerging from the Higgs/spin-2 particle decay (bottom right). The blue curves show the original SM distribution at the LHE level (LO), the red curves display the reweighted distribution using REPOLO, black is the VBFNLO prediction for the spin-2 model at LO. The lower panel shows the deviation of the REPOLO result from the BSM VBFNLO prediction.

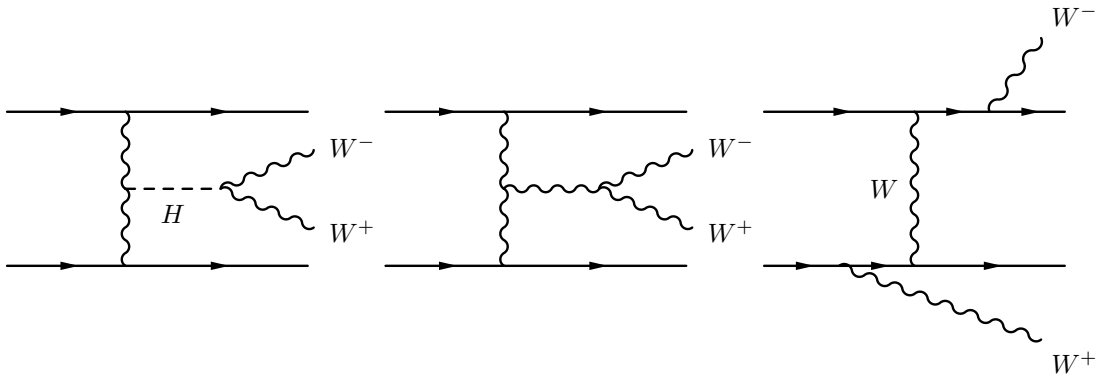

Figure 6.6.: Sample diagrams contributing to the process $pp \to l^+\nu_l\, l^-\bar{\nu}_l\, jj$. The leptonic W decay is not depicted. The left and middle diagrams contribute, *inter alia*, to diboson scattering, $VV \to WW$.

6.3. Heavy Higgs Reweighting

Another field of application for Repolo are searches for a heavy Higgs boson. In this section we assume for simplicity that the heavy Higgs boson has SM couplings.

Two important aspects have to be considered when the Higgs mass is larger than roughly 400 GeV. The line shape in NLO Monte Carlo generators is usually described via a Breit-Wigner distribution. This approximation has an accuracy of Γ_H/M_H, which is of the order of 10% for a Higgs boson mass of 450 GeV. As a solution the Complex-Pole Scheme (CPS) [178, 179] has been proposed and is implemented in the Powheg-Box. We introduce this prescription in Section 6.3.2 and explain the differences compared to the standard implementation used in Vbfnlo.

Another important effect is the interference of the resonant Higgs boson production contributions, e.g. $pp \to Hjj \to l^+\nu_l\, l^-\bar{\nu}_l\, jj$, and non-resonant background diagrams without Higgs boson contributions, $pp \to l^+\nu_l\, l^-\bar{\nu}_l\, jj$. Therefore a consistent definition of the signal process has to be established. This problem is addressed in Section 6.3.1. As we explain in Section 6.3.3, Repolo has been modified to read in Powheg-Box events containing the CPS prescription and to assign a new weight to each event. The new weight takes into account signal-background interference effects.

6.3.1. Signal Definition

In VBF the interference between diagrams containing a Higgs boson and background diagrams where no Higgs boson is present becomes more and more important when going to higher Higgs boson masses. The NLO QCD corrections to the full $pp \to VVjj$ processes in the VBF approximation have been calculated in Refs. [180, 181] and are available in Vbfnlo. Some sample diagrams contributing to the process $pp \to l^+\nu\, l^-\bar{\nu}\, jj$ are shown in Figure 6.6.

To assure the correct, unitary high-energy behavior of the SM, both Higgs and continuum diagrams without Higgs boson contributions have to be taken into account. Looking at

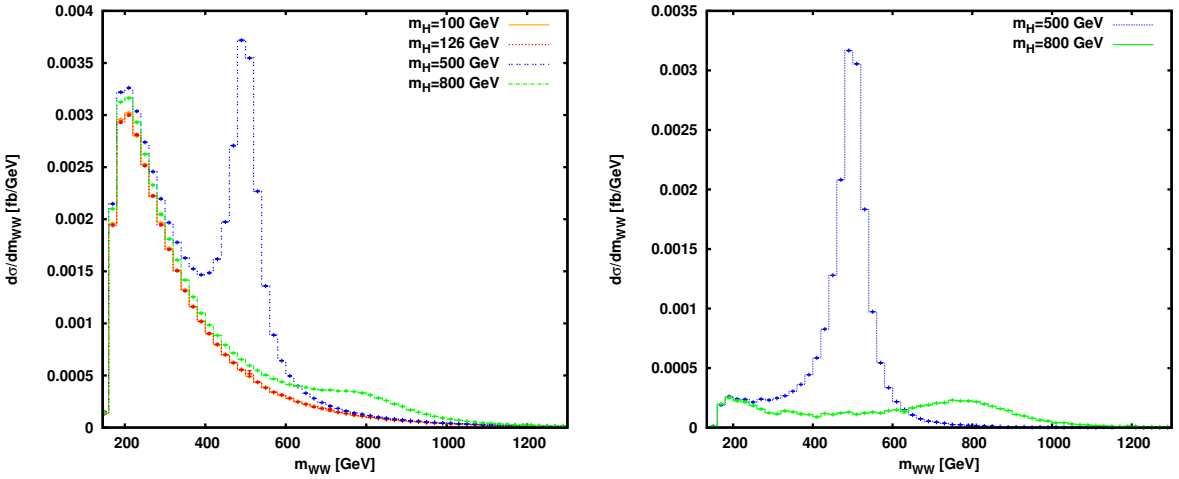

Figure 6.7.: Invariant $e^+\nu_e\,\mu^-\bar{\nu}_\mu$ mass distribution for VBF WW production with different Higgs boson masses. Left: The full process including also the continuum diagrams. Right: σ_{S+I} of Equation (6.12) with subtraction of the background $\sigma_B(m_h = 126\text{ GeV})$.

vector-boson scattering, $VV \to VV$, the continuum matrix elements $\mathcal{M}_B$ behave like $-\frac{s}{v^2}$ when increasing $\sqrt{s}$, which denotes the invariant mass of the two vector bosons in the initial/final state, v is the expectation value of the SM Higgs doublet. This high-energy behavior would lead to unitarity violation at scales roughly around $\sqrt{s} \approx 1$ TeV. However the sum of diagrams containing a Higgs boson, $\mathcal{M}_H$, is proportional to $\frac{s}{v^2}$ and exactly cancel the unitarity-violating behavior of the continuum diagrams. A naive definition of the signal cross section for Hjj production via VBF, $\sigma_{S,\text{naive}}$, where only the interference is taken into account,

$$\sigma_{S,\text{naive}} = \int \mathrm{d}\Phi \left(|\mathcal{M}_H + \mathcal{M}_B|^2 - |\mathcal{M}_B|^2 \right), \tag{6.9}$$

will lead to unitarity violation for large invariant masses of the diboson system due to the last term. Here, $\mathrm{d}\Phi$ denotes the phase-space integration variables. Due to the poor high-energy behavior of $\sigma_{S,\text{naive}}$, a different, more thoughtful definition for the signal cross section σ_S has to be given.

In the left plot of Figure 6.7 we show the invariant WW mass for $pp \to e^+\nu_e\,\mu^-\bar{\nu}_\mu\,jj$ production via VBF for a SM Higgs boson with $m_H = 100, 126, 500$ and 800 GeV. The peaks corresponding to the two light Higgs bosons are outside the shown invariant-mass range. The plots are at NLO and have been generated using VBFNLO. Besides standard jet and lepton definition cuts ($p_{T,j} > 20$ GeV, $|y_j| < 4.5$, $R_{jj} > 0.5$, $p_{T,l} > 5$ GeV, $|\eta_l| < 2.5$) we have additionally imposed typical VBF cuts ($\Delta y_{jj}^{\text{tag}} > 4$, $m_{jj}^{\text{tag}} > 400$ GeV). The two curves for the two light Higgs masses are in very good agreement. Only in the vicinity of the WW threshold a small dependence on the Higgs boson mass is present. Since the full process with a light Higgs boson is well-defined we use it to define the background as

$$\sigma_B = \int \mathrm{d}\Phi \, |\mathcal{M}_B + \mathcal{M}_H(m_h)|^2 . \tag{6.10}$$

As before, $\mathcal{M}_B$ denotes continuum diagrams and $\mathcal{M}_H(m_h)$ are the diagrams containing a Higgs boson with a low mass $m_h \lesssim 126$ GeV. This contribution can safely be subtracted from the full process with a high Higgs mass m_H,

$$\sigma_{S+B+I} = \int \mathrm{d}\Phi \, |\mathcal{M}_B + \mathcal{M}_H(m_H)|^2 \tag{6.11}$$

leading to our definition of the signal plus interference contribution,

$$\sigma_{S+I} = \sigma_{S+B+I} - \sigma_B. \tag{6.12}$$

In the right plot of Figure 6.7 we show the invariant diboson mass for σ_{S+I}, where the background has been subtracted using a light Higgs boson with $m_H = 126$ GeV.

6.3.2. The Complex-Pole Scheme

In this section we introduce the Complex-Pole scheme (CPS) following the arguments given in Ref. [179]. To account for the off-shellness of the Higgs boson in Monte Carlo generators, often a Breit-Wigner distribution for the Higgs boson is assumed. This shape, however, cannot be derived from Quantum-Field Theory and additionally violates unitarity in VV scattering. Therefore the full propagator should be used when calculating the cross section. Another ambiguity arises when one tries to split the full cross section into the production cross section and the branching ratio since they are known to different orders in perturbation theory. The ttH production cross section is, for instance, only known to NLO accuracy in QCD [182–185], whereas the decay rate $H \to b\bar{b}$ can be calculated within massless QCD up to N^{3}LO accuracy, see Ref. [186] and references therein. We write the full cross section including production, decay and the full propagator for the Higgs boson in a symbolic manner,

$$\sigma_{\text{full}} = \int \mathrm{d}\Phi_{\text{decay}} \, \mathrm{d}\Phi_{\text{prod}} \, \frac{\mathrm{d}q^2}{2\pi} \left| \mathcal{M}_{\text{prod}}(q^2) \, \frac{1}{(q^2 - m^2) + im\Gamma} \, \mathcal{M}_{\text{decay}}(q^2) \right|^2 . \tag{6.13}$$

In our notation, we omit all dependence of the production and decay matrix elements, $\mathcal{M}_{\text{prod}}$ and $\mathcal{M}_{\text{decay}}$, on phase-space variables other than the invariant mass q of the produced Higgs boson with mass m and total width Γ. As the Higgs boson is a scalar particle, there are no spin correlations between production and decay side, and the square of the absolute value can also be taken on the individual terms. The issue of including the background contributions remains unadressed here. Equation (6.13) in general violates gauge invariance when including NLO EW corrections but is the most practical alternative nowadays.

The partial decay width of the Higgs boson into a generic massless two-particle final state F at mass q, $\Gamma_{H\to F}(q)$, can be written as [154]

$$\Gamma_{H\to F}(q) = \frac{1}{2q} \int \frac{\mathrm{d}\Omega}{32\pi^2} \left| \mathcal{M}_{\text{decay}}(q^2) \right|^2 = \frac{1}{2q} \int \mathrm{d}\Phi_{\text{decay}} \left| \mathcal{M}_{\text{decay}}(q^2) \right|^2 . \tag{6.14}$$

By defining the branching ratio of the Higgs boson into a specific final state F,

$$BR_{H\to F}(q) = \frac{\Gamma_{H\to F}(q)}{\Gamma_H(q)}, \tag{6.15}$$

we can rewrite the full cross section of Equation (6.13),

$$\sigma_{\text{full}} = \int \mathrm{d}\Phi_{\text{prod}} \frac{\mathrm{d}q^2}{2\pi} \left|\mathcal{M}_{\text{prod}}(q^2)\right|^2 \frac{2q\,\Gamma_H(q)}{(q^2-m^2)^2+m^2\Gamma^2}\, BR_{H\to F}(q), \tag{6.16}$$

The total width of the Higgs boson, $\Gamma_H(q)$, has to be evaluated at the mass q.

Stripping off the branching ratio, we define the off-shell production cross section as

$$\sigma_{\text{prod}}(q) = \int \mathrm{d}\Phi_{\text{prod}} \frac{\mathrm{d}q^2}{2\pi} \left|\mathcal{M}_{\text{prod}}(q^2)\right|^2 \frac{2q\,\Gamma_H(q)}{(q^2-m^2)^2+m^2\Gamma^2}, \tag{6.17}$$

where the q dependence on the one hand indicates that the branching ratio has to be evaluated at the scale q instead of the on-shell Higgs mass m_H when multiplying it with the production cross section. On the other hand, the production cross section takes the full propagator including off-shell effects into account.

Until now the mass of the Higgs boson m and the total width Γ entering in the propagator have not been specified. In the CPS the width and mass of the Higgs boson in the propagator are derived as complex poles $s_{H,\text{CPS}}$ from the inverse Dyson-resummed propagator, satisfying

$$s_{H,\text{CPS}} - M_H^2 - \Sigma_{HH}(s_{H,\text{CPS}}, M_t^2, M_H^2, M_W^2, M_Z^2) = 0, \tag{6.18}$$

where the M_i are renormalized masses and Σ_{HH} is the renormalized Higgs self-energy. The solution is then parametrized according to

$$s_{H,\text{CPS}} = m_{H,\text{CPS}}^2 - i\,\Gamma_{H,\text{CPS}}\, m_{H,\text{CPS}}, \tag{6.19}$$

where the mass $m_{H,\text{CPS}}$ is an input parameter and the width $\Gamma_{H,\text{CPS}}$ can be computed from Equation (6.18) but is not the on-shell width.

As already mentioned, the CPS has been implemented in the POWHEG-BOX for Higgs production via gluon fusion [187] and via VBF [120]. There also exists a version of VBFNLO dedicated to the Higgs Cross Section Working group which can calculate cross sections for Higgs production via VBF according to the CPS [188]. In Table 6.1 we summarize the changes when going from the standard VBFNLO implementation to the CPS for the signal process Hjj without subsequent decay and with the decay including the full information of the decay matrix element, $(H \to VV)jj$. The main difference between the standard procedure and the CPS in VBFNLO for Hjj, besides the different width and mass in the propagator, is the definition of the branching ratio. In the CPS, $BR(q)$ is evaluated at the mass q of the Higgs boson, whereas in the standard definition the branching ratio is taken at the fixed Higgs mass $BR(m_H)$. Therefore the numerator in the definition of the production cross section has to contain the corresponding parameters evaluated at the fixed Higgs mass. After combining the production cross section with the suitable definition

process	σ_{prod}	BR
Hjj CPS	$\int \mathrm{d}\Phi_{\text{prod}} \frac{\mathrm{d}q^2}{2\pi} \left\lvert\mathcal{M}_{\text{prod}}(q^2)\right\rvert^2 \frac{2q\,\Gamma_H(q)}{(q^2 - m^2_{H,\text{CPS}})^2 + m^2_{H,\text{CPS}}\Gamma^2_{H,\text{CPS}}}$	$\int \mathrm{d}\Phi_{\text{decay}} \frac{\lvert\mathcal{M}_{\text{decay}}(q^2)\rvert^2}{64\pi^2\, q\,\Gamma_H(q)}$
Hjj standard	$\int \mathrm{d}\Phi_{\text{prod}} \frac{\mathrm{d}q^2}{2\pi} \left\lvert\mathcal{M}_{\text{prod}}(q^2)\right\rvert^2 \frac{2m_H\,\Gamma_H(m_H)}{(q^2 - m^2_H)^2 + m^2_H\Gamma^2_H(m_H)}$	$\int \mathrm{d}\Phi_{\text{decay}} \frac{\lvert\mathcal{M}_{\text{decay}}(m^2_H)\rvert^2}{64\pi^2\, m_H\,\Gamma_H(m_H)}$
$(H \to VV)jj$ CPS	$\int \mathrm{d}\Phi_{\text{prod}} \frac{\mathrm{d}q^2}{2\pi} \mathrm{d}\Phi_{\text{decay}} \left\lvert\mathcal{M}_{\text{prod}}(q^2)\right\rvert^2 \frac{1}{(q^2 - m^2_{H,\text{CPS}})^2 + m^2_{H,\text{CPS}}\Gamma^2_{H,\text{CPS}}} \left\lvert\mathcal{M}_{\text{decay}}(q^2)\right\rvert^2$	
$(H \to VV)jj$ standard	$\int \mathrm{d}\Phi_{\text{prod}} \frac{\mathrm{d}q^2}{2\pi} \mathrm{d}\Phi_{\text{decay}} \left\lvert\mathcal{M}_{\text{prod}}(q^2)\right\rvert^2 \frac{1}{(q^2 - m^2_H)^2 + m^2_H\Gamma^2_H(m_H)} \left\lvert\mathcal{M}_{\text{decay}}(q^2)\right\rvert^2$	

Table 6.1.: Comparison of the standard VBFNLO prescription and the CPS for the Higgs boson production cross section without a subsequent decay and including the decay into two vector bosons (which can decay further). Interference effects are not included. The parameters m_H and $\Gamma_H(x)$ denote the on-shell mass and the width, calculated at the Higgs mass x. The CPS parameters $m_{H,\text{CPS}}$ and $\Gamma_{H,\text{CPS}}$ are defined in Equations (6.18)–(6.19), q is the off-shell invariant mass of the produced Higgs boson.

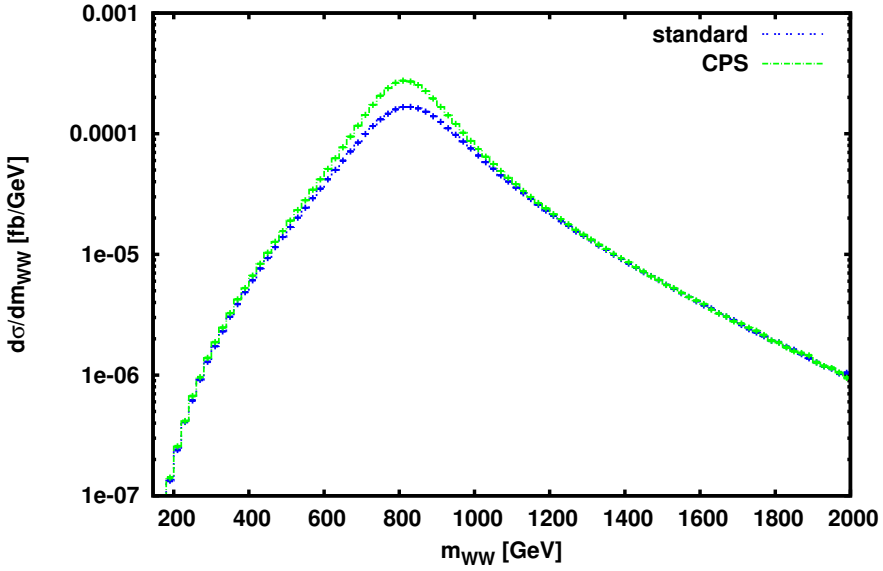

Figure 6.8.: Invariant WW mass for $(H \to WW)jj$ production via VBF for $m_H = 800$ GeV, using the standard procedure (blue) and the CPS (green). The plots have been obtained using VBFNLO.

of the branching ratio the two predictions will differ due to the used parameters in the Higgs propagator and the different mass value at which the branching ratio is evaluated.

In Figure 6.8 we display the invariant $e^+\nu_e\,\mu^-\bar{\nu}_\mu$ mass for $(H \to WW)jj$ production via VBF using the CPS propagator and the standard propagator definition as described in Table 6.1 for $m_H = m_{H,\mathrm{CPS}} = 800$ GeV. The difference of the two curves is solely caused by the different widths in the propagator, $\Gamma_{H,\mathrm{CPS}} = 235.6$ GeV and $\Gamma_H = 304.0$ GeV, and is roughly at the order of 30% ($\sigma_{\mathrm{CPS}} = 83.81$ ab, $\sigma_{\mathrm{standard}} = 62.01$ ab).

6.3.3. Implementation in Repolo

The cross section for the signal including interference effects for VBF Higgs production is given in Equation (6.12). In the Powheg-Box, the signal process is Hjj production using the CPS, but without any interference effects. To account for them we developed the Repolo framework further to reweight events of the signal process for a large Higgs mass m_H. These events have to be reweighted by a factor

$$\frac{|\mathcal{M}_B + \mathcal{M}_H(m_H)|^2 - |\mathcal{M}_B + \mathcal{M}_H(m_h)|^2}{|\mathcal{M}_H^{\mathrm{CPS}}(m_{H,\mathrm{CPS}})|^2}. \tag{6.20}$$

Here we have introduced the short hand notation

$$\left|\mathcal{M}_H^{\mathrm{CPS}}(m_{H,\mathrm{CPS}})\right|^2 = \left|\mathcal{M}_{\mathrm{prod}}(q^2)\right|^2 \frac{1}{(q^2 - m_{H,\mathrm{CPS}}^2)^2 + m_{H,\mathrm{CPS}}^2\Gamma_{H,\mathrm{CPS}}^2} \left|\mathcal{M}_{\mathrm{decay}}(q^2)\right|^2, \tag{6.21}$$

where the propagator contains the CPS parameters and the decay matrix element is calculated at the invariant mass q of the produced Higgs boson. The subtraction of the background is done using the full matrix elements,

$$\mathcal{M}_B + \mathcal{M}_H(m_{H/h}) = \mathcal{M}_{p_i p_j \to 4l}\left(q^2, \frac{1}{q^2 - m^2_{H/h} + i m_{H/h}\Gamma_{H/h}(m_{H/h})}\right). \tag{6.22}$$

The arguments of the matrix element $\mathcal{M}_{p_i p_j \to 4l}$ indicate that the full propagator evaluated with the on-shell Higgs masses and widths are used and that all correlations and off-shell effects from the incoming partons $p_{i,j}$ to the leptonic final state $4l$ are taken into account. The decay matrix element in Equation (6.21) has been included to cancel the dependence of the numerator of Equation (6.20) on the used decay.

Since the CPS scheme has to be used to reweight the POWHEG-BOX events, the mentioned Higgs Cross Section Working Group version of VBFNLO [188] has been exploited as the general framework to build REPOLO. Compared to the BSM version, REPOLO has had to be slightly changed to calculate all three squared matrix elements needed for the reweighting in Equation (6.20). Some additional input parameters have to be set and are explained in Appendix A. The read-in routine for the original LHE file stays unaltered. In the POWHEG LHE file only the invariant mass and the four-momentum of the heavy Higgs boson is recorded. On the contrary, the numerator of Equation (6.20) is only defined for the four-lepton final state, since the continuum diagrams included in Equation (6.22) contain only the momenta of the decay products. Therefore we simulate the full decay by taking into account full spin correlations and off-shell effects using a roulette wheel selection with 1000 random samples per event.

In the heavy Higgs running mode REPOLO needs to evaluate three different matrix elements. First, the signal $\left|\mathcal{M}_H^{\text{CPS}}(m_H)\right|^2$ is calculated using the CPS prescription and the heavy Higgs mass. The results are stored in `rew_s.dat`. Afterwards, the matrix elements contributing to the full process for the heavy Higgs boson, including all background and interference terms are calculated and stored in `rew_sbi.dat`. For the background only we again evaluate the matrix elements contributing to the full $\sigma_{S+B+I}(m_h)$ process, but with a Higgs boson mass of $m_h = 120$ GeV. The results for the matrix elements squared are stored in the file `rew_b.dat`. Afterwards, a `perl` script is used to assign the new weight of Equation (6.20) to the original events.

6.3.4. Results

In this section we apply REPOLO to reweight POWHEG-BOX events generated for VBF Higgs production, where the CPS prescription is used. We show results for two different Higgs masses, $m_H = 500$ GeV and $m_H = 800$ GeV.

In Figure 6.9 we display the invariant WW mass distribution for the input POWHEG-BOX events using the CPS and for the reweighted events obtained with REPOLO for a heavy Higgs boson with $m_H = 500$ GeV. For comparison, we have also plotted the curves obtained with VBFNLO using the definition of the signal process including the interference contributions according to Equation (6.12) with NLO accuracy. The reweighted

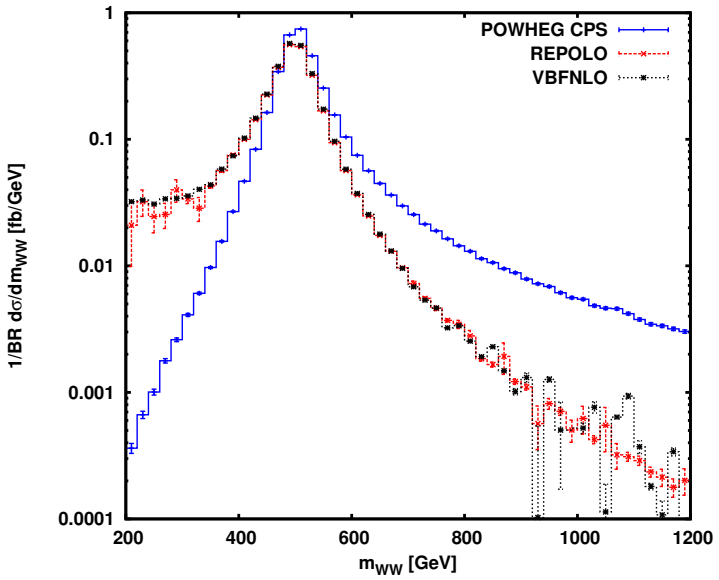

Figure 6.9.: Invariant WW mass for the original CPS POWHEG-BOX sample (blue), for the reweighted events obtained with REPOLO (red) and for the signal including the interference contributions defined in Equation (6.12) obtained with VBFNLO (black) for a Higgs mass of $m_H = 500$ GeV.

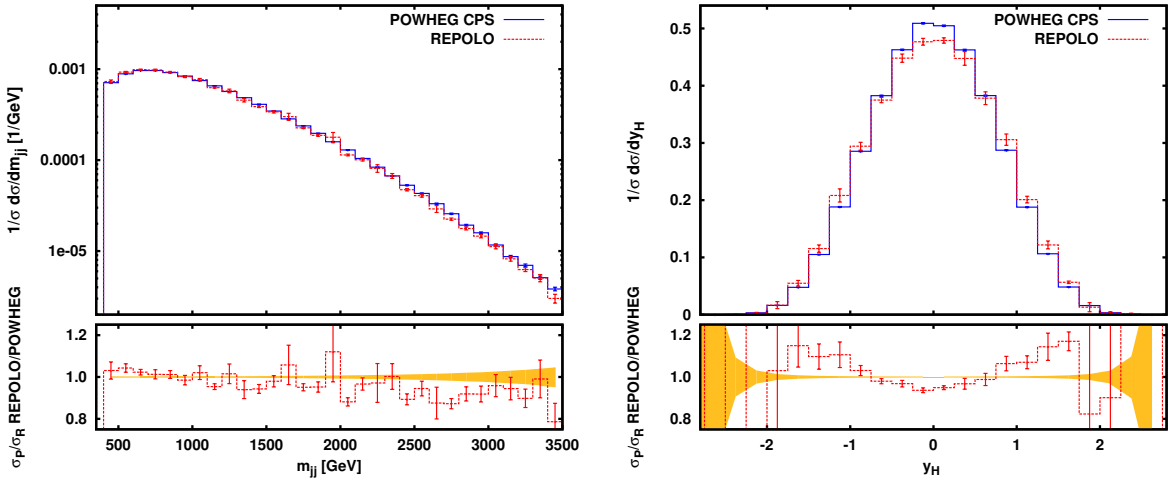

Figure 6.10.: Invariant tagging jet mass (left) and rapidity of the heavy Higgs boson (right) for the original CPS POWHEG-BOX sample (blue) and for the reweighted events obtained with REPOLO (red), both normalized to their respective cross section. The lower panel shows the ratio between the original and the reweighted distribution, again normalized.

distributions have been obtained using 2.5 million unweighted input events, where the decay $H \to WW \to 2l2\nu$ has been simulated with two different sets of random numbers to improve statistics. For the shown distributions we have used no cuts on the leptons and neutrinos, whereas VBF cuts for the jets are demanded ($p_{T,j} > 20$ GeV, $|y_j| < 4.5$, $R_{jj} = 0.5$, $m_{jj}^{\text{tag}} > 400$ GeV, $\Delta y_{jj}^{\text{tag}} > 4$). The cross sections are

$$\sigma_S^{\text{Powheg-Box}} = 72.09 \pm 0.05 \text{ fb} \quad \text{and} \quad \sigma_{S+I}^{\text{Repolo}} = 63.09 \pm 0.48 \text{ fb}. \tag{6.23}$$

For the Vbfnlo curve, which is calculated at NLO accuracy, we have divided out the branching ratio for the decay at the appropriate scale, $BR_{H\to WW\to 2l2\nu}(q)$. As for the BSM case, the reweighted curve shows statistical fluctuations in the low-m_{WW} region since the reweighting factors are of the order of 100 and only a small number of Powheg-Box events is present in this region. However, the agreement between Vbfnlo and Repolo is very satisfying. At the high-m_{WW} tale, the Repolo prediction is even better than the Vbfnlo one since the reweighting factor is of the order of 0.1 or lower and therefore many events can be used for the reweighting. For Vbfnlo statistics are worse since the contribution in this area of phase space is inferior compared to the lower m_{WW} region. In addition, the NLO accuracy of the original Powheg-Box LHEs seems to be preserved, although the interference effects do not factorize at individual phase-space points. However the effects coming from α_s cancel in the ratio defined in Equation (6.20).

With the reweighted Repolo events it is now possible to study the influence of the interference terms on other distributions. As an example we plot the invariant tagging jet mass and the rapidity of the Higgs boson for the original Powheg-Box events and for the reweighted ones at the LHE level in Figure 6.10. All distributions and the ratio are normalized to the respective cross section specified in Equation (6.23). The distributions of the jets exhibit only mild dependence on the interference effects, despite the different normalization caused by the smaller cross section. The two tagging jets are slightly closer in rapidity and are produced more centrally. Interference effects are more prominent in the distributions of the Higgs boson, its rapidity distribution gets broader. Likewise, the transverse momentum of the Higgs boson is shifted to slightly lower values.

In Figure 6.11 we give an example for the different decay modes that can be simulated with Repolo for a Higgs boson mass of $m_H = 800$ GeV. The plot shows the invariant Higgs boson mass for the original Powheg-Box events (blue) and for the reweighted curves using the decays $H \to WW \to 2l2\nu$ (red), $H \to ZZ \to 2l2\nu$ (green) and $H \to ZZ \to 4l$ (yellow). The black Vbfnlo distribution has been obtained at NLO accuracy using the full $pp \to 2l2\nu\, jj$ process. The background contribution again has been removed according to Equation (6.12) with a Higgs boson mass of $m_h = 120$ GeV. For all distributions we have required very inclusive cuts ($p_{T,j} > 10$ GeV, $|y_j| < 4.5$, $m_{jj}^{\text{tag}} > 10$ GeV and $R_{jj} > 0.8$). For the reweighted distributions we have used 950.000 Powheg-Box events as input. Not only is the agreement between the three different decay options very good within the statistical errors, but also the Vbfnlo distribution is nicely reproduced. Again, the fluctuations at low $m_{WW/ZZ}$ are very large since only a handful of events get a very large reweighting factor.

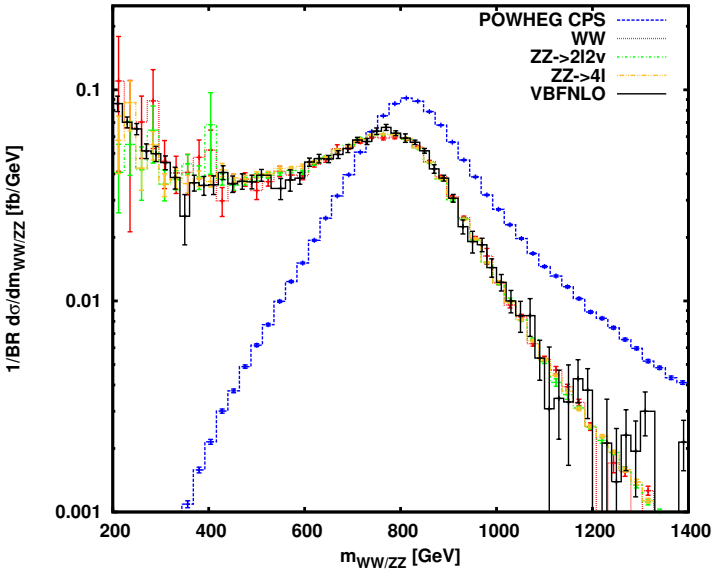

Figure 6.11.: Differential distribution of the invariant Higgs mass. The blue curve show the distribution at the LHE level for the POWHEG-BOX input events. The other colored distributions are obtained with REPOLO using the three different options to simulate the Higgs decay, $H \to WW \to 2l2\nu$ (red), $H \to ZZ \to 2l2\nu$ (green) and $H \to ZZ \to 4l$ (yellow). The black curve is obtained using VBFNLO with NLO accuracy ($e^+\nu_e\,\mu^-\bar{\nu}_\mu\,jj$ production).

6.4. Conclusions

We have introduced the REPOLO framework, which is able to reweight LHE files to account for two different BSM scenarios and for interference effects in heavy Higgs boson searches. It is an add-on to VBFNLO and uses the matrix elements implemented there to assign a new weight to each event in LHE input files. Meanwhile, all VBF Higgs boson production modes with non-hadronic decays are available.

We have checked the REPOLO method by reweighting NLO POWHEG-BOX events to account for anomalous HVV vertices and have used LO VBFNLO events including the decay of the Higgs boson into two photons to verify the predictions for a spin-2 model (see Equation (6.2)).[4] Additionally, POWHEG-BOX events for heavy Higgs bosons with the CPS prescription have been reweighted to include additional interference effects. We have shown that NLO accuracy of POWHEG-BOX events is preserved during the reweighting procedure since the effects related to the factorization or renormalization scale cancel out. The method is, however, limited by statistics since individual points with a large reweighting factor can effectively destroy distributions.

The heavy Higgs version of REPOLO has already been used by the ATLAS Collaboration [168].

[4] Taking NLO events for the spin-2 option is also possible.

CHAPTER 7

HIGGS BOSON PRODUCTION VIA VECTOR-BOSON FUSION IN ASSOCIATION WITH THREE JETS

After this intermezzo on reweighting of Les Houches event files we now come back to the shower corrections to the sub-leading jets in Higgs production via vector-boson fusion (VBF). To this end we have matched Higgs production via VBF in association with three jets at NLO accuracy to parton showers within the POWHEG-BOX [21–23] framework. The work presented in this chapter has been done in collaboration with Barbara Jäger.

7.1. Introduction

To establish the true nature of the resonance found at the LHC [19, 20], it is essential to precisely determine its couplings to fermions and gauge bosons [189–191]. Such coupling measurements can make use of the rather clean environment of VBF Higgs production, where the color-singlet exchange in the t-channel leads to tagging jets widely separated in rapidity with little hadronic activity in between. In order to suppress QCD backgrounds, a central-jet veto (CJV) [100–104] can be applied, which prohibits hard jets in the rapidity gap between the two tagging jets. To efficiently use such a veto it is however necessary to precisely simulate the jet activity in the central region of the detector.

As we have seen in Section 3.2 (Figure 3.4), acting with parton showers on VBF Higgs events produced at LO accuracy and comparing the outcome for the third-hardest jet with the LO prediction for $Hjjj$ production via VBF yields differences that can be of the order of 100-200%. This is a consequence of the fact that a parton shower is only reliable for soft/collinear radiation. In order to accurately describe the full spectrum additional QCD radiation has to be included via matrix elements. Matching the NLO prediction of Hjj production via VBF using the implementation into the POWHEG-BOX as described in Chapter 5 to PYTHIA [27] and HERWIG++ [28, 29], however, still leads to predictions for the third-hardest jet which deviate roughly 20% from the fixed-order result. Moreover,

as we have seen in Section 5.5 (Figure 5.5, left panel), the corrections of the two parton showers behave oppositely.

Therefore it is mandatory to precisely determine the third-hardest jet, which can be done by studying the process $pp \to Hjjj$. The NLO corrections to the VBF induced process have been calculated first in Ref. [192, 193]. This calculation, which neglects some kinematically and color-suppressed contributions, is available in VBFNLO [24–26] and forms the basis of our implementation of $Hjjj$ production via VBF in the POWHEG-BOX. More recently, full NLO QCD corrections to electroweak $Hjjj$ production have been presented in Ref. [194].

In this chapter we present the matching of $Hjjj$ production via VBF at NLO QCD to parton showers within the POWHEG-BOX framework. In Section 7.2 we will discuss the technical details of the implementation and the used approximations. Unfortunately, the NLO cross section obtained with VBFNLO and our new POWHEG-BOX implementation show a discrepancy of roughly 3%. Since the deviations are reasonably flat in phase space they should however only affect the overall normalization of the showered result. The numerical results presented in Section 7.3 are therefore normalized to the total cross section and should hence be valid even after including parton shower corrections.

7.2. Elements of the Implementation

The implementation of $Hjjj$ production via VBF in the context of the POWHEG-BOX requires, as major building blocks, the matrix elements for all relevant partonic subprocesses at Born level and at NLO. These have first been calculated in [192, 193] and are available within VBFNLO. As in the case of the processes described in Chapters 4–5 we have extracted the matrix elements from VBFNLO and adapted them to the format required by the POWHEG-BOX (see Section 7.2.1). Additionally, the phase-space integration is more involved than in the processes studied so far since there are several IR-divergent Born contributions. We will review the most important aspects of the phase-space implementation in Section 7.2.2. As has already been mentioned before, there are slight discrepancies between the NLO result of VBFNLO and our implementation. We will elaborate on them in Section 7.2.3.

7.2.1. Matrix Elements and used Approximations

7.2.1.1. Tree-Level Diagrams and Virtual Corrections

At leading order, processes of the type $qq' \to qq'gH$ and all channels obtained by crossing have to be taken into account. Sample diagrams where the gluon is attached to the upper quark line are depicted in Figure 7.1. All diagrams with an electroweak gauge boson exchanged in the s-channel, which form a gauge invariant subset of diagrams, are considered as part of the Higgs-strahlung process and excluded here, since interference effects are negligible when imposing typical VBF cuts [69, 131]. Additionally, the interference of t-channel with u-channel diagrams in subprocesses with same-type quarks is neglected. Throughout, we assume a diagonal CKM matrix and neglect all quark masses.

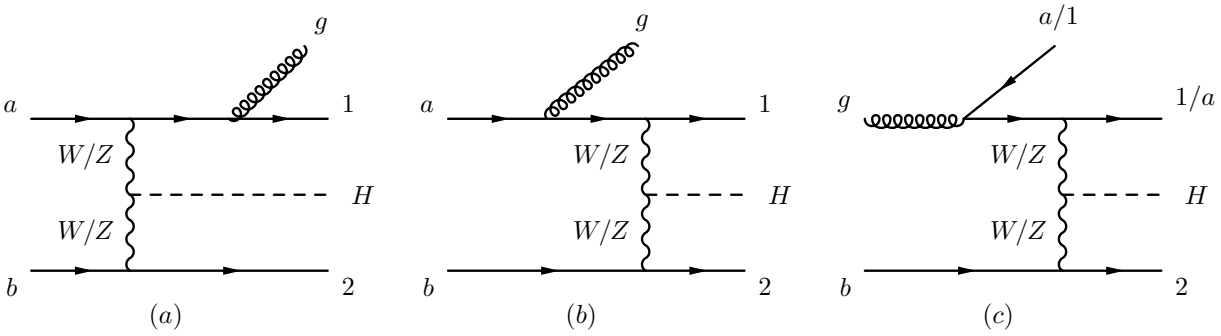

Figure 7.1.: Sample diagrams for the Born contributions to VBF $Hjjj$ production with gluon emission from the upper quark line.

Since we exclude contributions from b quarks, we will consequently use the four-flavor scheme. We refer to the electroweak $Hjjj$ production process at order $\mathcal{O}(\alpha_s\alpha^3)$ within these approximations as "VBF $Hjjj$ production".

The Born matrix elements comprise two different color structures that do not interfere. Building the color- and spin-averaged sum for final-state gluon emission, they read [192]

$$\begin{aligned} |\mathcal{M}_B|^2 &= \overline{\sum_{\text{colors}}} \left| t^a_{i_1 i_a} \delta_{i_2 i_b} \mathcal{A}_{3,1a} + t^a_{i_2 i_b} \delta_{i_1 i_a} \mathcal{A}_{3,2b} \right|^2 \\ &= C_F \left(|\mathcal{A}_{3,1a}|^2 + |\mathcal{A}_{3,2b}|^2 \right) \\ &= |\mathcal{M}_{1a}|^2 + |\mathcal{M}_{2b}|^2 \,. \end{aligned} \tag{7.1}$$

The color-stripped matrix elements $\mathcal{A}_{3,1a}$ and $\mathcal{A}_{3,2b}$ indicate whether the gluon is emitted from the upper ($1a$) or lower ($2b$) quark line. The squared matrix elements including color factors with gluon emission at the upper (lower) quark line are denoted $|\mathcal{M}_{1a}|^2$ ($|\mathcal{M}_{2b}|^2$). For initial-state gluons, only one of the two color sub-amplitudes contributes since we only consider VBF and neglect Higgs-strahlung contributions.

Possible virtual corrections to the Born diagram (a) from Figure 7.1 are depicted in Figure 7.2. They comprise up to four-point functions, where the virtual corrections only affect one quark line, and additional pentagon and hexagon contributions where a gluon connects the upper and lower quark line. As discussed in Ref. [192], the latter contributions are color suppressed and additionally only contribute for diagrams with two initial quarks when the Higgs-strahlung diagrams are omitted. Therefore we neglect all pentagon and hexagon contributions, which has also consequences for the real emission and FKS subtraction terms, as the pentagons and hexagons comprise $1/\epsilon$-poles due to soft divergences. Therefore, the corresponding terms leading to exactly these soft singularities have to be omitted in the real and FKS subtraction contributions. We will discuss this issue below.

The color-stripped interference term of the Born and virtual matrix elements, where both gluons are emitted from the upper quark line, taking into account up to box diagrams, in

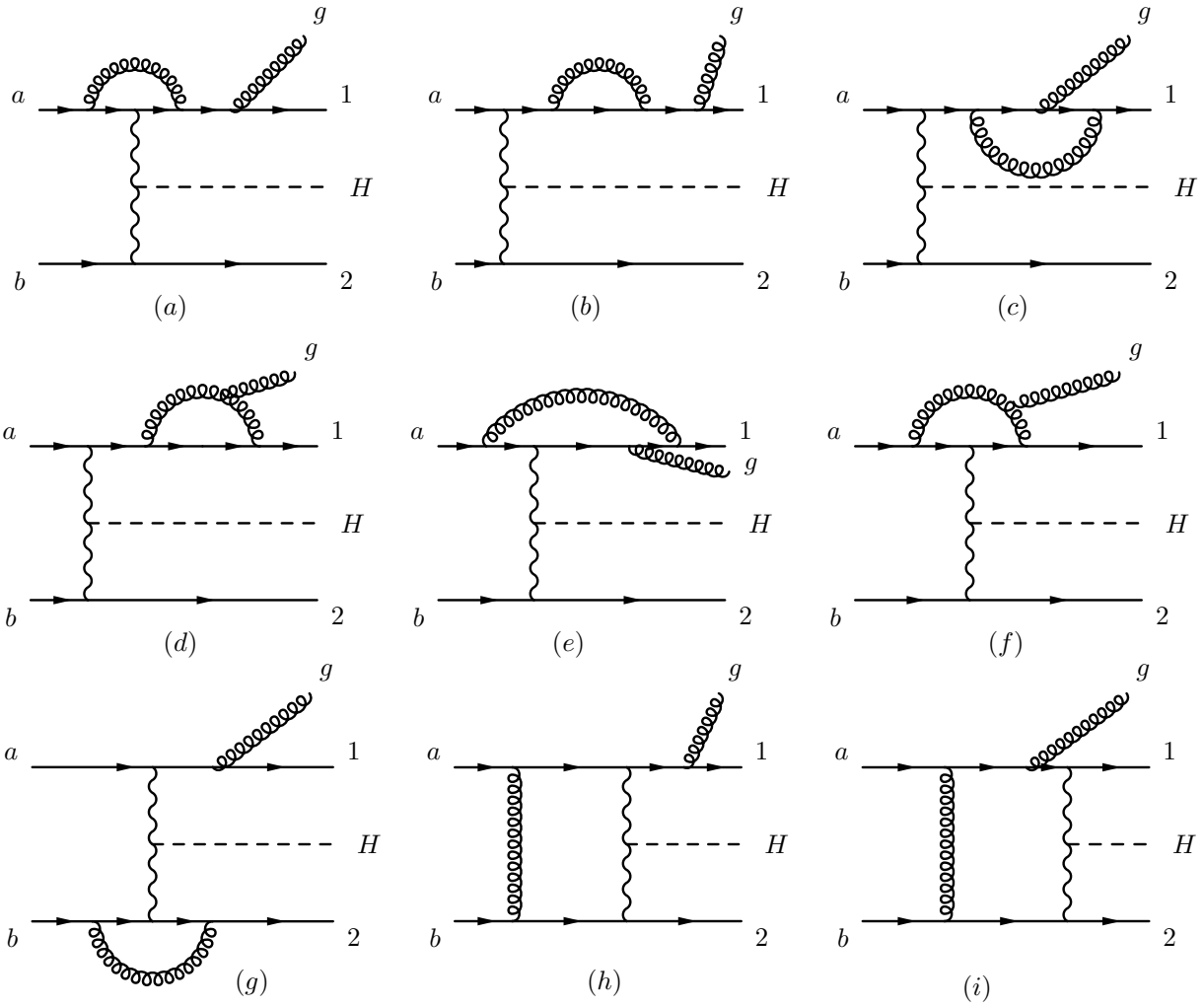

Figure 7.2.: Possible virtual corrections to VBF $Hjjj$ production with a final-state gluon emitted from the upper quark line. The diagrams (a)-(g) show up to box corrections which only affect one quark line. Pentagon and hexagon contributions (like (h) and (i)) are not included in our approximation.

this approximation read

$$\begin{aligned}\overline{\sum_{\text{colors}}} 2\ \mathrm{Re}[\mathcal{A}^{\text{virt}}_{3,1a}\mathcal{A}^{*}_{3,1a}] \;=\; & |\mathcal{A}_{3,1a}|^2 \frac{\alpha_s(\mu_R^2)}{2\pi}\frac{(4\pi)^\epsilon}{\Gamma(1+\epsilon)}\left(\frac{\mu_R^2}{Q^2}\right)^\epsilon \\ & \Bigg\{ \frac{1}{\epsilon^2}\Big(-C_A-4C_F\Big) \\ & + \frac{1}{\epsilon}\left(-\gamma_g-4\gamma_q-C_A\left[\ln\left(\frac{Q^2}{s_{13}}\right)+\ln\left(\frac{Q^2}{s_{a3}}\right)-\ln\left(\frac{Q^2}{s_{a1}}\right)\right]\right. \\ & \qquad \left. -2C_F\left[\ln\left(\frac{Q^2}{s_{a1}}\right)+\ln\left(\frac{Q^2}{s_{b2}}\right)\right]\right) \\ & + C_F\left[-\ln^2\left(\frac{Q^2}{s_{b2}}\right)-3\ln\left(\frac{Q^2}{s_{b2}}\right)-16\right]-\frac{\pi^2}{6}C_A\Bigg\} \\ & +\ 2\ \mathrm{Re}\left[\widetilde{\mathcal{A}}^{\text{virt}}_{3,1a}\,\mathcal{A}^{*}_{3,1a}\right]. \end{aligned} \tag{7.2}$$

Here, $\widetilde{\mathcal{A}}^{\text{virt}}_{3,1a}$ denotes the color-stripped finite part of the loop diagrams. Note that for this result the POWHEG-BOX convention, see Equations (3.36)–(3.38), has been adopted. The color factors of the partons are given by

$$\begin{aligned} C_F &= \frac{N_c^2-1}{2N_c}, & C_A &= N_c, \\ \gamma_q &= \frac{3}{2}C_F, & \gamma_g &= \frac{11}{6}C_A-\frac{2}{3}T_R n_f, \end{aligned} \tag{7.3}$$

where the number of colors is $N_c = 3$. As stated before we work in the four-flavor scheme, hence $n_f = 4$, and $T_R = \frac{1}{2}$ is fixed by convention. The invariants s_{ij} are given by

$$s_{ij} = 2\,p_i\cdot p_j,\ \ i,j = a,b,1,2,3. \tag{7.4}$$

The indices of the four-momenta correspond to the labels of the partons in Figure 7.2, a, b are the incoming quarks, $1, 2$ the outgoing ones and p_3 denotes the momentum of the gluon. The invariants s_{ij} are always time-like. All other terms given in Equation (2.29) of Ref. [192] cancel when imposing the POWHEG-BOX convention $Q = \mu_R$ and are therefore not given here.[5]

The two gauge invariant subsets of pentagon and hexagon corrections (see Figure 7.1 (h) and (i)) again decompose into two different color structures [193],

$$\mathcal{M}_{\text{ph}} = t^a_{i_1 j}t^b_{j i_a}t^b_{i_2 i_b}\mathcal{A}^{\text{ph}}_{3,1a} + t^a_{i_2 j}t^b_{j i_b}t^b_{i_1 i_a}\mathcal{A}^{\text{ph}}_{3,2b}, \tag{7.5}$$

where $\mathcal{A}^{\text{ph}}_{3,1a}$ ($\mathcal{A}^{\text{ph}}_{3,2b}$) denotes the color-stripped matrix element where the final-state gluon is emitted from the upper (lower) quark line. The interference term with the Born corresponding matrix element, which we will neglect later on, is then given by

$$2\,\mathrm{Re}\left[\mathcal{M}_B\mathcal{M}^{*}_{\text{ph}}\right] = \frac{C_F}{N_c^2-1}\left[2\,\mathrm{Re}\left[\mathcal{A}_{3,1a}\,\mathcal{A}^{\text{ph},*}_{3,2b}\right]+2\,\mathrm{Re}\left[\mathcal{A}_{3,2b}\,\mathcal{A}^{\text{ph},*}_{3,1a}\right]\right]. \tag{7.6}$$

[5] Note the typo in the third line of Equation (2.29) of Ref. [192], s_{23} has to be replaced by s_{13}.

These contributions are color suppressed and, as discussed in Ref. [192], further suppressed kinematically when imposing typical VBF cuts. However, they include $1/\epsilon$-poles which, in the soft limit, are proportional to the interference of a Born matrix elements with a gluon emitted from the upper quark line and a tree-level diagram with gluon emission from the lower quark line,

$$2\,\mathrm{Re}\left[\mathcal{A}_{3,1a}\,\mathcal{A}^*_{3,2b}\right]. \tag{7.7}$$

Since the POWHEG-BOX generates the subtraction terms automatically from the flavor structures of the Born and real subprocesses, FKS subtraction terms for the divergent contributions proportional to the term given in Equation (7.7) would be included.

Excluding contributions of the type (7.7) from the subtraction terms is equivalent to neglecting color correlations between the upper and lower quark line. The color-correlated Born amplitudes within this approximation have been calculated using Equation (3.31) and have been checked against an explicit calculation of the expression given in Equation (3.30) using FORM [195, 196]. They read

$$\begin{aligned}
\mathcal{B}_{2b} &= C_F\,|\mathcal{M}_{1a}|^2 + \left(C_F - \frac{C_A}{2}\right)|\mathcal{M}_{2b}|^2\,,\\
\mathcal{B}_{1g} &= \frac{C_A}{2}\,|\mathcal{M}_{1a}|^2\,,\\
\mathcal{B}_{2g} &= \frac{C_A}{2}\,|\mathcal{M}_{2b}|^2\,,\\
\mathcal{B}_{1a} &= \left(C_F - \frac{C_A}{2}\right)|\mathcal{M}_{1a}|^2 + C_F\,|\mathcal{M}_{2b}|^2\,,
\end{aligned} \tag{7.8}$$

for final-state gluons. For Born contributions with initial-state gluons only one of the two squared amplitudes, $|\mathcal{M}_{1a}|^2$ or $|\mathcal{M}_{2b}|^2$, contributes (the partons are labeled according to Figure 7.1). Using Equation (3.36), it has also been checked that these color-correlated amplitudes reproduce the correct $1/\epsilon$-poles in Equation (7.2). The spin-correlated Born matrix elements, which are needed for the subtraction of collinear divergencies, are calculated according to Equation (3.33), where again terms of the form (7.7) have been omitted.

7.2.1.2. Real Emission Contributions

The real emission contributions contain two different structures: processes involving two gluons, $qq' \to qq'\,gg\,H$, and pure quark-scattering diagrams, $qq' \to qq'\,Q\bar{Q}'\,H$, and all processes obtained by crossing.

In Figure 7.3 we show sample diagrams for the case of two final state gluons. The color-stripped matrix elements $\mathcal{A}^{1a}_{43}$ include two gluons emitted from the upper quark line, $\mathcal{A}^{1a}_{34}$ can be obtained by interchanging two gluons. The matrix elements where one gluon is emitted from the upper and one gluon from the lower quark line are denoted $\mathcal{B}^3_4$ and $\mathcal{B}^4_3$. The matrix element for two final-state gluons is then given by [192]

$$\begin{aligned}
\mathcal{M}^{(\mathrm{fs})}_4 &= \left(t^{a_4}t^{a_3}\right)_{i_1 i_a}\delta_{i_2 i_b}\mathcal{A}^{1a}_{43} + \left(t^{a_3}t^{a_4}\right)_{i_1 i_a}\delta_{i_2 i_b}\mathcal{A}^{1a}_{34}\\
&+ \left(t^{a_4}t^{a_3}\right)_{i_2 i_b}\delta_{i_1 i_a}\mathcal{A}^{2b}_{43} + \left(t^{a_3}t^{a_4}\right)_{i_2 i_b}\delta_{i_1 i_a}\mathcal{A}^{2b}_{34}\\
&+ t^{a_3}_{i_1 i_a}t^{a_4}_{i_2 i_b}\mathcal{B}^3_4 + t^{a_4}_{i_1 i_a}t^{a_3}_{i_2 i_b}\mathcal{B}^4_3.
\end{aligned} \tag{7.9}$$

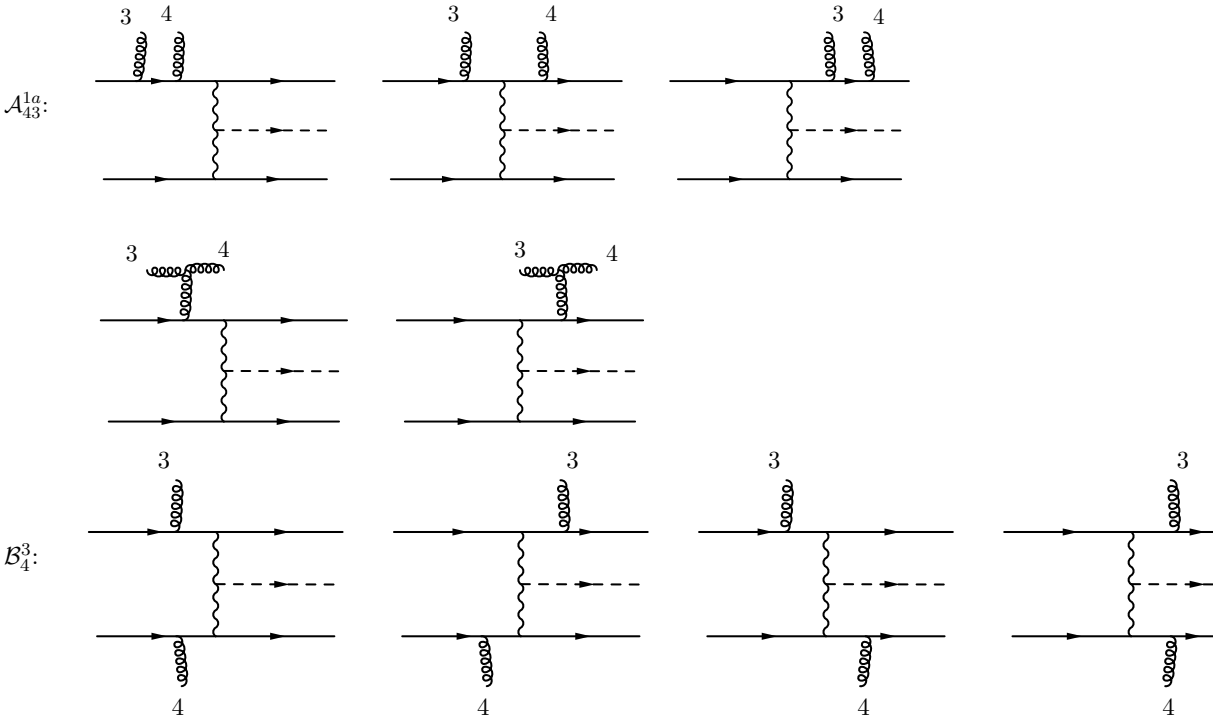

Figure 7.3.: Sample diagrams for two out of six possible color structures that contribute to the subprocess $qq' \to qq'\, gg\, H$. Two other structures can be obtained by interchanging two gluons. Diagrams where both gluons couple to the lower quark line form the two remaining color structures.

Squaring this matrix element leads to three different types of contributions,

$$\begin{aligned} |\mathcal{M}_4^{(\mathrm{fs})}|^2 &= N_c^2 C_F^2 \Big\{ \left(|\mathcal{A}_{43}^{1a}|^2 + |\mathcal{A}_{34}^{1a}|^2 + |\mathcal{A}_{43}^{2b}|^2 + |\mathcal{A}_{34}^{2b}|^2 + |\mathcal{B}_4^3|^2 + |\mathcal{B}_3^4|^2\right) \\ &+ \frac{C_F - 1/2\, C_A}{C_F}\, 2\,\mathrm{Re}\left[\mathcal{A}_{43}^{1a}\mathcal{A}_{34}^{1a\,*} + \mathcal{A}_{43}^{2b}\mathcal{A}_{34}^{2b\,*}\right] \\ &+ \frac{1}{N_c^2 - 1} 2\,\mathrm{Re}\left[\left(\mathcal{A}_{43}^{1a} + \mathcal{A}_{34}^{1a}\right)\cdot\left(\mathcal{A}_{43}^{2b} + \mathcal{A}_{34}^{2b}\right)^* + \mathcal{B}_4^3\mathcal{B}_3^{4\,*}\right] \Big\}. \end{aligned} \tag{7.10}$$

Since we have neglected the pentagon and hexagon corrections and also the corresponding local FKS subtraction terms, the real-emission contributions that contain the same color structures as the neglected terms have to be disregarded as well. These contributions are interference terms where both gluons couple to different quark lines. They are written in the last line of Equation (7.10).

Compared to the original VBFNLO routines, slight changes have been made to match the POWHEG-BOX convention. The original code for the real-emission diagrams is based on automatically generated MADGRAPH [197, 198] routines, where s-channel diagrams involving a hadronical decay of an electroweak vector boson, $V \to q\bar{q}$, are disregarded while running the program. Which diagrams have to be vetoed is decided due to the flavor structure of the considered subprocess. This method works also in the POWHEG-BOX for

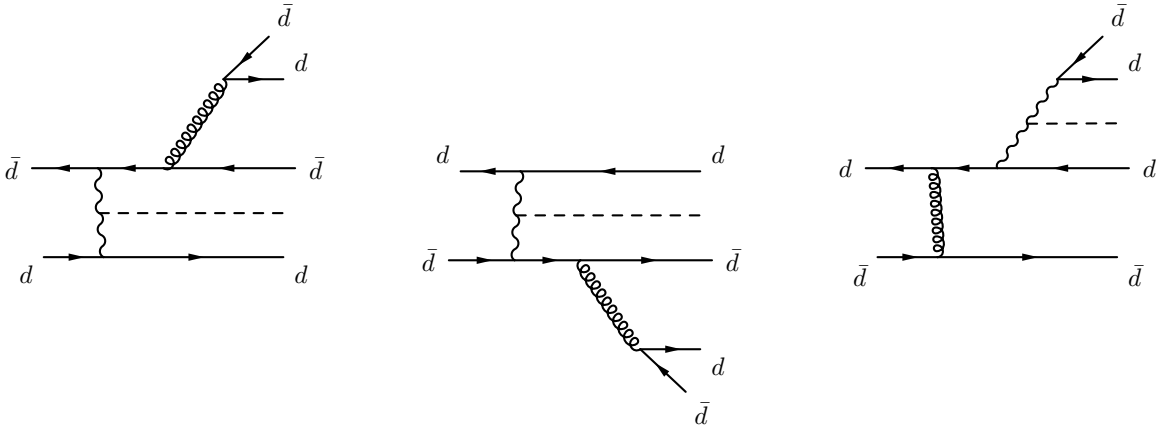

Figure 7.4.: Feynman diagrams for the three different color structures that contribute to the $qq' \to qq' Q\bar{Q}' H$ subprocess, the right diagram is not included in our approximations and has to be vetoed.

subprocesses with final-state gluons. For processes of the type $qq' \to qq' Q\bar{Q} H$, one has to know which pair of quarks emerges from the decay of the gluon. In our notation the pair is denoted $Q\bar{Q}$. In the MadGraph code, three different color structures as depicted in Figure 7.4 contribute. The rightmost diagram is not included in our approximation for $Hjjj$ production via VBF and therefore has to be vetoed. To this end, we again use the tagging of the parton lines as described in Section 4.2.1 and assign a different tag to the two partons coming from the gluon decay. Accordingly, we only calculate the diagrams where the gluon and not an electroweak gauge boson decays into a quark anti-quark pair. This tagging is especially useful for crossed processes like $Qq \to Qq\, q'\bar{q}' H$.

7.2.2. Phase Space

In contrast to Hjj production via VBF, which is finite at LO even without jet definition cuts, $Hjjj$ production via VBF comprises several IR divergences at tree level. The gluon can lead to soft divergences and a pair of partons can become collinear. To avoid these singularities one can impose generation cuts but has to make sure that the obtained results are independent of these cuts. Another possibility, which has already been used in Vjj production via VBF and Hjj production via VBF with anomalous couplings, is a Born suppression factor as described in Section 4.2.3. We have implemented two different variants for the suppression factor. The first possibility is given by

$$F_1\left(\Phi_n\right) = \prod_{i=1}^{3} \left(\frac{p_{T,j_i}^2}{p_{T,j_i}^2 + \Lambda_j^2} \right)^2 \prod_{i=1}^{3} \left(\frac{m_{ij}^2}{m_{ij}^2 + \Lambda_m^2} \right)^2 , \tag{7.11}$$

where the product contains all final state partons, p_{T,j_i} denotes the transverse momentum of the ith parton and $m_{ij}^2 = 2\, p_i \cdot p_j$. This factor suppresses all soft and collinear

divergences. Another possible choice has been adapted from Ref. [199] and is given by

$$\begin{aligned} F_2 &= S_1 \cdot S_2, \\ S_1 &= \exp\left[-\Lambda_1^4 \cdot \left(\sum_{i=1}^{3} \frac{1}{p_{T,j_i}^4} + \sum_{i=1}^{3} \frac{1}{q_{ij}^2}\right)\right], \\ S_2 &= \left(\frac{H_T^2}{H_T^2 + \Lambda_2^2}\right)^2, \end{aligned} \tag{7.12}$$

with

$$q_{ij} = p_i \cdot p_j \, \frac{E_i \, E_j}{E_i^2 + E_j^2} \quad \text{and} \quad H_T = p_{T,j_1} + p_{T,j_2} + p_{T,j_3}. \tag{7.13}$$

The factor S_1 suppresses all soft and collinear regions, S_2 suits to generate more events with moderate transverse momentum.

The phase-space generator itself has been built using the phase-space generator for VBF Hjj production as implemented in the POWHEG-BOX [120]. The additional emission needed at tree level for $Hjjj$ production is generated using emission kinematics provided automatically by the POWHEG-BOX. This method has already been used for Hjj production [200] and three jet production [199].

7.2.3. Comparisons and Checks

The amplitudes for the Born and real-emission contributions have been checked phase-space point by phase-space point against the original VBFNLO code and against automatically generated MADGRAPH [170, 197, 198] amplitudes, which have been adapted to match the approximations used in this calculation. Very good agreement between 11 and 15 digit accuracy has been found. Additionally, the parts of the virtual amplitudes that do not depend on the respective convention and subtraction scheme have been checked and agree at the amplitude level. Moreover, cross sections and differential distributions at LO for $Hjjj$ and $Hjjjj$ production via VBF agree perfectly between VBFNLO and our new implementation in the POWHEG-BOX.

However, as has been mentioned before, the full NLO cross section differs between our new implementation and VBFNLO. The discrepancy is of the order of 3% and no clear scale dependence (μ_R, μ_F) or analysis cut dependence is visible. Since the subtraction in VBFNLO and the POWHEG-BOX is done differently, VBFNLO uses Catani-Seymour subtraction [92, 93], the POWHEG-BOX FKS subtraction [98, 99], it is not possible to compare the subtraction terms and the virtual amplitude separately. Due to the different conventions some terms are shifted from the virtual to the subtraction terms and vice versa. Therefore it has unfortunately not been possible to trace the difference between the two implementations further down. The subtraction works for both codes. The integration error within VBFNLO drops only for very high statistics. A comparison with the results obtained in Ref. [194] is not possible neither, since they include Higgs-strahlung diagrams and only give cross sections with very inclusive cuts.

However, as shown in Figures 7.5–7.6, the deviation of the NLO prediction of VBFNLO and our new implementation in the POWHEG-BOX is rather flat in phase space. The plots

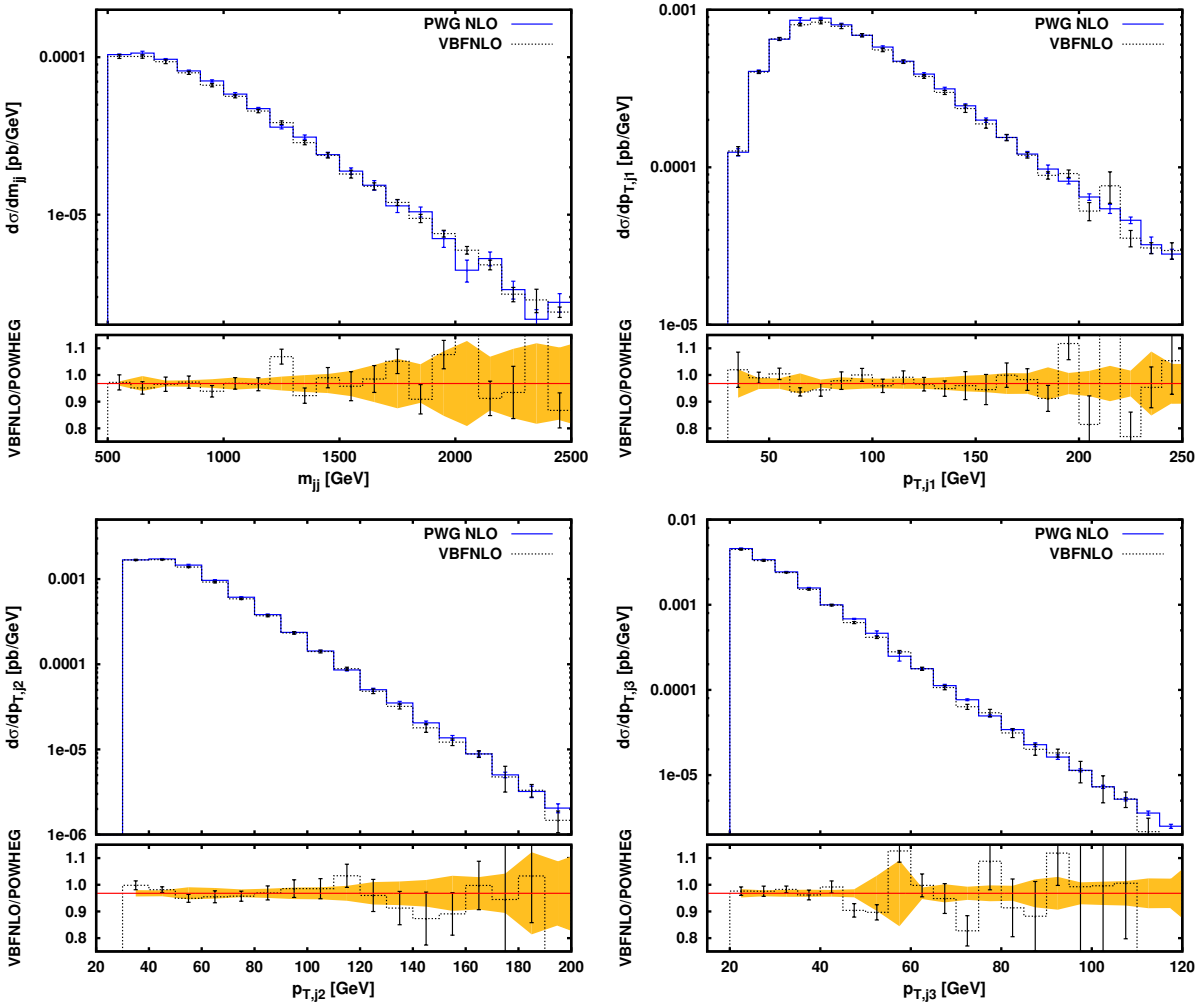

Figure 7.5.: Comparison of various differential jet distributions at NLO between VBFNLO and our new POWHEG-BOX implementation. The ratio plot shows the slight discrepancy between the two predictions. The yellow error band indicates the statistical error of the POWHEG-BOX result, its central value has been shifted to the red line at 0.968 (see text). The black error bars correspond to the statistical error of VBFNLO. The cuts used are specified in Equations (7.15)–(7.18).

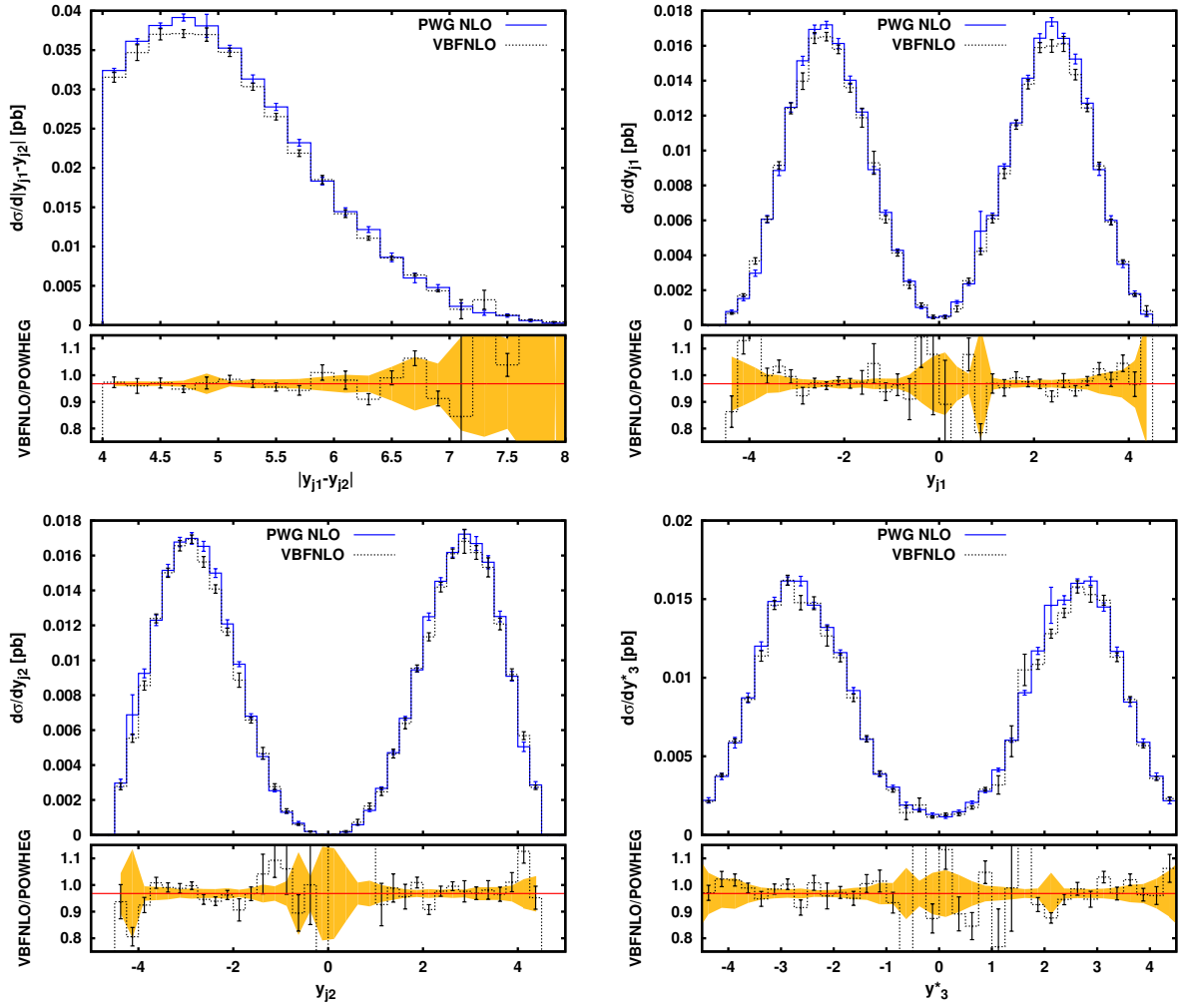

Figure 7.6.: Comparison of the differential rapidity distributions of the three leading jets at NLO between VBFNLO and our new POWHEG-BOX implementation. The ratio plot shows the slight discrepancy between the two predictions. The yellow error band indicates the statistical error of the POWHEG-BOX result, its central value has been shifted to the red line at 0.968 (see text). The black error bars correspond to the statistical error of VBFNLO. The cuts used are specified in Equations (7.15)–(7.18).

display the invariant tagging-jet mass and the transverse momenta of the three leading jets as well as the absolute value of the rapidity difference between the two tagging jets, the rapidity of the two tagging jets and the location of the third-hardest jet relative to the two tagging jets (see Equation (7.20)). The lower panel of each plot shows the ratio of the VBFNLO and the POWHEG-BOX curves. The yellow band displays the statistical error of our new implementation. It has been shifted to the ratio of the two cross sections, $\sigma_{\text{VBFNLO}}/\sigma_{\text{POWHEG}} = 0.968$, which is indicated by the red line. The black error bars correspond to the statistical error of the VBFNLO prediction. As can be nicely seen in the ratio plot, the deviation of the two predictions is, within statistical fluctuations, flat in phase space.

The hardest emission within the POWHEG framework is generated according to

$$\begin{aligned} \mathrm{d}\sigma_{\text{PWG}} = \bar{B}\left(\Phi_n\right)\mathrm{d}\Phi_n \Big\{ & \Delta_{\text{PWG}}\left(\Phi_n, p_T^{\text{min}}\right) \\ & + \Delta_{\text{PWG}}\left(\Phi_n, k_T\right) \frac{R\left(\Phi_n, \Phi_{\text{rad}}\right)}{B\left(\Phi_n\right)} \Theta\left(k_T - p_T^{\text{min}}\right) \mathrm{d}\Phi_{\text{rad}} \Big\}, \end{aligned} \tag{7.14}$$

see Equation (3.22). The POWHEG Sudakov factor is defined in Equation (3.25) and only depends on the ratio of the respective real emission and Born matrix element squared. The $\bar{B}$ function corresponds to the NLO cross section with fixed underlying Born kinematics. Since the Born and real-emission matrix elements and cross sections agree between VBFNLO and the new POWHEG-BOX implementation and the $\bar{B}$ function, i.e. the NLO distributions, seems to differ by a constant factor, only the overall normalization of the $\bar{B}$ function should be affected by the discrepancy. Therefore we will divide out the total cross section in the following discussion. Since parton shower effects do not depend on the normalization, the shown results should be valid even after providing the correct normalization.

To find the origin of the discrepancy and the validation of one of the two codes is left for future work.

7.3. Phenomenological Results

In this section we give numerical results for VBF $Hjjj$ production obtained using our new implementation in the POWHEG-BOX. The Higgs boson, with mass $M_H = 126$ GeV and width $\Gamma_H = 4.095$ MeV, is produced in proton-proton collisions at the LHC with a center-of-mass energy of 8 TeV. We are using the `CT10nlo - fixed 4-flavor` PDF set [124] as implemented in the LHAPDF library [125] and the corresponding value of the strong coupling, $\alpha_s(M_Z) = 0.1127$. Partons are clustered into jets via the anti-k_T algorithm [126] using the FASTJET package [127, 128] with a resolution parameter of $R = 0.5$. The electroweak parameters are calculated via tree-level relations from the weak gauge-boson masses, $M_W = 80.398$ GeV and $M_Z = 91.1876$ GeV, and the Fermi constant, $G_F = 1.16637 \cdot 10^{-5}$ GeV^{-2}. The widths of the massive gauge bosons are calculated thereof to $\Gamma_W = 2.095$ GeV and $\Gamma_Z = 2.506$ GeV, respectively. The renormalization and factorization scales are $\mu_R = \mu_F = M_H/2$, unless explicitly stated otherwise.

We demand at least three well observable jets with a minimum transverse momentum of

$$p_{T,j} > 20 \text{ GeV}, \tag{7.15}$$

as well as a rapidity bounded by

$$|y_j| < 4.5. \tag{7.16}$$

The two hardest jets, called tagging jets, are required to additionally satisfy

$$p_{T,j}^{\text{tag}} > 30 \text{ GeV}. \tag{7.17}$$

Since our approximations for Higgs boson production via VBF in association with three jets are only valid when imposing typical VBF cuts, we demand

$$m_{jj}^{\text{tag}} > 500 \text{ GeV}, \quad \Delta y_{jj}^{\text{tag}} > 4 \quad \text{and} \quad y_{j1}^{\text{tag}} \times y_{j2}^{\text{tag}} < 0. \tag{7.18}$$

The kinematics of the Higgs boson is not restricted.

As before, we will interface the NLO calculation to three different parton showers, Pythia version 6.4.25 with the Perugia 0-tune (Feb 2009) [27], the angular-ordered shower and the p_T-ordered Dipole Shower (DS++), both implemented in Herwig++ version 2.7.0 [28–32]. As has already been explained before, additional wide-angle, soft radiation is missing in the standard angular-ordered Herwig++ shower. We estimate the effect of this additional soft radiation from the comparison of Herwig++ with the p_T-ordered DS++. As before, we include parton shower effects, but neither hadronisation nor effects from underlying event simulations.

For the plots shown in the following we have used a generation cut of $p_{T,\text{parton}} > 10$ GeV for the three partons present in the Born process and in addition, $m_{ij}^2 = 2\, p_i \cdot p_j > (5 \text{ GeV})^2$ for all three possible combinations is required. Additionally, we have used the Born suppression factor F_1 as defined in Equation (7.11) with the parameters $\Lambda_m = 10$ GeV and $\Lambda_p = 0$. This has been necessary to generate enough events in the phase-space region defined by Equations (7.15)–(7.18). The cross sections at fixed order and after including parton shower corrections are

$$\begin{aligned} \sigma_{\text{NLO}} &= 73.35 \pm 0.19 \text{ fb}, & \sigma_{\text{Pythia}} &= 66.28 \pm 0.43 \text{ fb}, \\ \sigma_{\text{Herwig++}} &= 69.60 \pm 0.45 \text{ fb}, & \sigma_{\text{DS++}} &= 70.05 \pm 0.46 \text{ fb}. \end{aligned} \tag{7.19}$$

As explained in Section 7.2.3, we will only show normalized distributions in order to not depend on the possibly wrong normalization.

As has been stated before, it has to be ensured that the Born generation cut does not influence the final results. Therefore we have generated a sample of events using the Born suppression factor F_1 as defined in Equation (7.11) with the parameters $\Lambda_m = 10$ GeV and $\Lambda_p = 10$ GeV and only mild generation cuts of $p_{T,\text{parton}} > 2$ GeV and $m_{ij} > (2 \text{ GeV})^2$. The comparison of the two samples after showering with Herwig++ are displayed in Figure 7.7 for the rapidity of the third-hardest jet with respect to the two tagging jets (left) and the transverse momentum of the fourth-hardest jet (right), where the cut has been

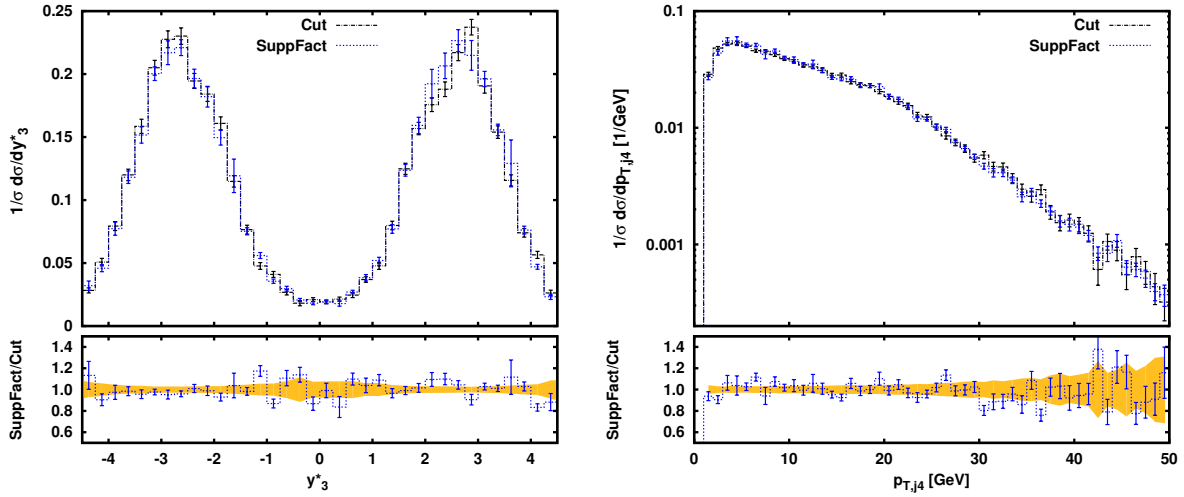

Figure 7.7.: Comparison of two event samples using a Born suppression factor (blue) and generation cuts (black) after showering with HERWIG++, the details are explained in the text.

lowered to $p_{T,j_4} > 1$ GeV. We observe no sizable deviations within statistical fluctuations and therefore conclude that the used generation cut has no apparent influence on the results.

In Figure 7.8 we show the normalized distributions of the invariant tagging jet mass and the transverse momentum of the Higgs boson at fixed NLO, calculated using our new POWHEG-BOX implementation, and matched with the three parton showers PYTHIA, HERWIG++ and DS++. As can best be seen in the ratio plots, which display the respective parton shower effects, the NLO prediction is essentially unaltered when including additional radiation. On account of the unitary of the parton showers only the normalization, which is factored out here, changes due to the migration of some events which do not pass the cuts after the showering stage. This is the same observation as for Vjj and Hjj production via VBF, see Chapters 4 and 5.

The effect of the parton showers on the distributions of the three hardest jets, which are now all taken into account at NLO accuracy, is mostly insignificant. To justify this statement we plot the normalized differential distribution of the transverse momentum and of the rapidity of the two tagging jets and the first sub-leading jet in Figure 7.9. As for Higgs production in association with two jets (Chapter 5), the tagging jet distributions do not receive noticeable parton shower corrections.

Taking the POWHEG prediction for $Hjjj$ production via VBF as starting point for the parton showers, this observation now also applies partly to the third-hardest jet, see the two distributions in the lower panel of Figure 7.9. The predictions at NLO and the ones obtained with the two HERWIG++ showers are in good agreement. However, for the rapidity of the third-hardest jet, deviations between the prediction of PYTHIA and the two HERWIG++ showers are visible. PYTHIA predicts more jets in the central region of the detector compared to the NLO, HERWIG++ and DS++ distributions. As we have seen

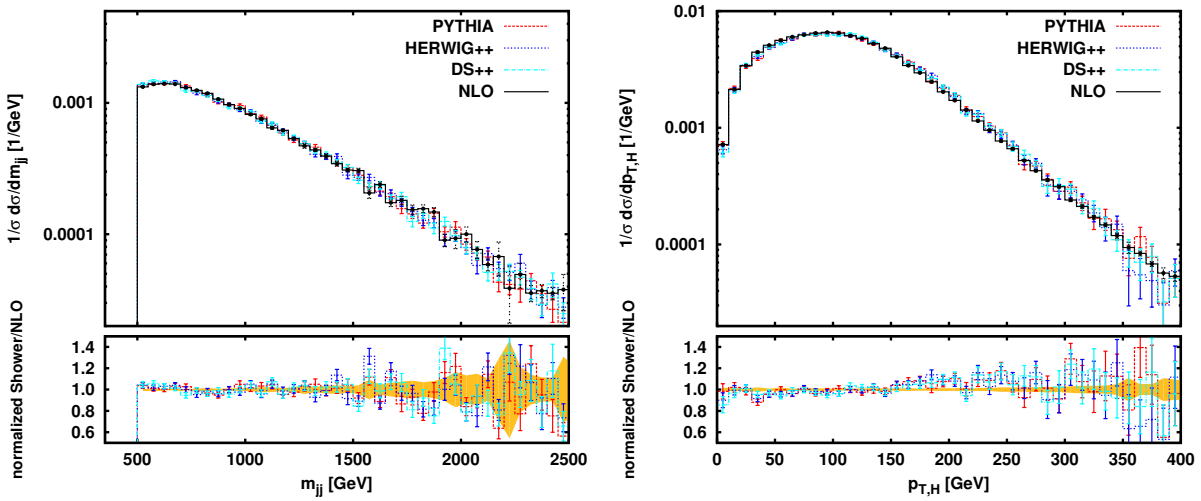

Figure 7.8.: Differential distribution of the invariant tagging jet mass and the transverse momentum of the Higgs boson, normalized to the respective cross section in Equation (7.19). The NLO curve (black) has been obtained using our new POWHEG-BOX implementation, the three colored lines correspond to the NLO prediction matched with PYTHIA (red), HERWIG++ (blue) and DS++ (turquoise). In the ratio plot the shower effects are displayed. The yellow error band corresponds to the statistical uncertainty of the NLO prediction. In the ratio plot, the normalization of the various curve has been included.

in Chapter 4 for electroweak gauge boson production via VBF, PYTHIA has predicted more jets in the rapidity gap between the two tagging jets due to uncorrelated, soft radiation. On the contrary, the two HERWIG++ showers predominantly have radiated additional partons in the collinear region between the two tagging jets and the beam axis. This effect, which has also been observed for VBF Higgs production in Chapter 5 (see Figure 5.5), now almost vanishes for the two HERWIG++ showers when considering the first sub-leading jet, which has now formal NLO accuracy. The predictions obtained with PYTHIA still show deviations from the fixed order result which will be discussed below in more detail.

In the top panel Figure 7.10 we show the location of the third-hardest jet relative to the tagging jets,

$$y_3^* = y_{j_3} - \frac{y_{j_1} + y_{j_2}}{2}. \tag{7.20}$$

Compared to the VBF Hjj case (Figure 5.5), the agreement between the showered and the fixed-order distribution of y_3^* is improved for HERWIG++ and DS++, whereas PYTHIA still predicts more jets in the rapidity gap than the NLO calculation. The deviations of PYTHIA from the fixed order result account for roughly 10-20% and are hence of the same order of magnitude as in the VBF Hjj case. In addition, the differential distribution of the PYTHIA prediction for y_3^* in Hjj and $Hjjj$ production via VBF is essentially the same. The difference between the three shower predictions can be further studied by investigating

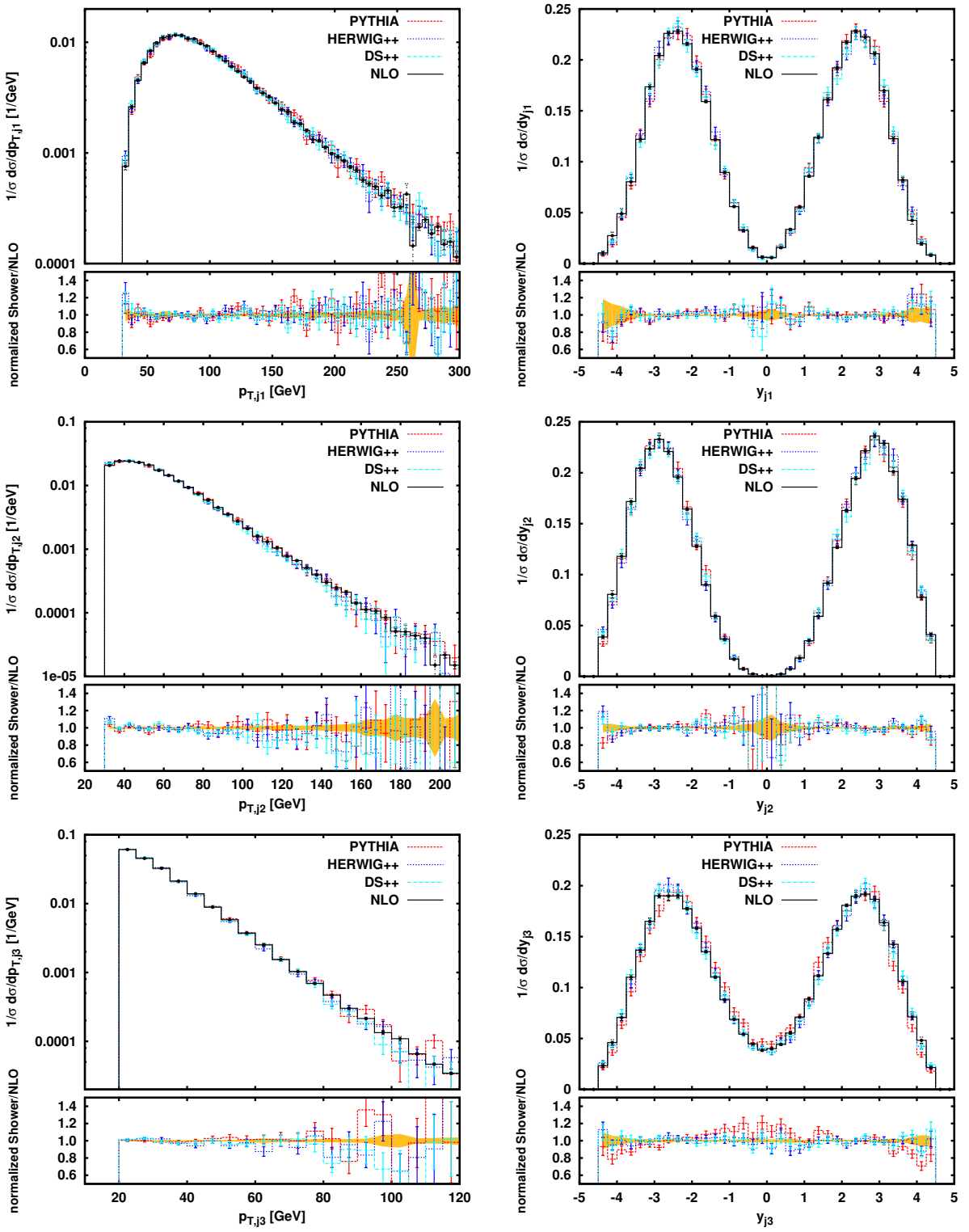

Figure 7.9.: Normalized differential distributions of the transverse momentum and of the rapidity of the three hardest jets in VBF $Hjjj$ production at NLO and showered with Pythia, Herwig++ and DS++. The respective ratio plot shows the influence of the parton showers on the NLO result. The line styles are assigned as in Figure 7.8.

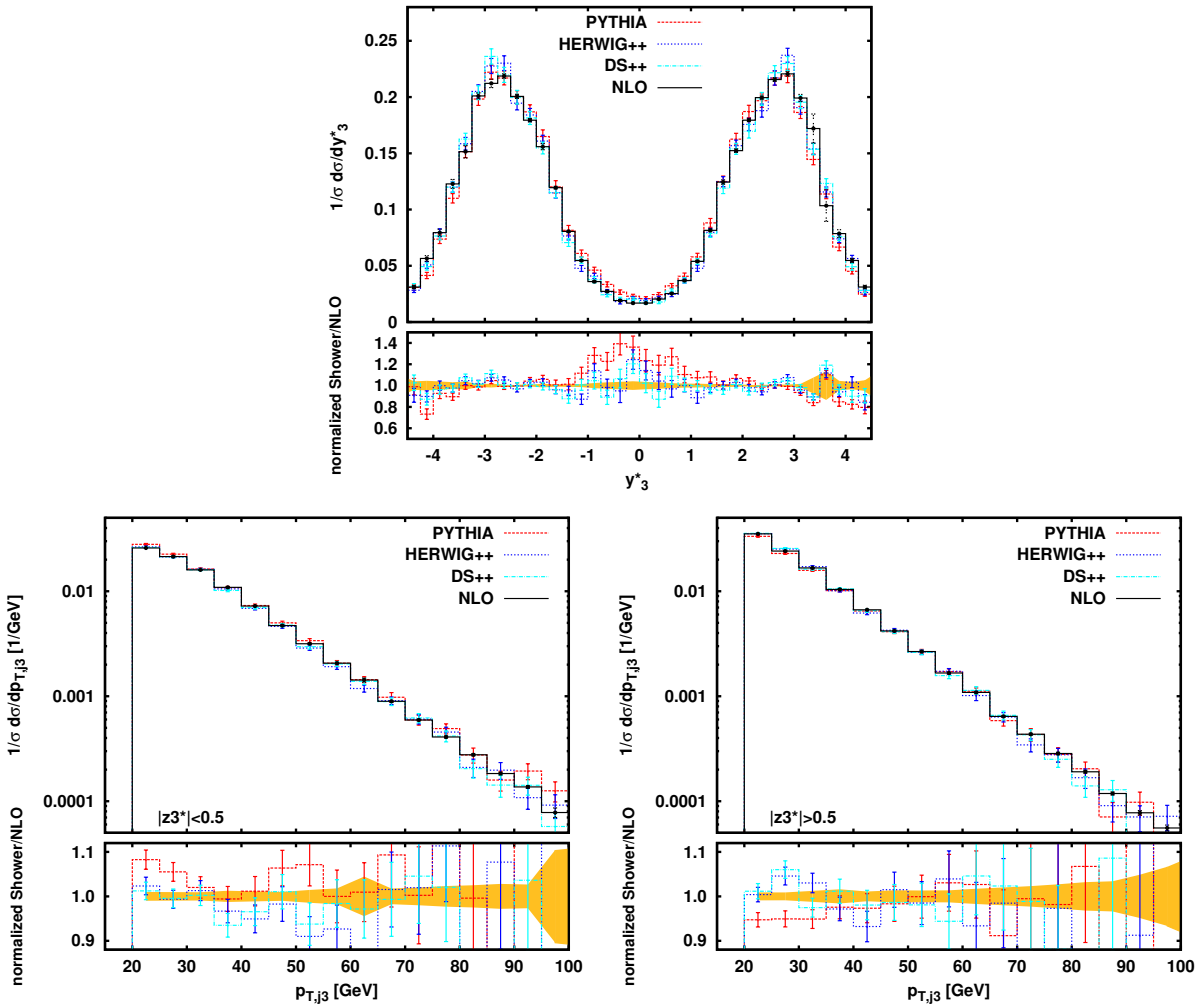

Figure 7.10.: The y_3^* distribution (top) and the transverse momentum of the third-hardest jet in the rapidity gap (bottom left) and between the two tagging jets and the beam axis (bottom right) at NLO and showered with Pythia, Herwig++ and DS++. The line styles are assigned as in Figure 7.8.

the transverse momentum distribution of the third-hardest jet in the rapidity gap and in the region between the beam axis and the two tagging jets (Figure 7.10, lower panels). To split the phase space into these two regions we again exploit the variable

$$z_3^* = \frac{y_3^*}{|y_{j_1} - y_{j_2}|}. \tag{7.21}$$

The two tagging jets are localized at $|z_3^*| = 0.5$, i.e. $|z_3^*| < 0.5$ corresponds to the rapidity gap and $|z_3^*| > 0.5$ to the region between the tagging jets and the beam axis. The Pythia prediction lies slightly above the Herwig++ ones for jets in the rapidity gap (Figure 7.10 left) and slightly below in the region between the tagging jets and the beam axis (Figure 7.10 right), which again can be traced back to the population of the available phase space with soft and collinear radiation. Moreover, the two Herwig++ showers

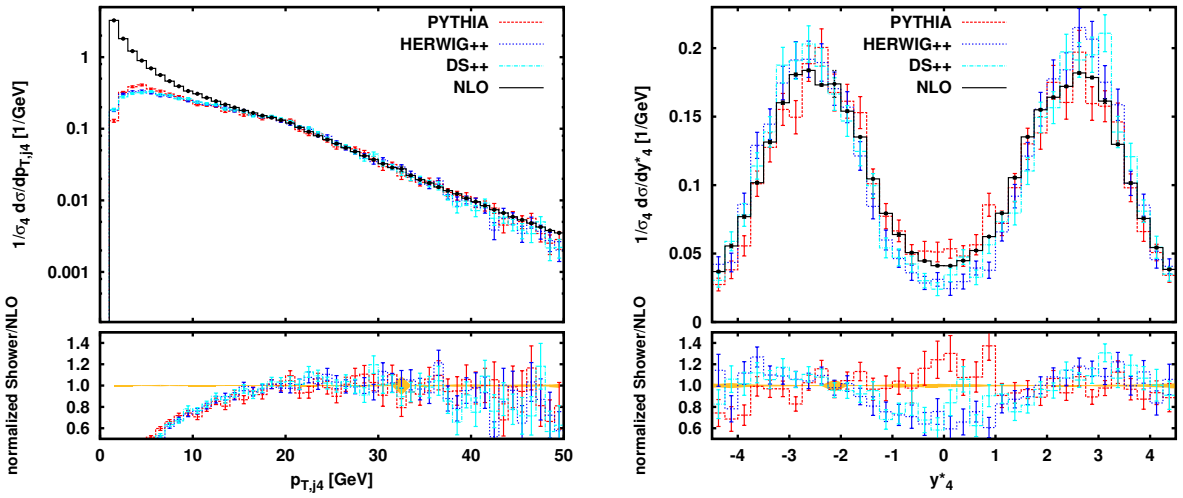

Figure 7.11.: Differential distribution of the transverse momentum (left) and the rapidity of the fourth-hardest jet relative to the two tagging jets as defined in Equation (7.22), both normalized to the Higgs plus four-jet cross section. In the left plot the cut on the transverse momentum of the fourth jet has been lowered to $p_{T,j_4} > 1$ GeV, whereas the standard cuts defined in Equations (7.15)–(7.18) have been kept for the normalization. The line styles are assigned as in Figure 7.8.

are in good agreement and coincide with the NLO prediction.

However, major differences between the three shower predictions become visible, as expected, starting with the distributions of the fourth-hardest jet, since it is only LO accurate and softer than the other three jets. In Figure 7.11 we display the differential distribution of the transverse momentum (left) and of the location of the fourth-hardest jet with respect to the two tagging jets (right), defined as

$$y_4^* = y_{j_4} - \frac{y_{j_1} + y_{j_2}}{2}. \tag{7.22}$$

The distributions are normalized to the Higgs plus four-jet cross section. For the p_{T,j_4} distribution the cut on the transverse momentum has been lowered to $p_{T,j_4} > 1$ GeV, whereas the cross section for the normalization incorporates the cuts specified in Equations (7.15)–(7.18). In the low transverse-momentum region the damping of the POWHEG Sudakov factor becomes manifest, whereas for a moderate transverse momentum of 20-40 GeV the predictions including parton shower effects match the NLO result. For higher transverse momenta the showered distributions fall below the fixed order curve due to additional radiation which is not re-clustered together with the fourth-hardest jet.

The parton shower corrections to the y_4^* distribution again show differences between the PYTHIA and the two HERWIG++ showers. As has already been observed for the distributions of the third-hardest jet in Vjj and Hjj production via VBF, the PYTHIA prediction lies above the NLO curve in the central region between the two tagging jets, whereas the

two HERWIG++ showers produce more additional partons between the two tagging jets and the beam axis which are likely to be reclustered together with the fourth-hardest parton into the fourth hardest jet. Again, predictions of the standard angular-ordered HERWIG++ shower and the p_T-ordered dipole shower DS++ are in good agreement, thus we deduce that also in this case additional soft, wide-angle radiation missing in the angular-ordered shower is negligible.

We have seen that by interfacing $Hjjj$ production via VBF to parton showers within the POWHEG approach, the discrepancy between the PYTHIA, HERWIG++ and DS++ predictions manifest in the distribution of the third-hardest jet in Hjj production via VBF is partly resolved and the two HERWIG++ showers match the NLO prediction. PYTHIA still produces more jets in the central detector region than predicted by the fixed-order calculation. To give a complete description of Higgs production via VBF, the merging of the Hjj and $Hjjj$ calculation and the matching to different parton showers would be desirable, but is beyond the scope of this thesis.

7.4. Conclusion

We have matched Higgs production via VBF in association with three jets, using some approximations for the NLO calculation, to the three parton showers PYTHIA, HERWIG++ and DS++ by exploiting the POWHEG-BOX framework. The NLO calculation is based on matrix elements included in VBFNLO. Unfortunately, the normalization of the NLO cross section of our new implementation and the original VBFNLO code differs by roughly 3%. The validation of one of the two codes is left for future work. However, as this discrepancy is rather flat in phase space, the matching to parton showers is nevertheless possible and should yield the correct results when normalizing the distributions to the total cross section.

We have shown that the shower corrections of HERWIG++ and DS++ to the third-hardest jet are in better agreement with the NLO prediction than for Hjj production via VBF, whereas PYTHIA still predicts more jets in the central detector region. Major differences between the three parton showers appear in the distributions of the fourth-hardest jet, which is only LO accurate. Moreover, since the DS++ and HERWIG++ predictions are in good agreement, we conclude that the effect of wide-angle soft radiation is negligible for the process studied here. To give a more complete description of VBF Higgs production at the LHC, the merging of the Hjj and $Hjjj$ calculation in the VBF approximation and a matching to parton showers at NLO accuracy would be worthwhile, but is beyond the scope of this work.

CHAPTER 8

SUMMARY

In this thesis, several VBF processes available at NLO accuracy within VBFNLO have been matched to the parton shower Monte Carlo generators PYTHIA 6 and HERWIG++ using the POWHEG method as implemented in the POWHEG-BOX. This matching is required to give an accurate description of differential distributions measured at the LHC. VBF is particularly suitable to scrutinize the couplings of the newly discovered boson to SM particles and to study its CP and spin quantum numbers.

The first considered processes have been the production of the electroweak gauge bosons W and Z via VBF. These processes provide the possibility to study the VBF topology and to test the theoretical predictions before moving on the the more involved Higgs boson signal. The parton-shower corrections to the leptonic decay products and to the two hardest (tagging) jets are marginal, whereas the third-hardest jet, whose matrix elements are only LO accurate, is sensible to the parton shower in use and receives corrections up to 30–40%. We have additionally shown that soft, wide-angle radiation missing in the standard HERWIG++ shower has no visible effect on the studied distributions.

The second process, Higgs boson production via VBF, has been studied using anomalous couplings which parametrize BSM physics in a model-independent way, using an effective Lagrangian approach. As discussed, parton-shower corrections are essentially the same for the SM and the studied BSM scenarios. In addition, the distinction of PYTHIA and HERWIG++ in observables related to the third-hardest jet are the same as for W and Z production via VBF and are of the order of 20% for the cuts used. The disparity between the fixed-order result and the PYTHIA, HERWIG++ and DS++ prediction for the rapidity of the third-hardest jet is partly resolved when considering Higgs production via VBF in association with three jets at NLO accuracy. The two HERWIG++ showers and the NLO prediction are in good agreement, whereas PYTHIA still predicts more hard jets in the rapidity gap between the two tagging jets.

In addition, we have discussed the program REPOLO, which uses the VBFNLO framework to reweight SM events supplied by Les Houches event files of VBF Higgs production at

LO or NLO accuracy. REPOLO is capable of reweighting events to account for anomalous couplings of the Higgs boson to SM particles or to replace the Higgs boson by a spin-2 particle. Thereby it provides predictions of differential distributions in these BSM models without the need of a complete recalculation of the process for each scenario. In addition, REPOLO is able to supply signal-background interference effects needed in heavy Higgs boson searches.

APPENDIX A

REPOLO INPUT FILE

In this appendix we specify the main input parameters for REPOLO, set in the `repolo.dat` file.

A.1. Main Input Parameters

- `PROCESS`: Process ID as described in Table A.1 for the BSM option and in Table A.2 for heavy Higgs reweighting.
- `ECM`: The center-of-mass energy, $\sqrt{s}$, of the collider, measured in GeV. The variable should be set to the value used in the Les Houches Event file.
- `INPUT_FILE`: Name of the input Les Houches Event file. Default is `pwgevents.lhe`.
- `ID_MUF` and `ID_MUR`: Choice of the factorization and renormalization scale.

All other options are analogous to the `vbfnlo.dat` input file [24–26] and can also be found in the REPOLO manual [201].

A.2. BSM and heavy Higgs Parameters

REPOLO can reweight Standard Model events either by altering the HVV couplings using effective dimension 5 or 6 operators, or by taking signal-background interference for a heavy Higgs boson into account. The different options can be set as follows:

- `SBI_REW`: Switch for heavy Higgs-reweighting (`true`). If set to `false`, the BSM option is used.
- `HQSQR`: Choice of the q^2 distribution of the heavy Higgs boson used to generate the input events. See Table A.3 for a list of available options. Default is 1.

PROCID	PROCESS	BSM
100	$pp \to H\,jj$	anomalous HVV couplings
101	$pp \to H\,jj \to \gamma\gamma\,jj$	anomalous HVV couplings, spin-2 ID 191
102	$pp \to H\,jj \to \mu^+\mu^-\,jj$	anomalous HVV couplings
103	$pp \to H\,jj \to \tau^+\tau^-\,jj$	anomalous HVV couplings
105	$pp \to H\,jj \to W^+W^-\,jj \to \ell_1^+\nu_{\ell_1}\ell_2^-\bar{\nu}_{\ell_2}\,jj$	anomalous HVV couplings, spin-2 ID 195
106	$pp \to H\,jj \to ZZ\,jj \to \ell_1^+\ell_1^-\ell_2^+\ell_2^-\,jj$	anomalous HVV couplings, spin-2 ID 196
107	$pp \to H\,jj \to ZZ\,jj \to \ell_1^+\ell_1^-\nu_{\ell_2}\bar{\nu}_{\ell_2}\,jj$	anomalous HVV couplings, spin-2 ID 197

Table A.1.: Process IDs for $pp \to Hjj$ production via vector-boson fusion in the SM. Anomalous HVV vertices can be used in every process, the spin-2 option with the respective `ProcID` is only available for $\gamma\gamma$, WW and ZZ decay modes.

- `ANOM_CPL`: If set to `true`, anomalous Higgs boson couplings are used. Anomalous coupling parameters are set via the file `anom_HVV.dat`. Default is `false`.
- `SPIN2`: Option for the spin-2 model. This is available for the process $pp \to S_2jj \to VVjj$ (see Table A.1). Default is set to `false`. Spin-2 parameters are set via the file `spin2coupl.dat`.
- `HMASS`: Higgs boson mass in GeV. Default value is 126 GeV.
- `HWIDTH`: Although REPOLO can calculate the total and partial widths of the Higgs boson, it is also possible to set its width to this input parameter. Default is -999 GeV, which means that the internally calculated value of the width is used. For the heavy Higgs option, the width is set to the value recommended by Higgs Cross Section Working Group [48].

ProcId	105	106	107
Signal	$pp \to H\,jj$ $(\to W^+W^-\,jj$ $\to \ell_1^+\nu_{\ell_1}\ell_2^-\bar{\nu}_{\ell_2}\,jj)$ is simulated	$pp \to H\,jj$ $(\to ZZ\,jj \to$ $\ell_1^+\ell_1^-\ell_2^+\ell_2^-\,jj)$ is simulated	$pp \to H\,jj$ $(\to ZZ\,jj$ $\to \ell_1^+\ell_1^-\nu_{\ell_2}\bar{\nu}_{\ell_2}\,jj)$ is simulated
SBI	$pp \to W^+W^-\,jj \to$ $\ell_1^+\nu_{\ell_1}\ell_2^-\bar{\nu}_{\ell_2}\,jj$	$pp \to ZZ\,jj \to$ $\ell_1^+\ell_1^-\ell_2^+\ell_2^-\,jj$	$pp \to ZZ\,jj \to$ $\ell_1^+\ell_1^-\nu_{\ell_2}\bar{\nu}_{\ell_2}\,jj$
Background	$pp \to W^+W^-\,jj \to$ $\ell_1^+\nu_{\ell_1}\ell_2^-\bar{\nu}_{\ell_2}\,jj$, $m_h = 120$ GeV	$pp \to ZZ\,jj \to$ $\ell_1^+\ell_1^-\ell_2^+\ell_2^-\,jj$, $m_h = 120$ GeV	$pp \to ZZ\,jj \to$ $\ell_1^+\ell_1^-\nu_{\ell_2}\bar{\nu}_{\ell_2}\,jj$, $m_h = 120$ GeV

Table A.2.: Process ID for $pp \to Hjj$ production via vector-boson fusion in the SM for heavy Higgs production. SBI denotes the full process with signal, background and their interference.

`HQSQR`	q^2 distribution of the Higgs Boson
0	on-shell
1	Breit Wigner distributed
2	CPS propagator (Passarino) [178, 179]

Table A.3.: q^2-distribution of the Higgs options.

APPENDIX B

LES HOUCHES EVENT FILES

For convenience we recapitulate the Les Houches Event (LHE) file format, as presented in [33, 34]. These event files are the standard output of parton-level event generators and can be used as input to shower Monte Carlo programs.

The main structure of the file, taken from [34] is as follows:

```
<LesHouchesEvents version="1.0">
  <!--
    # optional information in completely free format,
    # except for the reserved endtag (see next line)
  -->
  <init>
    mandatory initialization information
    # optional initialization information
  </init>
  <event>
    mandatory event information
    # optional event information
  </event>
  (further <event> ... </event> blocks, one for each event)
</LesHouchesEvents>
```

The compulsory information in the `init` block consist of

- `IDBMUP(1/2)`, the ID of the two beam particles according to the Particle Data Group convention [154];
- `EBMUP(1/2)`, the energy of the beam particles in GeV;
- `PDFGUP(1/2)`, the author group according to LHAPDF [125];

- `PDFSUP(1/2)`, the PDF set IDs according to LHAPDF [125];
- `IDWTUP`, a switch which specifies the interpretation of the event weight;
- `NPRUP`, the number of different user subprocesses;
- `XSECUP(IPR)`, the cross section in pb of subprocess `IPR` in the range 1 through `NPRUP`;
- `XERRUP(IPR)`, the statistical error for `XSECUP(IPR)`;
- `XMAXUP(IPR)`, the maximum event weight for this subprocess;
- `LPRUP(IPR)`, the user process ID that can appear in `IDPRUP`.

The `event` blocks are organized as follows, the first line comprises the common event information with

- `NUP`, the number of particles in the event;
- `IDPRUP`, the ID of the process in this event;
- `XWGTUP`, the event weight;
- `SCALUP`, the scale of the event in GeV;
- `AQEDUP`, the QED coupling constant used in this event;
- `AQCDUP`, the QCD coupling constant used in this event.

The additional `NUP` lines contain the information of each particle `I` in this event,

- `IDUP(I)`, the particle ID according to the Particle Data Group convention [154];
- `ISTUP(I)`, a status code, e.g. ∓ 1 for incoming/outgoing particles;
- `MOTHUP(1:2,I)`, the index of the first and last mother particle for outgoing particles coming from a decay;
- `ICOLUP(1:2,I)`, a tag for the color and anti-color flow line;
- `PUP(1:5,I)`, the lab frame momentum of the particle (p_x, p_y, p_z, E, m) in GeV;
- `VTIMUP(I)`, the distance from production to decay in mm;
- `SPINUP(I)`, the cosine of the lab-frame angle between the spin-vector of `I` and its mother particle. 9 for unpolarized particles.

Additional information of the event can be written afterwards in a comment line starting with `#`. One often used example is

```
#pdf id1 id2 x1 x2 scalePDF xpdf1 xpdf2
```

where `#pdf` is the identifying label, the other entries specify the used PDF values and scales.

BIBLIOGRAPHY

[1] E. Noether, *Invarianten beliebiger Differentialausdrücke*. Nachr. Ges. Wiss. Göttingen, Math.-Phys. Kl. **1918** (1918) 37–44.

[2] E. Noether, *Invariante Variationsprobleme*. Nachr. Ges. Wiss. Göttingen, Math.-Phys. Kl. **1918** (1918) 235–257.

[3] C.-N. Yang and R. L. Mills, *Conservation of Isotopic Spin and Isotopic Gauge Invariance*. Phys.Rev. **96** (1954) 191–195.

[4] M. Gell-Mann, *A Schematic Model of Baryons and Mesons*. Phys.Lett. **8** (1964) 214–215.

[5] H. Fritzsch, M. Gell-Mann, and H. Leutwyler, *Advantages of the Color Octet Gluon Picture*. Phys.Lett. **B47** (1973) 365–368.

[6] D. J. Gross and F. Wilczek, *Ultraviolet Behavior of Nonabelian Gauge Theories*. Phys.Rev.Lett. **30** (1973) 1343–1346.

[7] H. D. Politzer, *Reliable Perturbative Results for Strong Interactions?* Phys.Rev.Lett. **30** (1973) 1346–1349.

[8] S. Glashow, *Partial Symmetries of Weak Interactions*. Nucl.Phys. **22** (1961) 579–588.

[9] S. Weinberg, *A Model of Leptons*. Phys.Rev.Lett. **19** (1967) 1264–1266.

[10] A. Salam, *Weak and Electromagnetic Interactions*. Conf.Proc. **C680519** (1968) 367–377.

[11] **UA1 Collaboration**, G. Arnison *et al.*, *Experimental Observation of Isolated Large Transverse Energy Electrons with Associated Missing Energy at* $\sqrt{s} = 540$ *GeV*. Phys.Lett. **B122** (1983) 103–116.

[12] **UA2 Collaboration**, M. Banner *et al.*, *Observation of Single Isolated Electrons of High Transverse Momentum in Events with Missing Transverse Energy at the CERN anti-p p Collider*. Phys.Lett. **B122** (1983) 476–485.

[13] **UA1 Collaboration**, G. Arnison *et al.*, *Experimental Observation of Lepton Pairs of Invariant Mass Around 95 GeV/c^2 at the CERN SPS Collider*. Phys.Lett. **B126** (1983) 398–410.

[14] P. W. Higgs, *Broken Symmetries and the Masses of Gauge Bosons*. Phys.Rev.Lett. **13** (1964) 508–509.

[15] P. W. Higgs, *Spontaneous Symmetry Breakdown without Massless Bosons*. Phys.Rev. **145** (1966) 1156–1163.

[16] F. Englert and R. Brout, *Broken Symmetry and the Mass of Gauge Vector Mesons*. Phys.Rev.Lett. **13** (1964) 321–323.

[17] G. Guralnik, C. Hagen, and T. Kibble, *Global Conservation Laws and Massless Particles*. Phys.Rev.Lett. **13** (1964) 585–587.

[18] T. Kibble, *Symmetry breaking in non-Abelian gauge theories*. Phys.Rev. **155** (1967) 1554–1561.

[19] **ATLAS Collaboration**, G. Aad *et al.*, *Observation of a new particle in the search for the Standard Model Higgs boson with the ATLAS detector at the LHC*. Phys.Lett. **B716** (2012) 1–29, arXiv:1207.7214 [hep-ex].

[20] **CMS Collaboration**, S. Chatrchyan *et al.*, *Observation of a new boson at a mass of 125 GeV with the CMS experiment at the LHC*. Phys.Lett. **B716** (2012) 30–61, arXiv:1207.7235 [hep-ex].

[21] P. Nason, *A New method for combining NLO QCD with shower Monte Carlo algorithms*. JHEP **0411** (2004) 040, arXiv:hep-ph/0409146 [hep-ph].

[22] S. Frixione, P. Nason, and C. Oleari, *Matching NLO QCD computations with Parton Shower simulations: the POWHEG method*. JHEP **0711** (2007) 070, arXiv:0709.2092 [hep-ph].

[23] S. Alioli, P. Nason, C. Oleari, and E. Re, *A general framework for implementing NLO calculations in shower Monte Carlo programs: the POWHEG BOX*. JHEP **1006** (2010) 043, arXiv:1002.2581 [hep-ph].

[24] K. Arnold, M. Bähr, G. Bozzi, F. Campanario, C. Englert, *et al.*, *VBFNLO: A Parton level Monte Carlo for processes with electroweak bosons*. Comput.Phys.Commun. **180** (2009) 1661–1670, arXiv:0811.4559 [hep-ph].

[25] K. Arnold, J. Bellm, G. Bozzi, M. Brieg, F. Campanario, *et al.*, *VBFNLO: A Parton Level Monte Carlo for Processes with Electroweak Bosons – Manual for Version 2.5.0*. arXiv:1107.4038 [hep-ph].

[26] K. Arnold, J. Bellm, G. Bozzi, F. Campanario, C. Englert, *et al.*, *Release Note – Vbfnlo-2.6.0*. arXiv:1207.4975 [hep-ph].

[27] T. Sjöstrand, S. Mrenna, and P. Z. Skands, *PYTHIA 6.4 Physics and Manual*. JHEP **0605** (2006) 026, arXiv:hep-ph/0603175 [hep-ph].

[28] M. Bähr, S. Gieseke, M. Gigg, D. Grellscheid, K. Hamilton, *et al.*, *Herwig++ Physics and Manual*. Eur.Phys.J. **C58** (2008) 639–707, arXiv:0803.0883 [hep-ph].

[29] K. Arnold, L. d'Errico, S. Gieseke, D. Grellscheid, K. Hamilton, *et al.*, *Herwig++ 2.6 Release Note*. arXiv:1205.4902 [hep-ph].

[30] J. Bellm, S. Gieseke, D. Grellscheid, A. Papaefstathiou, S. Plätzer, *et al.*, *Herwig++ 2.7 Release Note*. arXiv:1310.6877 [hep-ph].

[31] S. Plätzer and S. Gieseke, *Coherent Parton Showers with Local Recoils*. JHEP **1101** (2011) 024, arXiv:0909.5593 [hep-ph].

[32] S. Plätzer and S. Gieseke, *Dipole Showers and Automated NLO Matching in Herwig++*. Eur.Phys.J. **C72** (2012) 2187, arXiv:1109.6256 [hep-ph].

[33] E. Boos, M. Dobbs, W. Giele, I. Hinchliffe, J. Huston, *et al.*, *Generic user process interface for event generators*. arXiv:hep-ph/0109068 [hep-ph].

[34] J. Alwall, A. Ballestrero, P. Bartalini, S. Belov, E. Boos, *et al.*, *A Standard format for Les Houches event files*. Comput.Phys.Commun. **176** (2007) 300–304, arXiv:hep-ph/0609017 [hep-ph].

[35] M. Böhm, A. Denner, and H. Joos, *Gauge Theories of the Strong and Electroweak Interaction*. Vieweg+Teubner Verlag, 2001.

[36] M. E. Peskin and D. V. Schroeder, *An Introduction To Quantum Field Theory (Frontiers in Physics)*. Westview Press, 1995.

[37] T. Muta, *Foundations Of Quantum Chromodynamics: An Introduction to Perturbative Methods in Gauge Theories (World Scientific Lecture Notes in Physics)*. World Scientific Publishing Company, 2009.

[38] R. K. Ellis, W. J. Stirling, and B. R. Webber, *QCD and Collider Physics (Cambridge Monographs on Particle Physics, Nuclear Physics and Cosmology)*. Cambridge University Press, 2003.

[39] A. Djouadi, *The Anatomy of electro-weak symmetry breaking. I: The Higgs boson in the standard model*. Phys.Rept. **457** (2008) 1–216, arXiv:hep-ph/0503172 [hep-ph].

[40] C. Llewellyn Smith, *High-Energy Behavior and Gauge Symmetry*. Phys.Lett. **B46** (1973) 233–236.

[41] J. Bell, *High-Energy Behavior of Tree Diagrams in Gauge Theories*. Nucl.Phys. **B60** (1973) 427–436.

[42] J. M. Cornwall, D. N. Levin, and G. Tiktopoulos, *Uniqueness of spontaneously broken gauge theories*. Phys.Rev.Lett. **30** (1973) 1268–1270.

[43] J. M. Cornwall, D. N. Levin, and G. Tiktopoulos, *Derivation of Gauge Invariance from High-Energy Unitarity Bounds on the s Matrix*. Phys.Rev. **D10** (1974) 1145.

[44] G. 't Hooft, *Renormalization of Massless Yang-Mills Fields*. Nucl.Phys. **B33** (1971) 173–199.

[45] G. 't Hooft, *Renormalizable Lagrangians for Massive Yang-Mills Fields*. Nucl.Phys. **B35** (1971) 167–188.

[46] N. Cabibbo, *Unitary Symmetry and Leptonic Decays*. Phys.Rev.Lett. **10** (1963) 531–533.

[47] M. Kobayashi and T. Maskawa, *CP Violation in the Renormalizable Theory of Weak Interaction*. Prog.Theor.Phys. **49** (1973) 652–657.

[48] **LHC Higgs Cross Section Working Group**. https://twiki.cern.ch/twiki/bin/view/LHCPhysics/CrossSections.

[49] **ATLAS Collaboration**, *Combined measurements of the mass and signal strength of the Higgs-like boson with the ATLAS detector using up to 25 fb^{-1} of proton-proton collision data*. ATLAS-CONF-2013-014, ATLAS-COM-CONF-2013-025, 2013.

[50] **CMS Collaboration**, S. Chatrchyan *et al.*, *Observation of a new boson with mass near 125 GeV in pp collisions at $\sqrt{s}$ = 7 and 8 TeV*. JHEP **1306** (2013) 081, arXiv:1303.4571 [hep-ex].

[51] R. Alkofer and J. Greensite, *Quark Confinement: The Hard Problem of Hadron Physics*. J.Phys. **G34** (2007) S3, arXiv:hep-ph/0610365 [hep-ph].

[52] V. Gribov and L. Lipatov, *Deep inelastic e p scattering in perturbation theory*. Sov.J.Nucl.Phys. **15** (1972) 438–450.

[53] G. Altarelli and G. Parisi, *Asymptotic Freedom in Parton Language*. Nucl.Phys. **B126** (1977) 298.

[54] Y. L. Dokshitzer, *Calculation of the Structure Functions for Deep Inelastic Scattering and e+ e- Annihilation by Perturbation Theory in Quantum Chromodynamics*. Sov.Phys.JETP **46** (1977) 641–653.

[55] T. Ohl, *Drawing Feynman diagrams with Latex and Metafont*. Comput.Phys.Commun. **90** (1995) 340–354, arXiv:hep-ph/9505351 [hep-ph].

[56] **LHC Higgs Cross Section Working Group**, S. Dittmaier *et al.*, *Handbook of LHC Higgs Cross Sections: 1. Inclusive Observables*. arXiv:1101.0593 [hep-ph].

[57] **LHC Higgs Cross Section Working Group**, S. Dittmaier, S. Dittmaier, C. Mariotti, G. Passarino, R. Tanaka, *et al.*, *Handbook of LHC Higgs Cross Sections: 2. Differential Distributions*. arXiv:1201.3084 [hep-ph].

[58] **LHC Higgs Cross Section Working Group**, S. Heinemeyer *et al.*, *Handbook of LHC Higgs Cross Sections: 3. Higgs Properties*. arXiv:1307.1347 [hep-ph].

[59] R. D. Ball, M. Bonvini, S. Forte, S. Marzani, and G. Ridolfi, *Higgs production in gluon fusion beyond NNLO*. Nucl.Phys. **B874** (2013) 746–772, arXiv:1303.3590 [hep-ph].

[60] M. Höschele, J. Hoff, A. Pak, M. Steinhauser, and T. Ueda, *Higgs boson production at the LHC: NNLO partonic cross sections through order ϵ and convolutions with splitting functions to N^3LO*. Phys.Lett. **B721** (2013) 244–251, arXiv:1211.6559 [hep-ph].

[61] C. Anastasiou, C. Duhr, F. Dulat, F. Herzog, and B. Mistlberger, *Real-virtual contributions to the inclusive Higgs cross-section at N^3LO*. JHEP **1312** (2013) 088, arXiv:1311.1425 [hep-ph].

[62] T. Han, G. Valencia, and S. Willenbrock, *Structure function approach to vector boson scattering in p p collisions*. Phys.Rev.Lett. **69** (1992) 3274–3277, arXiv:hep-ph/9206246 [hep-ph].

[63] T. Figy, C. Oleari, and D. Zeppenfeld, *Next-to-leading order jet distributions for Higgs boson production via weak boson fusion*. Phys.Rev. **D68** (2003) 073005, arXiv:hep-ph/0306109 [hep-ph].

[64] E. L. Berger and J. M. Campbell, *Higgs boson production in weak boson fusion at next-to-leading order*. Phys.Rev. **D70** (2004) 073011, arXiv:hep-ph/0403194 [hep-ph].

[65] R. V. Harlander, J. Vollinga, and M. M. Weber, *Gluon-Induced Weak Boson Fusion*. Phys.Rev. **D77** (2008) 053010, arXiv:0801.3355 [hep-ph].

[66] P. Bolzoni, F. Maltoni, S.-O. Moch, and M. Zaro, *Higgs production via vector-boson fusion at NNLO in QCD*. Phys.Rev.Lett. **105** (2010) 011801, arXiv:1003.4451 [hep-ph].

[67] P. Bolzoni, F. Maltoni, S.-O. Moch, and M. Zaro, *Vector boson fusion at NNLO in QCD: SM Higgs and beyond*. Phys.Rev. **D85** (2012) 035002, arXiv:1109.3717 [hep-ph].

[68] M. Ciccolini, A. Denner, and S. Dittmaier, *Strong and electroweak corrections to the production of Higgs + 2jets via weak interactions at the LHC*. Phys.Rev.Lett. **99** (2007) 161803, arXiv:0707.0381 [hep-ph].

[69] M. Ciccolini, A. Denner, and S. Dittmaier, *Electroweak and QCD corrections to Higgs production via vector-boson fusion at the LHC*. Phys.Rev. **D77** (2008) 013002, arXiv:0710.4749 [hep-ph].

[70] T. Figy, S. Palmer, and G. Weiglein, *Higgs Production via Weak Boson Fusion in the Standard Model and the MSSM*. JHEP **1202** (2012) 105, arXiv:1012.4789 [hep-ph].

[71] **ATLAS Collaboration**, *Combined coupling measurements of the Higgs-like boson with the ATLAS detector using up to 25 fb^{-1} of proton-proton collision data*. ATLAS-CONF-2013-034, ATLAS-COM-CONF-2013-035, 2013.

[72] **CMS Collaboration**, S. Chatrchyan *et al.*, *Study of the Mass and Spin-Parity of the Higgs Boson Candidate Via Its Decays to Z Boson Pairs*. Phys.Rev.Lett. **110** (2013) 081803, arXiv:1212.6639 [hep-ex].

[73] **CMS Collaboration**, *Updated measurements of the Higgs boson at 125 GeV in the two photon decay channel*. CMS-PAS-HIG-13-001, 2013.

[74] **CMS Collaboration**, *Update on the search for the standard model Higgs boson in pp collisions at the LHC decaying to W^+W^- in the fully leptonic final state*. CMS-PAS-HIG-13-003, 2013.

[75] **CMS Collaboration**, *Combination of standard model Higgs boson searches and measurements of the properties of the new boson with a mass near 125 GeV*. CMS-PAS-HIG-13-005, 2013.

[76] **CMS Collaboration**, C. Collaboration, *Properties of the observed Higgs-like resonance using the diphoton channel*. CMS-PAS-HIG-13-016, 2013.

[77] **CMS Collaboration**, S. Chatrchyan *et al.*, *Measurement of Higgs boson production and properties in the WW decay channel with leptonic final states*. JHEP **1401** (2014) 096, arXiv:1312.1129 [hep-ex].

[78] **CMS Collaboration**, S. Chatrchyan *et al.*, *Measurement of the properties of a Higgs boson in the four-lepton final state*. arXiv:1312.5353 [hep-ex].

[79] **ATLAS Collaboration**, G. Aad *et al.*, *Measurements of Higgs boson production and couplings in diboson final states with the ATLAS detector at the LHC*. Phys.Lett. **B726** (2013) 88–119, arXiv:1307.1427 [hep-ex].

[80] **ATLAS Collaboration**, G. Aad *et al.*, *Evidence for the spin-0 nature of the Higgs boson using ATLAS data*. Phys.Lett. **B726** (2013) 120–144, arXiv:1307.1432 [hep-ex].

[81] **ATLAS Collaboration**, *Measurements of the properties of the Higgs-like boson in the four lepton decay channel with the ATLAS detector using 25 fb^{-1} of proton-proton collision data*. ATLAS-CONF-2013-013, ATLAS-COM-CONF-2013-018, 2013.

[82] **ATLAS Collaboration**, *Study of the spin of the Higgs-like boson in the two photon decay channel using 20.7 fb^{-1} of pp collisions collected at $\sqrt{s}$ = 8 TeV with the ATLAS detector*. ATLAS-CONF-2013-029, ATLAS-COM-CONF-2013-027, 2013.

[83] **ATLAS Collaboration**, *Study of the spin properties of the Higgs-like particle in the $H \to WW^{(*)} \to e\nu\mu\nu$ channel with 21 fb^{-1} of $\sqrt{s} = 8$ TeV data collected with the ATLAS detector*. ATLAS-CONF-2013-031, ATLAS-COM-CONF-2013-017, 2013.

[84] **ATLAS Collaboration**, *Study of the spin of the new boson with up to 25 fb^{-1} of ATLAS data*. ATLAS-CONF-2013-040, ATLAS-COM-CONF-2013-048, 2013.

[85] M. Klute, R. Lafaye, T. Plehn, M. Rauch, and D. Zerwas, *Measuring Higgs Couplings at a Linear Collider*. Europhys.Lett. **101** (2013) 51001, arXiv:1301.1322 [hep-ph].

[86] S. Frixione and B. R. Webber, *Matching NLO QCD computations and parton shower simulations*. JHEP **0206** (2002) 029, arXiv:hep-ph/0204244 [hep-ph].

[87] A. Buckley, J. Butterworth, S. Gieseke, D. Grellscheid, S. Hoche, *et al.*, *General-purpose event generators for LHC physics*. Phys.Rept. **504** (2011) 145–233, arXiv:1101.2599 [hep-ph].

[88] F. Ambroglini, R. Armillis, P. Azzi, G. Bagliesi, A. Ballestrero, *et al.*, *Proceedings of the Workshop on Monte Carlo's, Physics and Simulations at the LHC. Part I*. arXiv:0902.0293 [hep-ph].

[89] F. Bloch and A. Nordsieck, *Note on the Radiation Field of the electron*. Phys.Rev. **52** (1937) 54–59.

[90] T. Kinoshita, *Mass singularities of Feynman amplitudes*. J.Math.Phys. **3** (1962) 650–677.

[91] T. Lee and M. Nauenberg, *Degenerate Systems and Mass Singularities*. Phys.Rev. **133** (1964) B1549–B1562.

[92] S. Catani and M. Seymour, *A General algorithm for calculating jet cross-sections in NLO QCD*. Nucl.Phys. **B485** (1997) 291–419, arXiv:hep-ph/9605323 [hep-ph].

[93] S. Catani, S. Dittmaier, M. H. Seymour, and Z. Trocsanyi, *The Dipole formalism for next-to-leading order QCD calculations with massive partons*. Nucl.Phys. **B627** (2002) 189–265, arXiv:hep-ph/0201036 [hep-ph].

[94] D. A. Kosower, *Antenna factorization of gauge theory amplitudes*. Phys.Rev. **D57** (1998) 5410–5416, arXiv:hep-ph/9710213 [hep-ph].

[95] D. A. Kosower, *Antenna factorization in strongly ordered limits*. Phys.Rev. **D71** (2005) 045016, arXiv:hep-ph/0311272 [hep-ph].

[96] A. Gehrmann-De Ridder, T. Gehrmann, and E. N. Glover, *Antenna subtraction at NNLO*. JHEP **0509** (2005) 056, arXiv:hep-ph/0505111 [hep-ph].

[97] A. Daleo, T. Gehrmann, and D. Maitre, *Antenna subtraction with hadronic initial states*. JHEP **0704** (2007) 016, arXiv:hep-ph/0612257 [hep-ph].

[98] S. Frixione, Z. Kunszt, and A. Signer, *Three jet cross-sections to next-to-leading order*. Nucl.Phys. **B467** (1996) 399–442, arXiv:hep-ph/9512328 [hep-ph].

[99] S. Frixione, *A General approach to jet cross-sections in QCD*. Nucl.Phys. **B507** (1997) 295–314, arXiv:hep-ph/9706545 [hep-ph].

[100] Y. Dokshitzer, V. Khoze, and S. Troian, *Physics in Collision: Proceedings of the 6th International Conference on Physics in Collision. Chicago, Il. Sept 3-5, 1986*. World Scientific Publishing Co Pte Ltd, 1987.

[101] J. Bjorken, *Rapidity gaps and jets as a new physics signature in very high-energy hadron hadron collisions*. Phys.Rev. **D47** (1993) 101–113.

[102] V. D. Barger, R. Phillips, and D. Zeppenfeld, *Mini - jet veto: A Tool for the heavy Higgs search at the LHC*. Phys.Lett. **B346** (1995) 106–114, arXiv:hep-ph/9412276 [hep-ph].

[103] D. L. Rainwater, R. Szalapski, and D. Zeppenfeld, *Probing color singlet exchange in Z + two jet events at the CERN LHC*. Phys.Rev. **D54** (1996) 6680–6689, arXiv:hep-ph/9605444 [hep-ph].

[104] V. Khoze, M. Ryskin, W. Stirling, and P. Williams, *A Z monitor to calibrate Higgs production via vector boson fusion with rapidity gaps at the LHC*. Eur.Phys.J. **C26** (2003) 429–440, arXiv:hep-ph/0207365 [hep-ph].

[105] POWHEG-BOX. http://powhegbox.mib.infn.it/.

[106] F. Schissler and D. Zeppenfeld, *Parton Shower Effects on W and Z Production via Vector Boson Fusion at NLO QCD*. JHEP **1304** (2013) 057, arXiv:1302.2884.

[107] **CMS Collaboration**, *Measurement of the electroweak production cross section of the Z boson with two forward-backward jets in pp collisions at 7 TeV*. CMS-PAS-FSQ-12-019, CERN, Geneva, 2012.

[108] **CMS Collaboration**, *Measurement of pure electroweak production of a Z boson in association with two forward/backward jets in proton-proton collisions at 8 TeV*. CMS-PAS-FSQ-12-035, 2013.

[109] **ATLAS Collaboration**, G. Aad *et al.*, *Measurement of the electroweak production of dijets in association with a Z-boson and distributions sensitive to vector boson fusion in proton-proton collisions at sqrt(s) = 8 TeV using the ATLAS detector*. arXiv:1401.7610 [hep-ex].

[110] V. Khoze, M. Ryskin, W. Stirling, and P. Williams, *A Z monitor to calibrate Higgs production via vector boson fusion with rapidity gaps at the LHC*. Eur.Phys.J. **C26** (2003) 429–440, arXiv:hep-ph/0207365 [hep-ph].

[111] U. Baur and D. Zeppenfeld, *Measuring three vector boson couplings in $q\,q \to q\,q$ W at the SSC*. arXiv:hep-ph/9309227 [hep-ph].

[112] O. Eboli and M. Gonzalez-Garcia, *Probing trilinear gauge boson interactions via single electroweak gauge boson production at the CERN LHC*. Phys.Rev. **D70** (2004) 074011, arXiv:hep-ph/0405269 [hep-ph].

[113] C. Oleari and D. Zeppenfeld, *QCD corrections to electroweak νljj and l^+l^-jj production*. Phys.Rev. **D69** (2004) 093004, arXiv:hep-ph/0310156 [hep-ph].

[114] A. Denner, L. Hofer, A. Scharf, and S. Uccirati, *Electroweak corrections to Z + 2 jets production at the LHC*. arXiv:1311.5336 [hep-ph].

[115] B. Jäger, S. Schneider, and G. Zanderighi, *Next-to-leading order QCD corrections to electroweak Zjj production in the POWHEGBOX*. JHEP **1209** (2012) 083, arXiv:1207.2626 [hep-ph].

[116] J. M. Campbell and R. K. Ellis, *Next-to-leading order corrections to W + 2 jet and Z + 2 jet production at hadron colliders*. Phys.Rev. **D65** (2002) 113007, arXiv:hep-ph/0202176 [hep-ph].

[117] J. M. Campbell, R. K. Ellis, and D. L. Rainwater, *Next-to-leading order QCD predictions for W + 2 jet and Z + 2 jet production at the CERN LHC*. Phys.Rev. **D68** (2003) 094021, arXiv:hep-ph/0308195 [hep-ph].

[118] E. Re, *NLO corrections merged with parton showers for Z+2 jets production using the POWHEG method*. JHEP **1210** (2012) 031, arXiv:1204.5433 [hep-ph].

[119] J. M. Campbell, R. K. Ellis, P. Nason, and G. Zanderighi, *W and Z bosons in association with two jets using the POWHEG method*. JHEP **1308** (2013) 005, arXiv:1303.5447 [hep-ph].

[120] P. Nason and C. Oleari, *NLO Higgs boson production via vector-boson fusion matched with shower in POWHEG*. JHEP **1002** (2010) 037, arXiv:0911.5299 [hep-ph].

[121] A. Denner, S. Dittmaier, M. Roth, and D. Wackeroth, *Predictions for all processes $e^+\,e^- \to 4$ fermions + gamma*. Nucl.Phys. **B560** (1999) 33–65, arXiv:hep-ph/9904472 [hep-ph].

[122] S. Alioli, P. Nason, C. Oleari, and E. Re, *Vector boson plus one jet production in POWHEG*. JHEP **1101** (2011) 095, arXiv:1009.5594 [hep-ph].

[123] P. Nason and C. Oleari, *Generation cuts and Born suppression in POWHEG*. arXiv:1303.3922 [hep-ph].

[124] H.-L. Lai, M. Guzzi, J. Huston, Z. Li, P. M. Nadolsky, *et al.*, *New parton distributions for collider physics*. Phys.Rev. **D82** (2010) 074024, arXiv:1007.2241 [hep-ph].

[125] M. Whalley, D. Bourilkov, and R. Group, *The Les Houches accord PDFs (LHAPDF) and LHAGLUE*. arXiv:hep-ph/0508110 [hep-ph]. http://hepforge.cedar.ac.uk/lhapdf/.

[126] M. Cacciari, G. P. Salam, and G. Soyez, *The Anti-k(t) jet clustering algorithm*. JHEP **0804** (2008) 063, arXiv:0802.1189 [hep-ph].

[127] M. Cacciari and G. P. Salam, *Dispelling the N^3 myth for the k_t jet-finder*. Phys.Lett. **B641** (2006) 57–61, arXiv:hep-ph/0512210 [hep-ph].

[128] M. Cacciari, G. P. Salam, and G. Soyez, *FastJet User Manual*. Eur.Phys.J. **C72** (2012) 1896, arXiv:1111.6097 [hep-ph].

[129] S. D. Ellis, Z. Kunszt, and D. E. Soper, *Jets at hadron colliders at order $\alpha_s^{3:}$ A Look inside*. Phys.Rev.Lett. **69** (1992) 3615–3618, arXiv:hep-ph/9208249 [hep-ph].

[130] **ATLAS Collaboration**, G. Aad *et al.*, *Study of Jet Shapes in Inclusive Jet Production in pp Collisions at $\sqrt{s} = 7$ TeV using the ATLAS Detector*. Phys.Rev. **D83** (2011) 052003, arXiv:1101.0070 [hep-ex].

[131] J. R. Andersen and J. M. Smillie, *QCD and electroweak interference in Higgs production by gauge boson fusion*. Phys.Rev. **D75** (2007) 037301, arXiv:hep-ph/0611281 [hep-ph].

[132] A. Bredenstein, K. Hagiwara, and B. Jäger, *Mixed QCD-electroweak contributions to Higgs-plus-dijet production at the LHC*. Phys.Rev. **D77** (2008) 073004, arXiv:0801.4231 [hep-ph].

[133] L. d'Errico and P. Richardson, *A Positive-Weight Next-to-Leading-Order Monte Carlo Simulation of Deep Inelastic Scattering and Higgs Boson Production via Vector Boson Fusion in Herwig++*. Eur.Phys.J. **C72** (2012) 2042, arXiv:1106.2983 [hep-ph].

[134] S. Frixione, P. Torrielli, and M. Zaro, *Higgs production through vector-boson fusion at the NLO matched with parton showers*. Phys.Lett. **B726** (2013) 273–282, arXiv:1304.7927 [hep-ph].

[135] K. B. Arnold, *NLO Corrections and Parton Showers in the LHC Era*. Phd thesis, ITP, KIT. http://digbib.ubka.uni-karlsruhe.de/volltexte/1000035541.

[136] T. Plehn, D. L. Rainwater, and D. Zeppenfeld, *Determining the structure of Higgs couplings at the LHC*. Phys.Rev.Lett. **88** (2002) 051801, arXiv:hep-ph/0105325 [hep-ph].

[137] C. Englert, M. Spannowsky, and M. Takeuchi, *Measuring Higgs CP and couplings with hadronic event shapes*. JHEP **1206** (2012) 108, arXiv:1203.5788 [hep-ph].

[138] I. Anderson, S. Bolognesi, F. Caola, Y. Gao, A. V. Gritsan, *et al.*, *Constraining anomalous HVV interactions at proton and lepton colliders*. arXiv:1309.4819 [hep-ph].

[139] A. Djouadi, R. Godbole, B. Mellado, and K. Mohan, *Probing the spin-parity of the Higgs boson via jet kinematics in vector boson fusion*. Phys.Lett. **B723** (2013) 307–313, arXiv:1301.4965 [hep-ph].

[140] W. Buchmüller and D. Wyler, *Effective Lagrangian Analysis of New Interactions and Flavor Conservation*. Nucl.Phys. **B268** (1986) 621.

[141] T. Figy and D. Zeppenfeld, *QCD corrections to jet correlations in weak boson fusion*. Phys.Lett. **B591** (2004) 297–303, arXiv:hep-ph/0403297 [hep-ph].

[142] V. Hankele, G. Klämke, D. Zeppenfeld, and T. Figy, *Anomalous Higgs boson couplings in vector boson fusion at the CERN LHC*. Phys.Rev. **D74** (2006) 095001, arXiv:hep-ph/0609075 [hep-ph].

[143] F. Maltoni, K. Mawatari, and M. Zaro, *Higgs characterisation via vector-boson fusion and associated production: NLO and parton-shower effects*. arXiv:1311.1829 [hep-ph].

[144] I. Low and J. Lykken, *Revealing the electroweak properties of a new scalar resonance*. JHEP **1010** (2010) 053, arXiv:1005.0872 [hep-ph].

[145] I. Low, J. Lykken, and G. Shaughnessy, *Singlet scalars as Higgs imposters at the Large Hadron Collider*. Phys.Rev. **D84** (2011) 035027, arXiv:1105.4587 [hep-ph].

[146] L. M. Carpenter and J. Goodman, *Pseudo-Higgs Signals a the LHC*. arXiv:1205.5555 [hep-ph].

[147] I. Low, J. Lykken, and G. Shaughnessy, *Have We Observed the Higgs (Imposter)?* Phys.Rev. **D86** (2012) 093012, arXiv:1207.1093 [hep-ph].

[148] B. Batell, D. McKeen, and M. Pospelov, *Singlet Neighbors of the Higgs Boson*. JHEP **1210** (2012) 104, arXiv:1207.6252 [hep-ph].

[149] K. Hagiwara, S. Ishihara, R. Szalapski, and D. Zeppenfeld, *Low-energy effects of new interactions in the electroweak boson sector*. Phys.Rev. **D48** (1993) 2182–2203.

[150] K. Hagiwara, R. Szalapski, and D. Zeppenfeld, *Anomalous Higgs boson production and decay*. Phys.Lett. **B318** (1993) 155–162, arXiv:hep-ph/9308347 [hep-ph].

[151] M. Gonzalez-Garcia, *Anomalous Higgs couplings*. Int.J.Mod.Phys. **A14** (1999) 3121–3156, arXiv:hep-ph/9902321 [hep-ph].

[152] O. J. Eboli, M. Gonzalez-Garcia, S. Lietti, and S. Novaes, *Probing intermediate mass Higgs interactions at the CERN Large Hadron Collider*. Phys.Lett. **B478** (2000) 199–207, arXiv:hep-ph/0001030 [hep-ph].

[153] B. Zhang, Y.-P. Kuang, H.-J. He, and C. Yuan, *Testing anomalous gauge couplings of the Higgs boson via weak boson scatterings at the CERN LHC*. Phys.Rev. **D67** (2003) 114024, arXiv:hep-ph/0303048 [hep-ph].

[154] **Particle Data Group**, J. Beringer *et al.*, *Review of Particle Physics (RPP)*. Phys.Rev. **D86** (2012) 010001.

[155] M. E. Peskin and T. Takeuchi, *A New constraint on a strongly interacting Higgs sector*. Phys.Rev.Lett. **65** (1990) 964–967.

[156] J. Erler and P. Langacker, *Electroweak model and constraints on new physics*. arXiv:hep-ph/0407097 [hep-ph].

[157] V. Hankele, *Schranken an anomale Higgs-Kopplungen*. diploma thesis, ITP, KIT, 2005. http://www-itp.particle.uni-karlsruhe.de/prep/diploma/PSFiles/Diplom_Hankele.ps.gz.

[158] K. Hagiwara, R. Peccei, D. Zeppenfeld, and K. Hikasa, *Probing the Weak Boson Sector in e+ e- → W+ W-*. Nucl.Phys. **B282** (1987) 253.

[159] G. Gounaris, J. Kneur, D. Zeppenfeld, Z. Ajaltouni, A. Arhrib, *et al.*, *Triple gauge boson couplings*. arXiv:hep-ph/9601233 [hep-ph].

[160] G. Altarelli, T. Sjöstrand, and F. Zwirner, *Physics at LEP2: Vol. 1*.

[161] **L3 Collaboration**, P. Achard *et al.*, *Search for anomalous couplings in the Higgs sector at LEP*. Phys.Lett. **B589** (2004) 89–102, arXiv:hep-ex/0403037 [hep-ex].

[162] G. Passarino and M. Veltman, *One Loop Corrections for e+ e- Annihilation into mu+ mu- in the Weinberg Model*. Nucl.Phys. **B160** (1979) 151.

[163] **ATLAS collaboration**, G. Aad *et al.*, *Updated coupling measurements of the Higgs boson with the ATLAS detector using up to 25 fb^{-1} of proton-proton collision data*. ATLAS-CONF-2014-009, ATLAS-COM-CONF-2014-013, 2014.

[164] C. Englert, B. Feigl, J. Frank, M. Rauch, O. Schlimpert, and F. Schissler, *Dipole Form Factor Calculation Tool for Anomalous Couplings in VBFNLO*. ITP, KIT, 2013. www.itp.kit.edu/~vbfnloweb/wiki/doku.php?id=download:formfactor.

[165] V. D. Barger, K.-M. Cheung, T. Han, and R. Phillips, *Strong W^+W^+ scattering signals at pp supercolliders*. Phys.Rev. **D42** (1990) 3052–3077.

[166] G. Gounaris, J. Layssac, and F. Renard, *Unitarity constraints for transverse gauge bosons at LEP and supercolliders*. Phys.Lett. **B332** (1994) 146–152, arXiv:hep-ph/9311370 [hep-ph].

[167] **CMS Collaboration**, S. Chatrchyan *et al.*, *Search for a standard-model-like Higgs boson with a mass in the range 145 to 1000 GeV at the LHC*. Eur.Phys.J. **C73** (2013) 2469, arXiv:1304.0213 [hep-ex].

[168] **ATLAS Collaboration**, *Search for a high-mass Higgs boson in the $H \to WW \to l\nu l\nu$ decay channel with the ATLAS detector using 21 fb^{-1} of proton-proton collision data*. ATLAS-CONF-2013-067, CERN, Geneva, Jul, 2013.

[169] H. Hoffmann, *Singuletts als Higgs-Doppelgänger: Untersuchung im Rahmen einer effektiven Feldtheorie*. diploma thesis, ITP, KIT, 2013.

[170] J. Alwall, P. Demin, S. de Visscher, R. Frederix, M. Herquet, *et al.*, *MadGraph/MadEvent v4: The New Web Generation*. JHEP **0709** (2007) 028, arXiv:0706.2334 [hep-ph].

[171] **CMS Collaboration**, S. Chatrchyan *et al.*, *Evidence for the 125 GeV Higgs boson decaying to a pair of τ leptons*. arXiv:1401.5041 [hep-ex].

[172] **CMS Collaboration**, S. Chatrchyan *et al.*, *Evidence for the direct decay of the 125 GeV Higgs boson to fermions*. arXiv:1401.6527 [hep-ex].

[173] F. James and M. Roos, *Minuit: A System for Function Minimization and Analysis of the Parameter Errors and Correlations*. Comput.Phys.Commun. **10** (1975) 343–367.

[174] J. Frank, M. Rauch, and D. Zeppenfeld, *Spin-2 Resonances in Vector-Boson-Fusion Processes at NLO QCD*. Phys.Rev. **D87** (2013) 055020, arXiv:1211.3658 [hep-ph].

[175] J. Frank, M. Rauch, and D. Zeppenfeld, *Higgs Spin Determination in the WW channel and beyond*. arXiv:1305.1883 [hep-ph].

[176] J. Frank, *Higgs Spin Determination and Unitarity of Vector-boson Scattering at the LHC*. Phd thesis, ITP, KIT, 2014. http://digbib.ubka.uni-karlsruhe.de/volltexte/1000038521.

[177] K. Hagiwara, J. Kanzaki, Q. Li, and K. Mawatari, *HELAS and MadGraph/MadEvent with spin-2 particles*. Eur.Phys.J. **C56** (2008) 435–447, arXiv:0805.2554 [hep-ph].

[178] G. Passarino, C. Sturm, and S. Uccirati, *Higgs Pseudo-Observables, Second Riemann Sheet and All That*. Nucl.Phys. **B834** (2010) 77–115, arXiv:1001.3360 [hep-ph].

[179] S. Goria, G. Passarino, and D. Rosco, *The Higgs Boson Lineshape*. Nucl.Phys. **B864** (2012) 530–579, arXiv:1112.5517 [hep-ph].

[180] B. Jäger, C. Oleari, and D. Zeppenfeld, *Next-to-leading order QCD corrections to W^+W^- production via vector-boson fusion*. JHEP **0607** (2006) 015, arXiv:hep-ph/0603177 [hep-ph].

[181] B. Jäger, C. Oleari, and D. Zeppenfeld, *Next-to-leading order QCD corrections to Z boson pair production via vector-boson fusion*. Phys.Rev. **D73** (2006) 113006, arXiv:hep-ph/0604200 [hep-ph].

[182] W. Beenakker, S. Dittmaier, M. Kramer, B. Plumper, M. Spira, *et al.*, *Higgs radiation off top quarks at the Tevatron and the LHC*. Phys.Rev.Lett. **87** (2001) 201805, arXiv:hep-ph/0107081 [hep-ph].

[183] L. Reina and S. Dawson, *Next-to-leading order results for t anti-t h production at the Tevatron*. Phys.Rev.Lett. **87** (2001) 201804, arXiv:hep-ph/0107101 [hep-ph].

[184] W. Beenakker, S. Dittmaier, M. Kramer, B. Plumper, M. Spira, *et al.*, *NLO QCD corrections to t anti-t H production in hadron collisions*. Nucl.Phys. **B653** (2003) 151–203, arXiv:hep-ph/0211352 [hep-ph].

[185] S. Dawson, L. Orr, L. Reina, and D. Wackeroth, *Associated top quark Higgs boson production at the LHC*. Phys.Rev. **D67** (2003) 071503, arXiv:hep-ph/0211438 [hep-ph].

[186] A. Djouadi, J. Kalinowski, and M. Spira, *HDECAY: A Program for Higgs boson decays in the standard model and its supersymmetric extension*. Comput.Phys.Commun. **108** (1998) 56–74, arXiv:hep-ph/9704448 [hep-ph].

[187] S. Alioli, P. Nason, C. Oleari, and E. Re, *NLO Higgs boson production via gluon fusion matched with shower in POWHEG*. JHEP **0904** (2009) 002, arXiv:0812.0578 [hep-ph].

[188] **VBFNLO Collaboration**. http://www.itp.kit.edu/~vbfnloweb/wiki/doku.php?id=external:heavyhiggs:overview.

[189] D. Zeppenfeld, R. Kinnunen, A. Nikitenko, and E. Richter-Was, *Measuring Higgs boson couplings at the CERN LHC*. Phys.Rev. **D62** (2000) 013009, arXiv:hep-ph/0002036 [hep-ph].

[190] M. Duhrssen, S. Heinemeyer, H. Logan, D. Rainwater, G. Weiglein, *et al.*, *Extracting Higgs boson couplings from CERN LHC data*. Phys.Rev. **D70** (2004) 113009, arXiv:hep-ph/0406323 [hep-ph].

[191] **LHC Higgs Cross Section Working Group**, A. David *et al.*, *LHC HXSWG interim recommendations to explore the coupling structure of a Higgs-like particle*. arXiv:1209.0040 [hep-ph].

[192] T. Figy, V. Hankele, and D. Zeppenfeld, *Next-to-leading order QCD corrections to Higgs plus three jet production in vector-boson fusion*. JHEP **0802** (2008) 076, arXiv:0710.5621 [hep-ph].

[193] T. M. Figy, *NLO QCD corrections to the jet activity in Higgs boson production via vector-boson fusion*. Phd thesis, 2006. http://inspirehep.net/record/736914/files/736914.pdf.

[194] F. Campanario, T. Figy, S. Plätzer, and M. Sjödahl, *Electroweak Higgs plus Three Jet Production at NLO QCD*. Phys.Rev.Lett. **111** (2013) 211802, arXiv:1308.2932 [hep-ph].

[195] J. Vermaseren, *New features of FORM*. arXiv:math-ph/0010025 [math-ph].

[196] T. van Ritbergen, A. Schellekens, and J. Vermaseren, *Group theory factors for Feynman diagrams*. Int.J.Mod.Phys. **A14** (1999) 41–96, arXiv:hep-ph/9802376 [hep-ph].

[197] T. Stelzer and W. Long, *Automatic generation of tree level helicity amplitudes*. Comput.Phys.Commun. **81** (1994) 357–371, arXiv:hep-ph/9401258 [hep-ph].

[198] F. Maltoni and T. Stelzer, *MadEvent: Automatic event generation with MadGraph*. JHEP **0302** (2003) 027, arXiv:hep-ph/0208156 [hep-ph].

[199] A. Kardos, P. Nason, and C. Oleari, *Three-jet production in POWHEG*. arXiv:1402.4001 [hep-ph].

[200] J. M. Campbell, R. K. Ellis, R. Frederix, P. Nason, C. Oleari, *et al.*, *NLO Higgs Boson Production Plus One and Two Jets Using the POWHEG BOX, MadGraph4 and MCFM*. JHEP **1207** (2012) 092, arXiv:1202.5475 [hep-ph].

[201] **VBFNLO Collaboration**. http://www.itp.kit.edu/~vbfnloweb/wiki/doku.php?id=documentation:repolo.

ACKNOWLEDGMENTS

First of all, I thank Prof. Dr. Dieter Zeppenfeld for accepting me as a PhD student and for giving me the possibility to work on such an interesting topic. I am very grateful for many illuminating discussions, his advice and his valuable comments on my work. I also want to thank him for giving me the opportunity to attend several schools and conferences.

I would like to thank Prof. Dr. Günter Quast for agreeing to be the second referee of this thesis.

Furthemore, I want to thank Barbara Jäger for the fruitful collaboration on the $H3j$ project, Stefan Gieseke for many useful discussions concerning the differences between Herwig++ and Pythia, and particularly Michael Rauch for many interesting and rewarding discussions on the Repolo project and beyond.

I am very thankful to Bastian Feigl, Christian Hangst, Thomas Hermann, Michael Rauch and Christian Röhr for the careful proof-reading of many parts of this thesis.

I also thank the members of the ITP for the friendly and enjoyable atmosphere at the institute. Special thanks go to Johannes Bellm, Bastian Feigl, Christian Hangst and Ramona Gröber for many interesting discussions. I also warmly thank my officemates Jessica Frank and Christian Röhr for the inspiring atmosphere. In addition, the work of the coffee machine is greatly appreciated.

This work would not have been possible without a smoothly running computer infrastructure. Therefore, special thanks go to the admins, Johannes Bellm, Bastian Feigl, Christian Röhr and Robin Roth.

The funding support for this thesis by the "GRK 1694: Elementarteilchenphysik bei höchster Energie und höchster Präzision" as well as by the "Karlsruher Schule für Elementarteilchen- und Astroteilchenphysik: Wissenschaft und Technologie (KSETA)" is greatly acknowledged.

Ein ganz besonderer Dank gilt natürlich meiner Familie, die mich in den letzten Jahren unglaublich unterstützt hat und mir besonders in schwierigen Phasen dieser Arbeit immer zur Seite stand.

Zu guter Letzt danke ich Thomas von ganzem Herzen für seine Liebe, seine Unterstützung und dafür, dass er sein Leben mit mir teilt und meines bereichert.